Title
Tides in Close Binary Systems

Author
Burkart, Joshua

Publication Date
2014

Peer reviewed|Thesis/dissertation

Tides in Close Binary Systems

By

Joshua Burkart

A dissertation submitted in partial satisfaction of the

requirements for the degree of

Doctor of Philosophy

in

Physics

in the

Graduate Division

of the

University of California, Berkeley

Committee in charge:

Professor Eliot Quataert, Chair
Professor Daniel Kasen
Professor Bruce Buffett

Fall 2014

Tides in Close Binary Systems

Abstract

Tides in Close Binary Systems

by

Joshua Burkart

Doctor of Philosophy in Physics

University of California, Berkeley

Professor Eliot Quataert, Chair

We consider three aspects of tidal interactions in close binary systems. 1) We first develop a framework for predicting and interpreting photometric observations of eccentric binaries, which we term tidal asteroseismology. In such systems, the Fourier transform of the observed lightcurve is expected to consist of pulsations at harmonics of the orbital frequency. We use linear stellar perturbation theory to predict the expected pulsation amplitude spectra. Our numerical model does not assume adiabaticity, and accounts for stellar rotation in the traditional approximation. We apply our model to the recently discovered *Kepler* system KOI-54, a 42-day face-on stellar binary with $e = 0.83$. Our modeling yields pulsation spectra that are semi-quantitatively consistent with observations of KOI-54. KOI-54's spectrum also contains several nonharmonic pulsations, which can be explained by nonlinear three-mode coupling. 2) We next consider the situation of a white dwarf (WD) binary inspiraling due to the emission of gravitational waves. We show that resonance locks, previously considered in binaries with an early-type star, occur universally in WD binaries. In a resonance lock, the orbital and spin frequencies evolve in lockstep, so that the tidal forcing frequency is approximately constant and a particular normal mode remains resonant, producing efficient tidal dissipation and nearly synchronous rotation. We derive analytic formulas for the tidal quality factor and tidal heating rate during a g-mode resonance lock, and verify our results numerically. We apply our analysis to the 13-minute double-WD binary J0651, and show that our predictions are roughly consistent with observations. 3) Lastly, we examine the general dynamics of resonance locking in more detail. Previous analyses of resonance locking, including my own earlier work, invoke the adiabatic (a.k.a. Lorentzian) approximation for the mode amplitude, valid only in the limit of relatively strong mode damping. We relax this approximation, analytically derive conditions under which the fixed point associated with resonance locking is stable, and further check our analytic results with numerical integration of the coupled mode, spin, and orbital evolution equations. These show that resonance locking can sometimes take the form of complex limit cycles or even chaotic trajectories. We also show that resonance locks can accelerate the course of tidal evolution in eccentric systems.

I dedicate this dissertation to my parents, Cliff Meneken and Bonnie Burkart, and to my research advisor, Eliot Quataert.

Acknowledgments

I am pleased to thank my research advisor, Eliot Quataert, and my principal collaborators, Phil Arras and Nevin Weinberg. I also thank Edgar Knobloch, Keaton Burns, Geoff Marcy, and Eugene Chiang for useful consultations.

My research was supported by an NSF Graduate Research Fellowship, by NSF grant AST-0908873, and NASA grant NNX09AF98G.

Contents

Chapter 1

Introduction

Newton, using his law of gravity, showed that two isolated point-like celestial bodies travel on stable elliptical orbits that do not change with time. As such, a binary is an extremely stable and ubiquitous phenomenon. One of the primary ways by which binaries evolve is by the influence of tides.

The first theoretical analysis of tides also dates to Newton, who correctly explained their occurrence on the Earth as resulting from the differential gravity of both the Sun and Moon. Tides only cause secular orbital evolution when they lag behind the perturbing gravitational potential, which can occur as a result of internal dissipation acting on the tidal bulge or *equilibrium tide*. G.H. Darwin (son of Charles Darwin) used this observation to develop a quantitative theory of the tidal evolution of moons orbiting a planet (see e.g. Darwin 2010).

Darwin, along with many subsequent authors, parameterized a given body's internal dissipation via the so-called tidal quality factor or "tidal Q" (Goldreich & Soter 1966) by analogy with a simple harmonic oscillator. Zahn (1977) performed the first *a priori* calculation of tidal dissipation on the equilibrium tide for stellar binaries, and thus the first theoretical prediction of the tidal Q. Zahn (1977) relied on the influence of turbulent convection to retard the equilibrium tide.

The equilibrium tide can be thought of as the set of internal oscillation modes that are spatially commensurate with the tidal potential. There is another source of tidal dissipation, however, known as the *dynamical tide*, which corresponds to the set of internal oscillation modes that are instead temporally commensurate with the tidal potential. In other words, the dynamical tide comprises internal waves with frequencies comparable to a binary's orbital frequency that can thus be resonantly excited. Although the equilibrium tide contains the majority of the tidal energy, it also possesses a very long effective wavelength, and thus is weakly damped. The dynamical tide, on the other hand, typically possesses less energy (except in the case of extreme resonances), but involves smaller-wavelength modes that can thus be damped more effectively. Whether the dynamical or equilibrium tide provides the dominant source of tidal dissipation depends upon the application in question.

The first *a priori* theoretical calculation of the dynamical tide's dissipation efficiency in stars was performed by Zahn (1975), who computed the linear fluid response of a star to periodic tidal forcing. Witte & Savonije (1999) took this a step further, and integrated the coupled orbital and spin evolution equations in response to a time-varying tidal torque. In so doing, they discovered the phenomenon of resonance locking, which will be described in great detail in chapters 3 and 4.

This dissertation extends tidal theory in several ways. First, chapter 2, which was separately published as Burkart et al. (2012), develops a theoretical framework for predicting and interpreting photometric observations of tides in eccentric binaries, and applies these theoretical results to the *Kepler* system KOI-54 (Welsh et al. 2011).

Chapter 3 focuses on the tidal evolution of a white dwarf binary inspiraling due to the emission of gravitational waves, and was separately published as Burkart et al. (2013). Prior work applied the theory of the equilibrium tide to this problem (Willems et al. 2010); we extend these results to model the dynamical tide, which we find to be far more important than the equilibrium tide in white dwarf binaries. One of our key questions is whether tides cause white dwarfs to rotate synchronously even as their orbital motion speeds up due to gravitational wave induced orbital decay. Another question is how much orbital energy is dissipated as heat in each white dwarf, and what happens to this thermal energy. These results are important for interpreting observations of close white dwarf binaries and for understanding their thermal and rotational state prior to merger.

Lastly, in chapter 4 we give a detailed description and theoretical analysis of tidal resonance locking. In prior calculations of resonance locking, studies such as Witte & Savonije (1999) invoked approximations in order to determine the amplitudes of stellar eigenmodes (see § 4.6.1); these approximations correspond to assuming that each eigenmode is relatively rapidly damped. We instead allow eigenmodes to possess fully dynamical mode amplitudes that are self-consistently coupled to the orbital and spin evolution of the body in question, and determine what form resonance locking takes with these more realistic assumptions. These results are applicable to many different astrophysical systems, including white dwarf binaries, eccentric stellar binaries, and eccentric planetary companions.

Chapter 2

Tidal asteroseismology: Kepler's KOI-54

2.1 Introduction

The recently discovered Kepler system KOI-54 (Welsh et al. 2011; henceforth W11) is a highly eccentric stellar binary with a striking lightcurve: a 20-hour 0.6% brightening occurs with a periodicity of 41.8 days, with lower-amplitude perfectly sinusoidal oscillations occurring in between. Such observations were only possible due to the unprecedented photometric precision afforded by Kepler. W11 arrived at the following interpretation of these phenomena: during the periastron passage of the binary, each of its two similar A stars is maximally subjected to both its companion's tidal force and radiation field. The tidal force causes a prolate ellipsoidal distortion of each star known as the equilibrium tide, so that the resulting perturbations to both the stellar cross section and the emitted stellar flux produce a change in the observed flux. Along with the effects of irradiation, this then creates the large brightening at periastron. Secondly, the strong tidal force also resonantly excites stellar eigenmodes during periastron, which continue to oscillate throughout the binary's orbit due to their long damping times; this resonant response is known as the dynamical tide.

W11 successfully exploited KOI-54's periastron flux variations, known traditionally as ellipsoidal variability, by optimizing a detailed model against this component of KOI-54's lightcurve (Orosz & Hauschildt 2000). In this way, W11 were able to produce much tighter constraints on stellar and orbital parameters than could be inferred through traditional spectroscopic methods alone. W11 also provided data on the dynamical tide oscillations. Thirty such pulsations were reported, of which roughly two-thirds have frequencies at exact harmonics of the orbital frequency. It is the analysis of these and similar future data that forms the basis of our work.

In close binary systems, tides provide a key mechanism to circularize orbits and synchronize stellar rotation with orbital motion. An extensive literature exists on the theory of stellar tides (e.g., Zahn 1975; Goodman & Dickson 1998; Witte & Savonije 1999). We have synthesized this theoretical formalism, together with other aspects of stellar oscillation theory, in order to model the dynamical tide of KOI-54 as well as to provide a framework for interpreting other similar systems.

The methods we have begun to develop are a new form of asteroseismology, a long-standing subject with broad utility. In traditional asteroseismology, we observe stars in which internal stellar processes (e.g., turbulent convection or the kappa mechanism) drive stellar eigenmodes, allowing them to achieve large amplitudes (Christensen-Dalsgaard 2003). In this scenario, modes ring at their natural frequencies irrespective of the excitation mechanism. The observed frequencies (and linewidths) thus constitute the key information in traditional asteroseismology, and an extensive set of theoretical techniques exist to invert such data in order to infer stellar parameters and probe different aspects of stellar structure (Unno et al. 1989).

In tidal asteroseismology of systems like KOI-54, however, we observe modes excited by a periodic tidal potential from an eccentric orbit; tidal excitation occurs predominantly at $l = 2$ (§ 2.3.2). Since orbital periods are well below a star's dynamical timescale, it is g-modes (buoyancy waves) rather than higher-frequency p-modes (sound waves) that primarily concern us. Furthermore, since modes in our case are *forced* oscillators, they do not ring at their natural eigenfrequencies, but instead at pure harmonics of the orbital frequency. (We discuss nonharmonic pulsations in § 2.6.5.) It is thus pulsation amplitudes and phases that provide the key data in tidal asteroseismology.

This set of harmonic amplitudes and phases in principle contains a large amount of information. One of the goals for future study is to determine exactly how the amplitudes can be optimally used to constrain stellar properties, e.g., the radial profile of the Brunt-Väisälä frequency. In this work, however, we focus on the more modest tasks of delineating the physical mechanisms at work in eccentric binaries and constructing a coherent theoretical model and corresponding numerical method capable of quantitatively modeling their dynamical tidal pulsations.

This paper is organized as follows. In § 2.2 we give essential background on KOI-54. In § 2.3 we give various theoretical results that we rely on in later sections, including background on tidal excitation of stellar eigenmodes (§ 2.3.2), techniques for computing disk-averaged observed flux perturbations (§ 2.3.3), and background on including the Coriolis force using the traditional approximation (§ 2.3.4). In § 2.4 we use these results to qualitatively explain the pulsation spectra of eccentric stellar binaries, particularly what governs the range of harmonics excited. In § 2.5 we confront the rotational evolution of KOI-54's stars, showing that they are expected to have achieved a state of stochastic pseudosynchronization.

In § 2.6 we present the results of our more detailed modeling. This includes an analytic model of ellipsoidal variability (§ 2.6.1), the effects of nonadiabaticity (§ 2.6.2), the effects of fast rotation (§ 2.6.3), and a preliminary optimization of our nonadiabatic method against KOI-54's pulsation data (§ 2.6.4). We show in § 2.6.5 that the observed nonharmonic pulsations in KOI-54 are well explained by nonlinear three-mode coupling, and perform estimates of instability thresholds, which may limit the amplitudes modes can attain. We also address whether the highest-amplitude observed harmonics in KOI-54 are signatures of resonant synchronization locks in § 2.6.6. We present our conclusions and prospects for future work in § 2.7.

A few weeks prior to the completion of this manuscript, we became aware of a complementary study of KOI-54's pulsations (Fuller & Lai 2011).

Table 2.1: List of KOI-54 system parameters as determined by W11. Selected from Table 2 of W11. The top rows contain standard observables from stellar spectroscopy, whereas the bottom rows result from W11's modeling of photometric and radial velocity data. Symbols either have their conventional definitions, or are defined in § 2.3.1. Note that W11's convention is to use the less-massive star as the primary.

	parameter	value	error	unit
Observations	T_1	8500	200	K
	T_2	8800	200	K
	L_2/L_1	1.22	0.04	
	$v_{\mathrm{rot},1}\sin i_1$	7.5	4.5	km/s
	$v_{\mathrm{rot},2}\sin i_2$	7.5	4.5	km/s
	$[\mathrm{Fe/H}]_1$	0.4	0.2	
	$[\mathrm{Fe/H}]_2$	0.4	0.2	
Lightcurve/RV modeling	M_2/M_1	1.025	0.013	
	P_{orb}	41.8051	0.0003	days
	e	0.8342	0.0005	
	ω	36.22	0.90	degrees
	i	5.52	0.10	degrees
	a	0.395	0.008	AU
	M_1	2.32	0.10	$M_\odot$
	M_2	2.38	0.12	$M_\odot$
	R_1	2.19	0.03	$R_\odot$
	R_2	2.33	0.03	$R_\odot$

2.2 Background on KOI-54

Table 2.1 gives various parameters for KOI-54 resulting from W11's observations and modeling efforts. Table 2.2 gives a list of the pulsations W11 reported, including both frequencies and amplitudes.

2.2.1 Initial rotation

KOI-54's two components are inferred to be A stars. Isolated A stars are observed to rotate much more rapidly than e.g. the Sun, with typical surface velocities of ~ 100 km/s and rotation periods of ~ 1 day (Adelman 2004). This results from their lack of a significant convective envelope, which means they experience less-significant magnetic braking, allowing them to retain more of their initial angular momentum as they evolve onto the main sequence. We thus operate under the assumption that both component stars of KOI-54 were born with rotation periods of roughly

$$P_{\mathrm{birth}} \approx 1 \text{ day}.$$

Table 2.2: Thirty largest KOI-54 pulsations. Originally Table 3 from W11. Asterisks ($*$) denote pulsations which are not obvious harmonics of the orbital frequency.

ID	amp. (μmag)	$\omega/\Omega_{\rm orb}$	
F1	297.7	90.00	
F2	229.4	91.00	
F3	97.2	44.00	
F4	82.9	40.00	
F5	82.9	22.42	$*$
F6	49.3	68.58	$*$
F7	30.2	72.00	
F8	17.3	63.07	$*$
F9	15.9	57.58	$*$
F10	14.6	28.00	
F11	13.6	53.00	
F12	13.4	46.99	
F13	12.5	39.00	
F14	11.6	59.99	
F15	11.5	37.00	
F16	11.4	71.00	
F17	11.1	25.85	$*$
F18	9.8	75.99	
F19	9.3	35.84	$*$
F20	9.1	27.00	
F21	8.4	42.99	
F22	8.3	45.01	
F23	8.1	63.09	$*$
F24	6.9	35.99	
F25	6.8	60.42	$*$
F26	6.4	52.00	
F27	6.3	42.13	$*$
F28	5.9	33.00	
F29	5.8	29.00	
F30	5.7	48.00	

2.2.2 Rotational inclination

W11 constrained both stars' rotation, via line broadening, to be $v_{\rm rot} \sin i_* = 7.5 \pm 4.5$ km/s (the same for both stars). Using the mean values of R_1 and R_2 obtained from W11's modeling, we can translate this into the following constraints on rotation periods (in days):

$$9.2 < P_1/\sin i_1 < 37 \qquad \text{and} \qquad 9.8 < P_2/\sin i_2 < 39,$$

where (i_1, i_2) and (P_1, P_2) are the rotational angular momentum inclinations with respect to the observer and the stellar rotation periods, respectively. If we assume that tidal interactions cause both stellar rotation periods to be approximately equal to the pseudosynchronous period of $P_{\rm ps} \sim 1.8$ days derived in § 2.5, we can constrain i_1 and i_2:

$$2.8^\circ < i_1 < 11^\circ \qquad \text{and} \qquad 2.6^\circ < i_2 < 11^\circ.$$

W11 obtained $i_{\rm orb} = 5.52^\circ \pm 0.10$ by fitting the lightcurve's ellipsoidal variation together with radial velocity measurements, so the constraints just derived are consistent with alignment of rotational and orbital angular momenta,

$$i = i_{\rm orb} = i_1 = i_2. \tag{2.1}$$

Tides act to drive these three inclinations to be mutually parallel or antiparallel, so such an alignment once achieved is expected to persist indefinitely. In order to simplify the analytical formalism as well as reduce the computational expense of modeling the observed pulsations, we will adopt equation (2.1) as an assumption for the rest of our analysis.

2.3 Theoretical Background

In this section we review various heterogeneous theoretical results that we rely on in later sections. In § 2.3.1 we summarize the conventions and definitions used in our analysis. In § 2.3.2 we review the theory of tidally forced adiabatic stellar eigenmodes. Later (§ 2.4), we use this formalism to explain qualitative features of the lightcurves of eccentric binaries like KOI-54. We also use adiabatic normal modes to compute tidal torques (§ 2.5 and Appendix A.3), as well as to perform a nonlinear saturation calculation (§ 2.6.5). However, our detailed quantitative modeling of the observations of KOI-54 utilizes a nonadiabatic tidally forced stellar oscillation method that we introduce and employ in § 2.6.

In § 2.3.3 we summarize how perturbed quantities at the stellar photosphere, specifically the radial displacement and Lagrangian flux perturbation, can be averaged over the stellar disk and translated into an observed flux variation. Lastly, in § 2.3.4 we review the traditional approximation, a way of simplifying the stellar oscillation equations in the presence of rapid rotation.

2.3.1 Conventions and definitions

We label the two stars as per Table 2.1, consistent with W11; note that the primary/star 1 is taken to be the smaller and less massive star. In the following, we focus our analysis on star 1, since the results for star 2 are similar. We assume that both stars' rotational angular momentum vectors are perpendicular to the orbital plane (§ 2.2.2), and work in spherical coordinates (r, θ, ϕ) centered on star 1 where $\theta = 0$ aligns with the system's orbital angular momentum and $\phi = 0$ points from star 1 to star 2 at periastron.

We write the stellar separation as $D(t)$ and the true anomaly as $f(t)$, so that the position of star 2 is $D = (D, \pi/2, f)$. We write the semi-major axis as a and the eccentricity as e. The angular position of the observer in these coordinates is $\hat{n}_o = (\theta_o, \phi_o)$, where these angles are related to the traditional inclination i and argument of periastron ω by (Arras et al. 2012)

$$\theta_o = i \qquad \text{and} \qquad \phi_o = \frac{\pi}{2} - \omega \mod 2\pi. \tag{2.2}$$

The orbital period [angular frequency] is $P_{\rm orb}$ [$\Omega_{\rm orb}$], while a rotation period [angular frequency] is P_* [Ω_*]. The effective orbital frequency at periastron is

$$\Omega_{\rm peri} = \left.\frac{df}{dt}\right|_{f=0} = \frac{\Omega_{\rm orb}}{1-e}\sqrt{\frac{1+e}{1-e}}, \tag{2.3}$$

which is $\Omega_{\rm peri} = 20. \times \Omega_{\rm orb}$ for KOI-54. The stellar dynamical frequency is

$$\omega_{\rm dyn} = \sqrt{\frac{GM}{R^3}}, \tag{2.4}$$

which is $\omega_{\rm dyn} \approx 1.1$ rad/hr for KOI-54's stars.

2.3.2 Tidal excitation of stellar eigenmodes

Although we ultimately use an inhomogeneous, nonadiabatic code including the Coriolis force to model the pulsations in eccentric binaries (§ 2.6.2), the well known normal mode formalism provides an excellent qualitative explanation for many of the features in the lightcurve power spectra of systems such as KOI-54. Here we will review the salient results of this standard theory; we demonstrate their application to KOI-54 and related systems in §§ 2.4 – 2.5. The remainder of the paper after § 2.5 primarily uses our nonadiabatic method described in § 2.6.2.

Working exclusively to linear order and operating in the coordinates specified in the previous section, we can represent the response of star 1 (and similarly for star 2)—all oscillation variables such as the radial displacement ξ_r, the Lagrangian pressure perturbation Δp, etc.—to a perturbing tidal potential by a spatial expansion in normal modes and a temporal expansion in orbital harmonics (e.g., Kumar et al. 1995):

$$\delta X = \sum_{nlmk} A_{nlmk} \delta X_{nl}(r) e^{-ik\Omega_{\rm orb} t} Y_{lm}(\theta, \phi). \tag{2.5}$$

Here, $2 \leq l < \infty$ and $-l \leq m \leq l$ are the spherical harmonic quantum numbers, and index the angular expansion; $|n| < \infty$ is an eigenfunction's number of radial nodes, and indexes the radial expansion;[1] and $|k| < \infty$ is the orbital Fourier harmonic number, which indexes the temporal expansion.

Each (n, l, m) pair formally corresponds to a distinct mode, although the eigenspectrum is degenerate in m since for now we are ignoring the influence of rotation on the eigenmodes. Each mode has associated with it a set of eigenfunctions for the various perturbation variables, e.g., ξ_r, δp, etc., as well as a frequency ω_{nl} and a damping rate γ_{nl}. For stars and modes of interest, γ_{nl} is set by radiative diffusion; see the discussion after equation (2.17). Figure 2.1 gives a propagation diagram for a stellar model consistent with W11's mean parameters for star 1 (Table 2.1). The frequencies of g-modes behave asymptotically for $n \gg 0$ and hence $\omega_{nl} \ll \omega_{\rm dyn}$ as (Christensen-Dalsgaard 2003)

$$\omega_{nl} \sim \omega_0 \frac{l}{n}, \tag{2.6}$$

where $\omega_0 \approx 4$ rad/hr for KOI-54's stars.

The amplitudes A_{nlmk} appearing in equation (2.5) each represent the pairing of a stellar eigenmode with an orbital harmonic. Their values are set by the tidal potential, and can be expressed analytically:

$$A_{nlmk} = \frac{2\,\varepsilon_l\, Q_{nl}\, \widetilde{X}^k_{lm}\, W_{lm}\, \Delta_{nlmk}}{E_{nl}}. \tag{2.7}$$

The coefficients appearing in equation (2.7) are as follows.

1. The tidal parameter ε_l is given by

$$\varepsilon_l = \left(\frac{M_2}{M_1}\right)\left(\frac{R_1}{D_{\rm peri}}\right)^{l+1}, \tag{2.8}$$

   where $D_{\rm peri} = a(1-e)$ is the binary separation at periastron. This factor represents the overall strength of the tide; due to its dependence on $R_1/D_{\rm peri}$, which is a small number in cases of interest, it is often acceptable to consider only $l = 2$.

[1] Conventionally, $n > 0$ corresponds to p-modes while $n < 0$ corresponds to g-modes; however, since we are mostly concerned with g-modes in this paper, we will report g-mode n values as > 0.

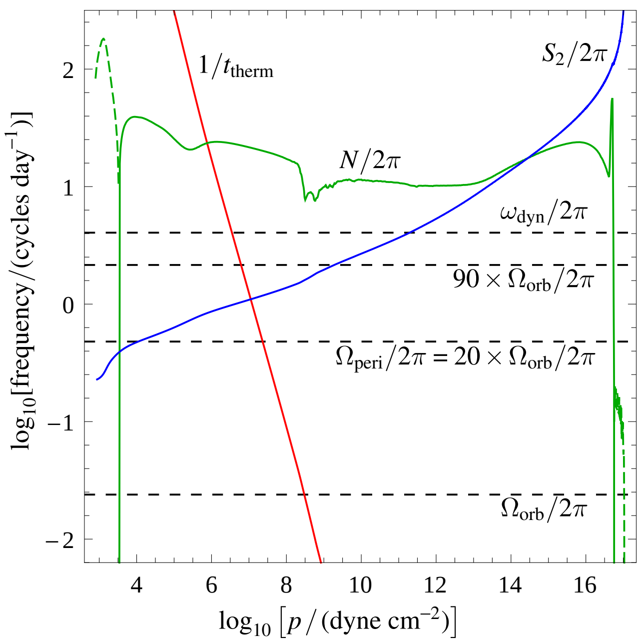

Figure 2.1: Propagation diagram for a MESA stellar model consistent with W11's mean parameters for star 1 of KOI-54, showing the radial profiles of the Brunt-Väisälä frequency N, the Lamb frequency $S_l = \sqrt{l(l+1)}c_s/r$ for $l = 2$ (where c_s is the sound speed), and the inverse thermal time $1/t_{\rm therm}$ (defined in equation 2.16). (N is dashed where $N^2 < 0$.) Propagation of g-modes occurs where the squared mode frequency ω_{nl}^2 is less than both N^2 and S_l^2 (Christensen-Dalsgaard 2003). Nonadiabatic effects become important when $\omega_{nl} \cdot t_{\rm therm} < 2\pi$. Several important frequencies for KOI-54 are also plotted, which are defined in § 2.3.1. The 90th harmonic is the largest pulsation observed (Table 2.2).

2. The linear overlap integral Q_{nl} (Press & Teukolsky 1977), given by

$$\begin{aligned} Q_{nl} &= \frac{1}{M_1 R_1^l} \int_0^{R_1} l \left(\xi_{r,nl} + (l+1)\xi_{h,nl} \right) \rho r^{l+1} dr \\ &= \frac{1}{M_1 R_1^l} \int_0^{R_1} \delta\rho_{nl}\, r^{l+2} dr \\ &= -\frac{R_1}{GM_1} \cdot \frac{2l+1}{4\pi} \cdot \delta\phi(R_1), \end{aligned} \tag{2.9}$$

represents the spatial coupling of the tidal potential to a given eigenmode; it is largest for modes with low $|n|$ and hence for eigenfrequencies close to the dynamical frequency $\omega_{\rm dyn} = \sqrt{GM_1/R_1^3}$, but falls off as a power law for $|n| \gg 0$.

3. We define our mode normalization/energy E_{nl} as

$$E_{nl} = 2 \left(\frac{\omega_{nl}^2 R_1}{GM_1^2} \right) \int_0^{R_1} \left(\xi_{r,nl}^2 + l(l+1)\xi_{h,nl}^2 \right) \rho r^2 dr, \tag{2.10}$$

where ξ_h is the horizontal displacement (Christensen-Dalsgaard 2003).

4. The unit-normalized Hansen coefficients $\widetilde{X}_{lm}^k$ are the Fourier series expansion of the orbital motion (Murray & Dermott 1999), and are defined implicitly by

$$\left(\frac{D_{\rm peri}}{D(t)} \right)^{l+1} e^{-imf(t)} = \sum_{k=-\infty}^{\infty} \widetilde{X}_{lm}^k(e) e^{-ik\Omega_{\rm orb} t}. \tag{2.11}$$

They are related to the traditional Hansen coefficients X_{lm}^k by $X_{lm}^k = \widetilde{X}_{lm}^k/(1-e)^{l+1}$ and satisfy the sum rule

$$\sum_{k=-\infty}^{\infty} \widetilde{X}_{lm}^k(e) = 1, \tag{2.12}$$

which can be verified using equation (2.11). (An explicit expression for X_{lm}^k is given in equation A.6.) The Hansen coefficients represent the temporal coupling of the tidal potential to a given orbital harmonic. They peak near $k_{\rm peak} \sim m\Omega_{\rm peri}/\Omega_{\rm orb}$ but fall off exponentially for larger $|k|$.

5. The Lorentzian factor Δ_{nlmk} is

$$\Delta_{nlmk} = \frac{\omega_{nl}^2}{\left(\omega_{nl}^2 - \sigma_{km}^2 \right) - 2i\gamma_{nl}\sigma_{km}} \tag{2.13}$$

where $\sigma_{km} = k\Omega_{\rm orb} - m\Omega_*$, and represents the temporal coupling of a given harmonic to a given mode. When its corresponding mode/harmonic pair approach resonance, i.e. $\omega_{nl} \approx \sigma_{km}$, Δ_{nlmk}

can become very large; its maximum, for a perfect resonance, is half the simple harmonic oscillator quality factor, q_{nl}: $\Delta_{\rm pr} = i\omega_{nl}/2\gamma_{nl} = iq_{nl}/2$.

6. W_{lm} is defined in equation (A.3) and represents the angular coupling of the tidal potential to a given mode; it is nonzero only for $\mathrm{mod}(l+m, 2) = 0$. In particular, $W_{2,\pm1} = 0$, meaning that $l = 2$, $|m| = 1$ modes are not excited by the tidal potential.

7. To calculate the quasiadiabatic damping rate γ_{nl} within the adiabatic normal mode formalism,[2] we average the product of the thermal diffusivity χ with a mode's squared wavenumber k^2, weighted by the mode energy:

$$\gamma_{nl} = \frac{\int_0^{r_c} k^2\chi(\xi_r^2 + l(l+1)\xi_h^2)\rho r^2 dr}{\int_0^{r_c}(\xi_r^2 + l(l+1)\xi_h^2)\rho r^2 dr}, \tag{2.14}$$

where the thermal diffusivity χ is

$$\chi = \frac{16\sigma T^3}{3\kappa\rho^2 c_p}. \tag{2.15}$$

The cutoff radius r_c is determined by the minimum of the mode's outer turning point and the point where $\omega_{nl} \cdot t_{\rm therm} = 2\pi$ (Christensen-Dalsgaard 2003), where the thermal time is

$$t_{\rm therm} = \frac{pc_pT}{gF}. \tag{2.16}$$

When this cutoff is restricted by the mode period intersecting the thermal time, so that strong nonadiabatic effects are present inside the mode's propagation cavity, the mode becomes a traveling wave at the surface, and the standing wave/adiabatic normal mode approximation becomes less realistic. This begins to occur at a frequency (in the rest frame of the star) of $\sim 50 \times \Omega_{\rm orb}$ for KOI-54, as can be seen in Figure 2.1. Fortunately, our calculations involving the normal mode formalism (§§ 2.5 & 2.6.5) center primarily on low-order modes that are firmly within the standing wave limit.

The g-mode damping rate scales roughly as

$$\gamma_{nl} \sim \gamma_0 n^s \sim \gamma_0 \left[l \left(\frac{\omega_0}{\omega_{nl}} \right) \right]^s, \tag{2.17}$$

where we have used the asymptotic g-mode frequency scaling from equation (2.6). In the standing wave regime, i.e. for $\omega_{nl} \gtrsim 50 \times \Omega_{\rm orb}$, we find that $\gamma_0 \sim 1\ \mathrm{Myr}^{-1}$ and $s \sim 4$. This large value for s results from the fact that most of the damping occurs at the surface, and the cutoff radius is limited by the outer turning point where the mode frequency intersects the Lamb frequency. As the mode frequency declines, the cutoff radius moves outward toward

[2] We only use this approximate method of calculating damping rates when employing the adiabatic normal mode formalism; our nonadiabatic method introduced in § 2.6.2 fully includes radiative diffusion.

smaller Lamb frequency and stronger damping, as can be seen in Figure 2.1. Without this behavior of the turning point, we would expect $s \sim 2$ since $k^2 \propto n^2$ in equation (2.14).

2.3.3 Observed flux perturbation

Throughout this work, perturbations to the emitted flux ΔF are understood to be bolometric, i.e. integrated over the entire electromagnetic spectrum. We correct for Kepler's bandpass to first order as follows. We define the bandpass correction coefficient $\beta(T)$ as the ratio of the bandpass-corrected flux perturbation $(\Delta F/F)_{\rm bpc}$ to the bolometric perturbation $(\Delta F/F)$, so that

$$\left(\frac{\Delta F}{F}\right)_{\rm bpc} = \beta(T)\left(\frac{\Delta F}{F}\right). \tag{2.18}$$

We assume Kepler is perfectly sensitive to the wavelength band $(\lambda_1, \lambda_2) = (400, 865)$ nm (Koch et al. 2010), and is completely insensitive to all other wavelengths. Then $\beta(T)$ is given to first order by

$$\beta(T) \approx \frac{\int_{\lambda_1}^{\lambda_2}(\partial B_\lambda/\partial \ln T)d\lambda}{4\int_{\lambda_1}^{\lambda_2} B_\lambda d\lambda}, \tag{2.19}$$

where $B_\lambda(T)$ is the Planck function. Using W11's mean parameters for KOI-54 (Table 2.1), we have $\beta(T_1) = 0.81$ and $\beta(T_2) = 0.79$. Note that employing β alone amounts to ignoring bandpass corrections due to limb darkening. We have also ignored the fact that in realistic atmospheres, the perturbed specific intensity depends on perturbations to gravity in addition to temperature; this is a small effect, however, as shown e.g. in Robinson et al. (1982).

For completeness, we transcribe several results from Pfahl et al. (2008), which allow a radial displacement field ξ_r and a Lagrangian perturbation to the emitted flux ΔF, both evaluated at the stellar surface, to be translated into a corresponding disk-averaged observed flux perturbation δJ, as seen e.g. by a telescope (Dziembowski 1977). While an emitted flux perturbation alters the observed flux directly, a radial displacement field contributes by perturbing a star's cross section.[3]

Given ξ_r and ΔF expanded in spherical harmonics as

$$\xi_r = \sum_{l=0}^{\infty}\sum_{m=-l}^{l} \xi_{r,lm}(t) Y_{lm}(\theta,\phi) \tag{2.20}$$

$$\Delta F = \sum_{l=0}^{\infty}\sum_{m=-l}^{l} \Delta F_{lm}(t) Y_{lm}(\theta,\phi), \tag{2.21}$$

[3]A horizontal displacement field ξ_h produces no net effect to first order—its influence cancels against perturbations to limb darkening, all of which is included in equation (2.22).

Table 2.3: First six disk-integral factors b_l and c_l from equations (2.23) and (2.24) for linear Eddington limb darkening, $h(\mu) = 1 + (3/2)\mu$.

l	b_l	c_l
0	1	0
1	17/24	17/12
2	13/40	39/20
3	1/16	3/4
4	−1/48	−5/12
5	−1/128	−15/64

we can translate these into a fractional observed flux variation $\delta J/J$ to first order by

$$\frac{\delta J}{J} = \sum_{l=0}^{\infty}\sum_{m=-l}^{l}\left[(2b_l - c_l)\frac{\xi_{r,lm}(t)}{R} + \beta(T)\, b_l \frac{\Delta F_{lm}(t)}{F(R)}\right] Y_{lm}(\theta_{\rm o}, \phi_{\rm o}), \tag{2.22}$$

where the disk-integral factors are

$$b_l = \int_0^1 \mu P_l(\mu) h(\mu)\, d\mu \tag{2.23}$$

$$c_l = \int_0^1 \left[2\mu^2 \frac{dP_l}{d\mu} - (\mu - \mu^3)\frac{d^2 P_l}{d\mu^2}\right] h(\mu)\, d\mu, \tag{2.24}$$

$P_l(\mu)$ is a Legendre polynomial, and $h(\mu)$ is the limb darkening function, normalized as $\int_0^1 \mu h(\mu) d\mu = 1$. For simplicity, we use Eddington limb darkening for all of our analysis, with $h(\mu) = 1 + 3\mu/2$; b_l and c_l in this case are given in Table 2.3 for $0 \le l \le 5$.

Since $Y_{2,\pm 2} \propto \sin^2\theta$ and $Y_{2,0} \propto (3\cos^2\theta - 1)$, and since KOI-54 has $\theta_o = i \approx 5.5°$ (Table 2.1), equation (2.22) shows that $m = \pm 2$ eigenmodes are a factor of ~ 200 less observable than $m = 0$ modes. It is thus likely that nearly all of the observed pulsations in KOI-54 have $m = 0$; the exceptions may be F1 and F2, as we discuss in § 2.6.6.

2.3.4 Rotation in the traditional approximation

Stellar rotation manifests itself in a star's corotating frame as the fictitious centrifugal and Coriolis forces (Unno et al. 1989). The centrifugal force directly affects the equilibrium structure of a star, which can then consequently affect stellar oscillations. Its importance, however, is characterized by $(\Omega_*/\omega_{\rm dyn})^2$, which is $\sim 10^{-2}$ for rotation periods and stellar parameters of interest here (§ 2.2). As such we neglect rotational modification of the equilibrium stellar structure (Ipser & Lindblom 1990).

The Coriolis force, on the other hand, affects stellar oscillations directly. Given a frequency of oscillation σ, the influence of the Coriolis force is characterized by the dimensionless rotation parameter q given by

$$q = 2\Omega_*/\sigma, \tag{2.25}$$

where large values of $|q|$ imply that rotation is an important effect that must be accounted for. Note that for simplicity we assume rigid-body rotation throughout. For the pulsations observed in KOI-54's lightcurve (Table 2.2), assuming both stars rotate at near the pseudosynchronous rotation period $P_{\rm ps} \sim 1.8$ days discussed in § 2.5.1 and that $m = 0$ (justified in the previous section), q ranges from 0.5 for $k = \sigma/\Omega_{\rm orb} = 90$ to 1.5 for $k = 30$. Thus lower harmonics fall in the nonperturbative rotation regime, where rotation is a critical effect that must be fully included.

The "traditional approximation" (Chapman & Lindzen 1970) greatly simplifies the required analysis when the Coriolis force is included in the momentum equation. In the case of g-modes, it is applicable for

$$1 \gg \frac{2}{q} \cdot \frac{R}{H_p} \cdot \left(\frac{\Omega_*}{|N|}\right)^2, \tag{2.26}$$

where $H_p = \rho g/p$ is the pressure scale height; outside of the convective cores of models we are concerned with in this work (where g-modes are evanescent anyway), equation (2.26) is well satisfied whenever rotation is significant. Here we will give a brief overview of the traditional approximation; we refer to Bildsten et al. (1996) for a more thorough discussion.

The traditional approximation changes the angular Laplacian, which occurs when deriving the nonrotating stellar oscillation equations, into the Laplace tidal operator L^q_m. (Without the traditional approximation, the oscillation equations for a rotating star are generally not separable.) It is thus necessary to perform the polar expansion of oscillation variables in eigenfunctions of L^q_m, known as the Hough functions $H^q_{\lambda m}(\mu)$ (where $\mu = \cos\theta$), rather than associated Legendre functions; the azimuthal expansion is still in $e^{im\phi}$. The eigenvalues of L^q_m are denoted λ, and depend on m, the azimuthal wavenumber. In the limit that $q \to 0$, the Hough functions become ordinary (appropriately normalized) associated Legendre functions, while $\lambda \to l(l+1)$.

We present the inhomogeneous, tidally driven stellar oscillation equations in the traditional approximation in Appendix A.1.2. The principal difference relative to the standard stellar oscillation equations is that terms involving $l(l+1)$ either are approximated to zero, or have $l(l+1) \to \lambda$. This replacement changes the effective angular wavenumber. E.g., since the primary λ for $m = 0$ increases with increasing rotation, fast rotation leads to increased damping of $m = 0$ g-modes at fixed frequency, as discussed in § 2.6.3.

For strong rotation, $|q| > 1$, the Hough eigenvalues λ can be both positive and negative. The case of $\lambda > 0$ produces rotationally modified traditional g-modes, which evanesce for $\cos^2\theta > 1/q^2$. (Rossby waves or r-modes are also confined near the equator and have a small positive value of λ.) Instead, for $\lambda < 0$, polar modes are produced that propagate near the poles for $\cos^2\theta > 1/q^2$, but evanesce radially from the surface since they have an imaginary Lamb frequency $S_\lambda = \lambda^{1/2} c_s/r$ (as explained further in Figure 2.1).

2.4 Qualitative discussion of tidal asteroseismology

It is helpful conceptually to divide the tidal response of a star into two components, the *equilibrium tide* and the *dynamical tide* (Zahn 1975). Note that in this section we will again use the normal mode formalism described in § 2.3.2, even though our subsequent more detailed modeling of KOI-54 uses the inhomogeneous, nonadiabatic formalism introduced in § 2.6.2.

2.4.1 Equilibrium tide

The equilibrium tide is the "static" response of a star to a perturbing tidal potential, i.e., the large-scale prolation due to differential gravity from a companion. In terms of lightcurves, the equilibrium tide corresponds to ellipsoidal variability (along with the irradiation component of this effect discussed in Appendix A.2.1). In the case of an eccentric binary this manifests itself as a large variation in the observed flux from the binary during periastron. KOI-54's equilibrium tide was successfully modeled in W11, enabling precise constraints to be placed on various stellar and orbital parameters (Table 2.1).

In terms of the normal mode formalism developed in § 2.3.2, the equilibrium tide corresponds to the amplitudes from equation (2.7) tied to large overlaps Q_{nl} and large Hansen coefficients X^k_{lm}; in other words, to pairings of low-$|n|$ modes with low-$|k|$ orbital harmonics. The Lorentzian factor Δ_{nlmk} is typically ~ 1 for the equilibrium tide since it is not a resonant phenomenon.

In practice, however, it is much simpler and more convenient to use other mathematical formalisms to model the equilibrium tide, like taking the zero-frequency stellar response as in Appendix A.2.2, or filling Roche potentials as in W11's simulations. We show in § 2.6.1 that our simple analytical treatment of the equilibrium tide verifies the results from the sophisticated simulation code employed in W11.

2.4.2 Dynamical tide

The dynamical tide, on the other hand, corresponds to resonantly excited pulsations with frequencies equal to harmonics of the orbital frequency, $k\Omega_{\rm orb}$. W11 observed at least 21 such harmonics (Table 2.2).

For a circular orbit, the tidal potential has all its power in the $k = \pm 2$ orbital harmonics; in this case the only modes that can be resonantly excited are those with frequencies close to twice the Doppler-shifted orbital frequency: $\omega_{nl} \approx 2|\Omega_{\rm orb} - \Omega_*|$; this is typically only a single mode. This corresponds to the fact that the Hansen coefficients from equation (2.11) become a Kronecker delta at zero eccentricity: $\widetilde{X}^k_{lm}(0) = \delta^k_m$. However, for a highly eccentric orbit, the distribution of power in the Hansen coefficients, and hence the stellar response, can be much broader; as a result a wide array of different harmonics can be excited, allowing for a rich pulsation spectrum.

Mode excitation due to a tidal harmonic $k\Omega_{\rm orb}$ is modulated by the Doppler-shifted frequency $\sigma_{km} = k\Omega_{\rm orb} - m\Omega_*$. However, the frequencies at which modes are *observed* to oscillate, viewed from an inertial frame, are indeed pure harmonics of the orbital frequency, $k\Omega_{\rm orb}$.[4] We demonstrate this mathematically in Appendix A.1; intuitively, although a driving frequency experiences a Doppler shift upon switching to a star's corotating frame, the star's response is then Doppler shifted back upon observation from an inertial frame. In general, any time a linear system is driven at a particular frequency, it then also oscillates at that frequency, with its internal structure reflected only in the oscillation's amplitude and phase.

Whether a given mode is excited to a large amplitude is contingent on several conditions—essentially all the terms in equation (2.7). First, the overall strength of the tide, and hence the magnitude of observed flux variations, is determined by the tidal factor ε_l from equation (2.8). The dominant multipole order is $l = 2$, so we have $\varepsilon_2 = (M_2/M_1)(R_1/D_{\rm peri})^3$, where $D_{\rm peri} = a(1-e)$ is the binary separation at periastron, and we are focusing our analysis on star 1. For KOI-54, $\varepsilon_2 \simeq 4\times10^{-3}$ for both stars.

Next, the strength of a mode's resonant temporal coupling to the tidal potential is given by the Lorentzian factor Δ_{nlmk} in equation (2.13). Since this factor is set by how close a mode's frequency is to the nearest orbital harmonic, its effect is intrinsically random. The degree of resonance has an enormous effect on a mode's contribution to the observed flux perturbation, meaning that modeling the dynamical tide amounts on some level to adjusting stellar and system parameters in order to align eigenfrequencies against orbital harmonics so that the array of Lorentzian factors conspire to reproduce observational data.

Moreover, given a single observed pulsation amplitude together with theoretical knowledge of the likely responsible mode, i.e. the first four factors in equation (2.7), equating theoretical and observed pulsation amplitudes in principle yields direct determination of the mode's eigenfrequency, independently of the degree of resonance. This line of reasoning of course neglects the considerable theoretical uncertainties present, but serves to illustrate tidal asteroseismology's potential to constrain stellar parameters.

Despite the inherent unpredictability, a lightcurve's Fourier spectrum is still subject to restrictions imposed primarily by the remaining two factors in equation (2.7). These terms, the linear overlap integral Q_{nl} and the unit-normalized Hansen coefficient $\widetilde{X}^k_{lm}(e)$ (respectively equations 2.9 and 2.11), restrict the range in k over which harmonics can be excited; Figure 2.2 shows profiles of both. As discussed in § 2.3.2, Q_{nl} peaks for modes with frequencies near the dynamical frequency of the star $\omega_{\rm dyn}$ and falls off as a power law in frequency, whereas $\widetilde{X}^k_{lm}$ peaks for harmonics near $m\Omega_{\rm peri}/\Omega_{\rm orb}$ and falls off for higher k:

$$Q_{nl} \propto \omega_{nl}^p \qquad \omega_{nl} \ll \omega_{\rm dyn} \tag{2.27}$$

$$\widetilde{X}^k_{lm}(e) \propto \exp(-k/r) \qquad |k| \gg m\Omega_{\rm peri}/\Omega_{\rm orb}. \tag{2.28}$$

The power-law index p is 11/6 for g-modes in stars with a convective core and a radiative envelope or vice versa (Zahn 1970), and for KOI-54's eccentricity and $l = 2$ we find $r \sim 15$.

As a result, modes that can be excited are those with frequencies in the intervening region

[4] Welsh et al. (2011) incorrectly attributed nonharmonic pulsations to rotational splitting; we return to nonharmonic pulsations in § 2.6.5.

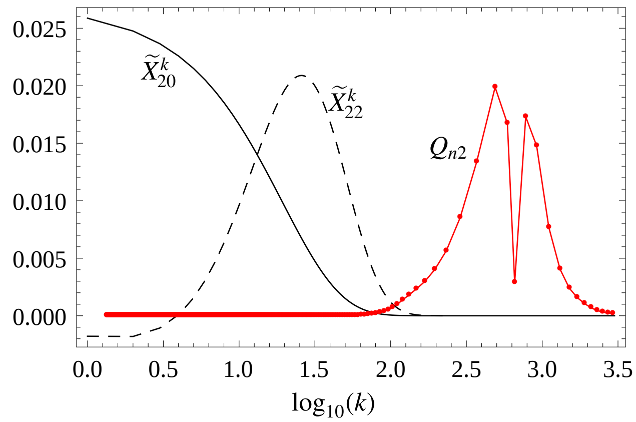

Figure 2.2: The linear overlap integral Q_{nl} and unit-normalized Hansen coefficients $\widetilde{X}^k_{lm}(e)$ as a function of $k = \omega/\Omega_{\rm orb}$ for $l = 2$ and $m = 0, 2$ (note the identity $\widetilde{X}^k_{lm} = \widetilde{X}^{-k}_{l,-m}$). Stellar and orbital parameters are fixed to W11's mean values for star 1; in particular, $e = 0.8342$. Each point on the curve for Q represents a normal mode with frequency $\omega_{nl} \simeq k\Omega_{\rm orb}$, thus neglecting any Doppler shift due to rotation. (See § 2.6.3 for a discussion of the influence of Doppler shifts.) Modes of a given m can be excited near where the overlap curve intersects the Hansen curve, at $\log_{10}(k) \approx 2.0$ in this plot.

between the peaks of Q_{nl} and X^k_{lm}, i.e.,

$$|m|\Omega_{\rm peri} < \omega_{nl} < \omega_{\rm dyn}. \tag{2.29}$$

This is a necessary but not sufficient condition; Figure 2.3 shows the product $Q_{nl}X^k_{lm}(e)$ at various eccentricities with stellar parameters as well as the periastron distance $D_{\rm peri}$ fixed to the mean values in W11, and hence with fixed tidal parameter ε_l (but consequently allowing the orbital period to vary). Although a chance close resonance can yield a large Lorentzian factor Δ_{nlmk}, excitation of modes far from the peak of $Q_{nl}\widetilde{X}^k_{lm}$ becomes less and less likely, since this quantity falls off sharply, especially towards larger $|k|$.

There are two other constraints on the range of harmonic pulsations that can be excited. First, the eigenmode density for g-modes scales asymptotically as

$$\left|\frac{dn}{dk}\right| \sim \frac{l}{k^2} \cdot \frac{\omega_{\rm dyn}}{\Omega_{\rm orb}}, \tag{2.30}$$

which shows that fewer modes exist at higher k. This can be seen by the spacing of points (which denote normal modes) in Figures 2.2 and 2.3, as well as by the spacing of peaks in Figure 2.6. This further limits the number of harmonics that can be excited at large k, in addition to the exponential decay of the Hansen coefficients discussed earlier, and thus effectively shifts the curves in Figure 2.3 toward lower k.

In addition, the Lorentzian factor Δ_{nlmk} is attenuated by mode damping γ_{nl}, which is set by radiative diffusion for high-order g-modes. Damping becomes larger with decreasing g-mode frequency due to increasing wavenumber; an asymptotic scaling is given in equation (2.17). Be-

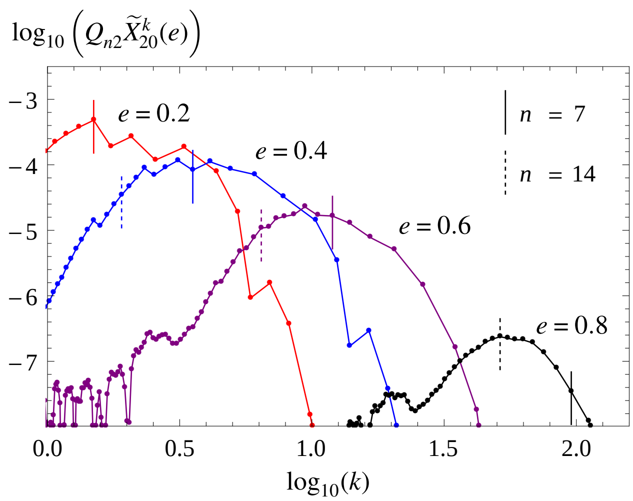

Figure 2.3: Plot of $Q_{nl}\widetilde{X}^k_{lm}(e)$ as a function of $k = \omega/\Omega_{\rm orb}$ for several eccentricities with $l = 2$, $m = 0$, and all stellar parameters as well as the periastron separation $D_{\rm peri}$ fixed to W11's mean values for star 1 (Table 2.1). Fixing $D_{\rm peri}$ fixes the tidal factor ε_l from equation (2.8) and hence the overall strength of the tide (although the orbital period consequently varies). Each point represents a normal mode; Hansen coefficients are evaluated with k given by the integer nearest to $\omega_{nl}/\Omega_{\rm orb}$ for each eigenmode. Solid vertical lines denote the $n = 7$ g-mode (the g-mode with 7 radial nodes), while dashed vertical lines are $n = 14$. Note that the finer eigenfrequency spacing at small k allows for larger amplitudes, which is not accounted for in this plot; including this effect would shift the curves toward lower k.

cause the Lorentzian response is proportional to γ_{nl}^{-1} at perfect resonance, the amplitudes of lower-frequency modes/harmonics are diminished by increased damping, in addition to the power-law decay of the tidal overlap. This effect is critical for understanding the influence of rotation on lightcurve power spectra, as we investigate in § 2.6.3.

2.4.3 Pulsation phases

Pulsation phases in eccentric binaries are essential information which should be fully modeled, in addition to the pulsation amplitudes reported in W11. For simplicity, we focus on a particular harmonic amplitude A_{nlmk} from equations (2.5) and (2.7) and assume it results from a close resonance so that $\omega_{nl} \approx \sigma_{km} = k\Omega_{\rm orb} - m\Omega_*$, assuming without loss of generality that $\sigma_{km} > 0$. We can then evaluate its phase ψ_{nlmk} relative to periastron, modulo π (since we are temporarily ignoring other factors contributing to the amplitude, which could introduce a minus sign), as

$$\begin{aligned}
\psi_{nlmk} &= \arg(A_{nlmk}) \\
&= \pi/2 - \arctan\left(\frac{\delta\omega(\omega_{nl}+\sigma_{km})}{2\gamma_{nl}\sigma_{km}}\right) \mod \pi \\
&\approx \pi/2 - \arctan(\delta\omega/\gamma_{nl}) \mod \pi,
\end{aligned} \tag{2.31}$$

where $\delta\omega = \omega_{nl} - \sigma_{km}$ is the detuning frequency.

For a near-perfect resonance, where $|\delta\omega| \lesssim \gamma_{nl}$, ψ_{nlmk} approaches $\pi/2$ (modulo π). However, if eigenmode damping rates are much smaller than the orbital frequency, then this intrinsic phase should instead be near 0. This is the case for KOI-54, where $\Omega_{\rm orb}/\gamma_{nl} > 10^3$ for modes of interest. Indeed, theoretically modeling the largest-amplitude 90th and 91st harmonics of KOI-54 assuming they are $m = 0$ modes requires only $|\delta\omega|/\gamma_{nl} \sim 20$, so that even these phases should be within $\sim 1\%$ of zero (modulo π).

The phase of the corresponding observed harmonic flux perturbation can be obtained from equation (2.31) by further including the phase of the spherical harmonic factor in the disk-averaging formula, equation (2.22):

$$\arg(\delta J_k/J) = \psi_{nlmk} + m\phi_o. \tag{2.32}$$

Summing over the complex conjugate pair, the observed time dependence is then $\cos[k\Omega_{\rm orb}t + (\psi_{nlmk} + m\phi_o)]$, where $t = 0$ corresponds to periastron. Thus if the observed pulsation's (cosine) phase is δ, the comparison to make is

$$\delta = (\psi_{nlmk} + m\phi_o) \mod \pi. \tag{2.33}$$

Nonetheless, since we have argued that $\psi_{nlmk} \approx 0$, this becomes

$$\delta \approx m\phi_o \mod \pi. \tag{2.34}$$

Given determination of ϕ_o (related to the argument of periastron ω by equation 2.2) by modeling of RV data or ellipsoidal variation, the phase of a resonant harmonic thus directly gives the mode's value of $|m|$ (which is very likely 0 or 2 for tidally excited modes, since $l = 2$ dominates). For KOI-54, phase information on harmonics 90 and 91 would thus determine whether they result from resonance locks, as discussed in the next section, or are simply chance resonances. Furthermore, knowing $|m|$ allows $m\phi_o$ to be removed from equation (2.33), yielding the pulsation's damping-to-detuning ratio.

However, the preceding treatment is only valid if the eigenfunction itself has a small phase: although eigenfunctions are purely real for adiabatic normal modes, local phases are introduced in a fully nonadiabatic calculation, as in § 2.6.2. Thus equations (2.32) – (2.34) are only applicable in the standing wave regime, where the imaginary part of the flux perturbation is small relative to the real part. In the traveling wave regime, the local wave phase near the surface becomes significant, and can overwhelm the contribution from global damping; see § 2.6.2. For KOI-54, this corresponds to $|k|$ below ~ 30, although this depends on the rotation rate (§ 2.6.3).

2.5 Rotational synchronization in KOI-54

Here we will discuss *a priori* theoretical expectations for KOI-54's stars' rotation. Later, in § 2.6.3, we will compare the results derived here with constraints imposed by the observed pulsation spectrum.

2.5.1 Pseudosynchronization

In binary systems, the influence of tides causes each component of the binary to eventually synchronize its rotational and orbital motions, just as with Earth's moon. Tides also circularize orbits, sending $e \to 0$, but the circularization timescale $t_{\rm circ}$ is much greater than the synchronization timescale $t_{\rm sync}$; their ratio is roughly given by the ratio of orbital to rotational angular momenta:

$$\begin{aligned} \frac{t_{\rm circ}}{t_{\rm sync}} &\sim \frac{L_{\rm orb}}{L_*} = \frac{\mu a^2}{I_*} \cdot \frac{\Omega_{\rm orb}}{\Omega_*} \cdot \sqrt{1-e^2} \\ &\sim \left(\frac{a}{R}\right)^2 \left(\frac{M_* R_*^2}{I_*}\right) (1-e)^2, \end{aligned} \tag{2.35}$$

where I_* is the stellar moment of inertia, μ is the reduced mass, and we have assumed for simplicity that the stars rotate at the periastron frequency $\Omega_{\rm peri}$ (§ 2.3.1). For KOI-54, this ratio is $\sim 10^3$.

Due to the disparity of these timescales, a star in an eccentric binary will first synchronize to a *pseudosynchronous period* $P_{\rm ps}$, defined as a rotation period such that no average tidal torque is exerted on either star over a sufficiently long timescale. If only the torque due to the equilibrium tide is used, and thus eigenmode resonances are neglected, then only one unique pseudosynchronous period exists, $P_{\rm ps}^{\rm nr}$, as derived in Hut (1981) and employed in W11. Its value for KOI-54 is (equation A.48)

$$P_{\rm ps}^{\rm nr} = (2.53 \pm 0.01) \text{ days}.$$

Inclusion of eigenmode resonances, however, complicates the situation. Figure 2.4 shows the secular tidal torque (averaged over one rotation period) for star 1 of KOI-54 plotted as a function of rotation frequency/period including contributions from both the equilibrium and dynamical tide. Although the general torque profile tends to zero at $P_{\rm ps}^{\rm nr}$, numerous other roots exist (displayed as vertical lines), where the torque due to a single resonantly excited eigenmode of the dynamical tide cancels against that due to the equilibrium tide. To produce this plot, we directly evaluated the secular tidal torque (Appendix A.3.1) using an expansion over the quadrupolar adiabatic normal modes of a MESA stellar model (Paxton et al. 2011) with parameters set by W11's mean values for star 1 of KOI-54 (Table 2.1). In our calculation we include both radiative (§ 2.3.2) and turbulent convective damping (Willems et al. 2010), but neglect rotational modification of the eigenmodes.

Next, of the many zeroes of the secular torque available, which are applicable? Continuing with the assumption that KOI-54's stars were born with rotation periods of $P_{\rm birth} \sim 1$ day (§ 2.2.1), with the same orientation as the orbital motion, one might naively posit that the first zero encountered by each star should constitute a pseudosynchronous period—it is an ostensibly stable spin state since small changes to either the stellar eigenmodes (via stellar evolution) or the orbital parameters (via circularization and orbital decay) induce a restoring torque. This is the basic idea behind a resonance lock (Witte & Savonije 1999).

However, this conception of resonance locking neglects two important factors. First, although the dynamical and equilibrium tidal torques may cancel, their energy deposition rates do not (in general); see Appendix A.3.1. Thus during a resonance lock the orbital frequency must continue to evolve, allowing other modes to come into resonance, potentially capable of breaking the lock. Second, as shown by Fuller & Lai (2011), it is necessary that the orbital frequency not evolve so quickly that the restoring torque mentioned earlier be insufficient to maintain the resonance lock. This restricts the range of modes capable of resonantly locking, introducing an upper bound on their inertial-frame frequencies and hence their orbital harmonic numbers (values of k in our notation).

Consequently, pseudosynchronization is in reality a complicated and dynamical process, consisting of a chain of resonance locks persisting until eventually $e \to 0$ and $P_* = P_{\rm orb}$. Such resonance lock chains were studied in much greater detail by Witte & Savonije (1999) for eccentric binaries broadly similar to KOI-54. As a result of the inherent complexity, a full simulation of KOI-54's orbital and rotational evolution is required in order to address the phenomenon of resonance locking and to derive theoretical predictions for the stars' spins. To perform such simulations, we again expanded the secular tidal torque and energy deposition rate over normal modes (detailed in Appendix A.3.1) using two MESA stellar models consistent with W11's mean parameters for KOI-54's two stars. We then numerically integrated the orbital evolution equations (Witte & Savonije 1999) assuming rigid-body rotation. We did not include the Coriolis force, nor did we address whether the eigenmode amplitudes required to produce the various resonance locks that arise are stable to nonlinear processes (§ 2.6.5).

Our simulations indicate that both stars should have reached pseudosynchronization states with rotation periods of $P_{\rm ps} \sim 1.8$ days; we discuss the synchronization timescale in more detail in § 2.5.2. These periods are $\sim 30\%$ faster than Hut's value of $P_{\rm ps}^{\rm nr} = 2.5$ days. The pseudosynchronization mechanism that operates is stochastic in nature, in which the dynamical tide's prograde resonance locks balance the equilibrium tide in a temporally averaged sense. This result appears

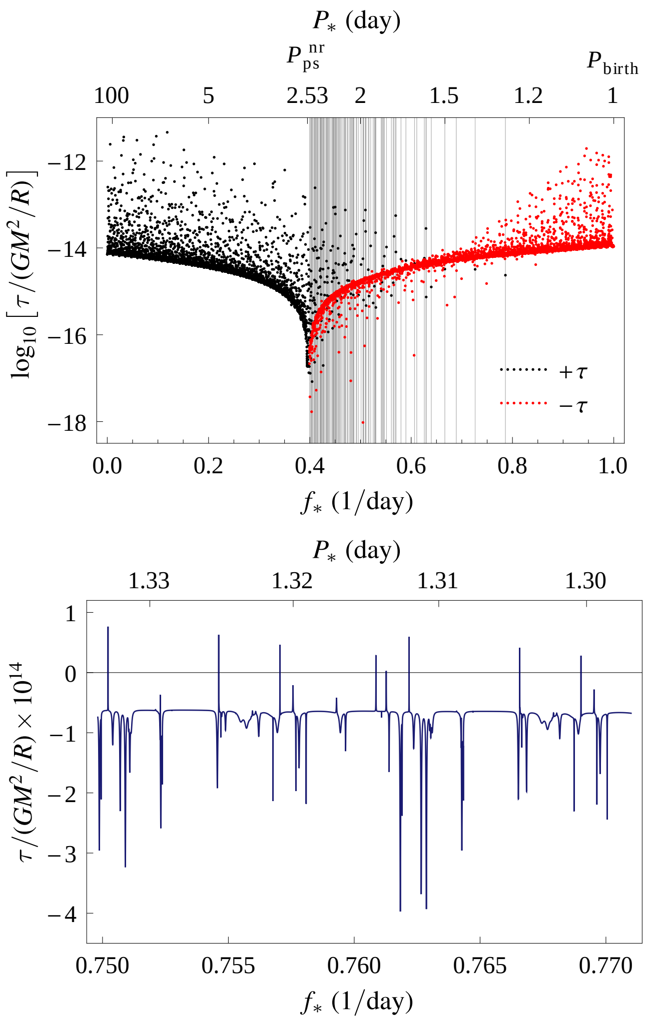

Figure 2.4: Plot of the secular tidal synchronization torque τ as a function of the rotational frequency $f_* = 1/P_*$ for star 1, using W11's parameters (Table 2.1). **Top panel:** Black indicates a positive torque (meaning increasing stellar spin), while red indicates a negative torque (decreasing stellar spin). The overall profile of τ goes to zero at Hut's value for the nonresonant pseudosynchronous period, $P_{\rm ps}^{\rm nr} = 2.53$ days for KOI-54, but eigenmode resonances create many additional zeroes, displayed as light gray vertical lines. (Determination of zeroes in this plot is limited by its grid resolution. Many more exist; see bottom panel.) **Bottom panel:** Zoom in, showing how narrow resonance spikes can cause the otherwise negative torque to become zero. The torque pattern roughly repeats at half the orbital frequency, $f_{\rm orb}/2 = 0.012$ day^{-1}, due to the fact that eigenmodes resonate with Doppler-shifted driving frequencies $\sigma_{km} = k\Omega_{\rm orb} - m\Omega_*$, with $m = \pm 2$ and $k \in \mathbb{Z}$.

independently of the initial rotation rates used; in other words, it is an attractor.

As described above, when a star is locked in resonance, it is the torque from a single highly resonant eigenmode that acts to oppose the equilibrium tide's nonzero torque. Such a high-amplitude mode should be easily observable. At first glance, this line of reasoning seems to provide a natural explanation for the presence of the large-amplitude 90th and 91st observed harmonics in KOI-54 (F1 and F2 from Table 2.2), namely that each is the photometric signature of the highly resonant eigenmode that produces a resonance lock for its respective star. There are several problems with this idea, however, which we elucidate in § 2.6.6.

2.5.2 Synchronization timescale

Where between the stars' putative birth rotation periods, $P_{\rm birth} = 1.0$ day, and the pseudosynchronous period from our simulations, $P_{\rm ps} \sim 1.8$ days, do we *a priori* expect the rotation periods of KOI-54's stars to fall? To this end, we can roughly estimate the synchronization timescale $t_{\rm sync}$ by integrating $I\dot{\Omega}_* = \tau(\Omega_*)$ to find

$$t_{\rm sync} \sim I \int_{\Omega_{\rm birth}}^{\Omega_{\rm ps}} \frac{d\Omega_*}{\tau(\Omega_*)}, \tag{2.36}$$

where I is the stellar moment of inertia, $\Omega_{\rm ps} = 2\pi/P_{\rm ps}$, and the tidal torque τ can as before be calculated as a function of the spin frequency Ω_* using an expansion over normal modes (Appendix A.3.1).

Using this approximation, we find $t_{\rm sync} \sim 80$ Myr, which is less than the inferred system age of $t_{\rm age} \sim 200$ Myr. This is consistent with our orbital evolution simulations (§ 2.5.1). Although stellar evolution was ignored in this calculation, a rough estimate of its effect can be made using only the fact that $t_{\rm sync}$ scales as R^{-3} (since the torque scales as R^5 while the moment of inertia scales as R^2). Given that both stars had 10% smaller radii at ZAMS (indicated by our modeling), this would lead to only at most a $3 \times 10\% = 30\%$ increase in $t_{\rm sync}$. Furthermore, both stars had much larger radii before reaching the main sequence, which would imply an even shorter synchronization time. Lastly, an important effect that arises when rotation is fully included is the existence of retrograde r-modes, which would also enhance the rate of stellar spindown (Witte & Savonije 1999). Thus the inequality

$$t_{\rm age} > t_{\rm sync}$$

seems to be well satisfied, and we expect that both stars' rotation periods should be close to the value of $P_{\rm ps} \sim 1.8$ days from § 2.5.1.

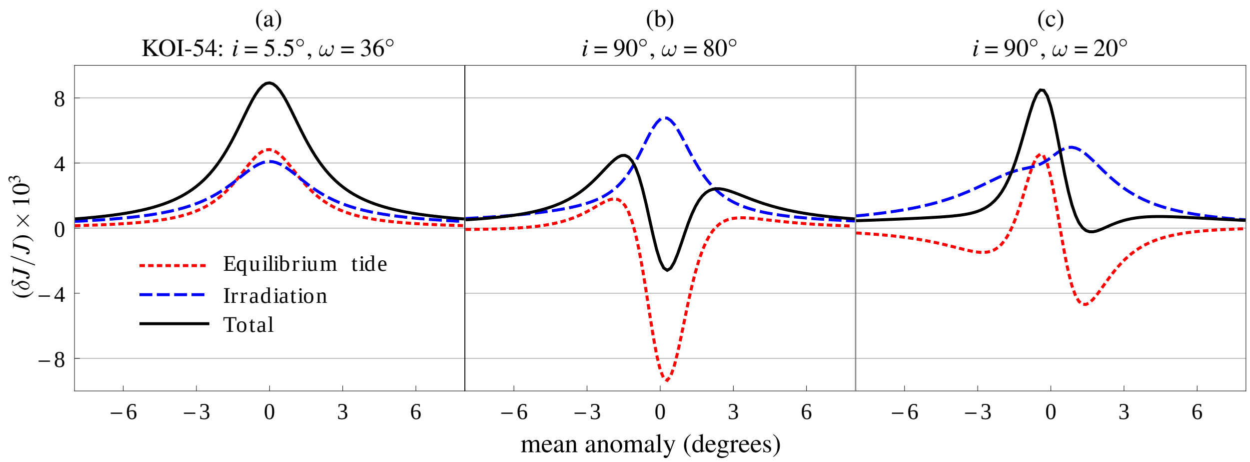

Figure 2.5: Simple analytic model of ellipsoidal variability detailed in Appendix A.2, including both the equilibrium tide (red dotted lines) and “reflection”/irradiation (blue dashed lines) components of the lightcurve. We used the best-fit parameters from W11 in all three panels (Table 2.1), except that we show two examples of edge-on orientations (ignoring the possibility of eclipses) in (b) & (c), effectively presenting KOI-54’s lightcurve as it would be observed from different angles. (We used $\omega = (80°, 20°)$ for (b, c) in order to demonstrate the asymmetric lightcurves possible depending on the binary’s orientation.) Panel (a) reproduces W11’s modeling and the data for KOI-54 to $\sim 20\%$. Our analytic model is easily applicable to many other systems. In § 2.6.3 we show that the dynamical tidal response, ignored here, may be larger than that due to the equilibrium tide for edge-on systems.

2.6 Results

2.6.1 Ellipsoidal variation

Figure 2.5.a shows our simple model of KOI-54's ellipsoidal variation; we adopted the best-fit parameters from W11's modeling (Table 2.1) to produce our lightcurve. Our irradiation (Appendix A.2.1, blue dashed line) and equilibrium tide (Appendix A.2.2, red dotted line) models are larger than W11's results by 24% and 14% respectively. The shapes of both curves are, however, essentially indistinguishable from W11's much more detailed calculations.

We attribute the small difference between our results and those of W11 to our simple model of the bandpass correction (equation 2.19) which ignores bandpass variations due to limb darkening. Such details could easily be incorporated into our analytical formalism, however, by introducing a wavelength-dependent limb darkening function $h_\lambda(\mu)$ in the disk integrals in equations (2.23) and (2.24) (Robinson et al. 1982). We thus believe that the models provided in Appendix A.2 should be quite useful for modeling other systems like KOI-54, due in particular to their analytic simplicity.

We also show in Figure 2.5.b & c what KOI-54's equilibrium tide and irradiation would look like for two edge-on orientations, demonstrating the more complicated, asymmetric lightcurve morphologies possible in eccentric binaries (see also the earlier work by Kumar et al. 1995). Future searches for eccentric binaries using Kepler and other telescopes with high-precision photometry should allow for the wide range of lightcurve shapes shown in Figure 2.5. We note, however, that that the dynamical tidal response, ignored in this section, may be larger than that due to the equilibrium tide for edge-on systems, as we show in § 2.6.3.

2.6.2 Nonadiabatic inhomogeneous method

Thus far our theoretical results have primarily utilized the tidally forced adiabatic normal mode formalism. Although this framework provides excellent intuition for the key physics in eccentric binaries, it is insufficient for producing detailed theoretical lightcurves, since this necessitates tracking a star's tidal response all the way to the photosphere where nonadiabatic effects are critical. To account for this, we employ the nonadiabatic inhomogeneous formalism originally used by Pfahl et al. (2008) (Appendix A.1.1), which we have extended to account for rotation in the traditional approximation (Appendix A.1.2).

Rather than decompose the response of the star into normal modes, the inhomogeneous method directly solves for the full linear response of the star to an external tidal force produced by a companion at a given forcing frequency. Given a stellar model, an orbital period, a set of orbital harmonics to act as driving frequencies, and a rigid-body rotation period, we solve the numerical problem described in Appendix A.1.2 for each star. This determines the various physical perturbation variables of the star as a function of radius, such as the radial displacement and the flux perturbation. For stars of interest we can safely ignore perturbations to the convective flux, so the only nonadiabatic effect is that produced by radiative diffusion.

Figure 2.6 shows the surface radial displacement ξ_r and Lagrangian emitted flux perturbation ΔF computed on a fine frequency grid, temporarily ignoring rotation; normal mode frequencies

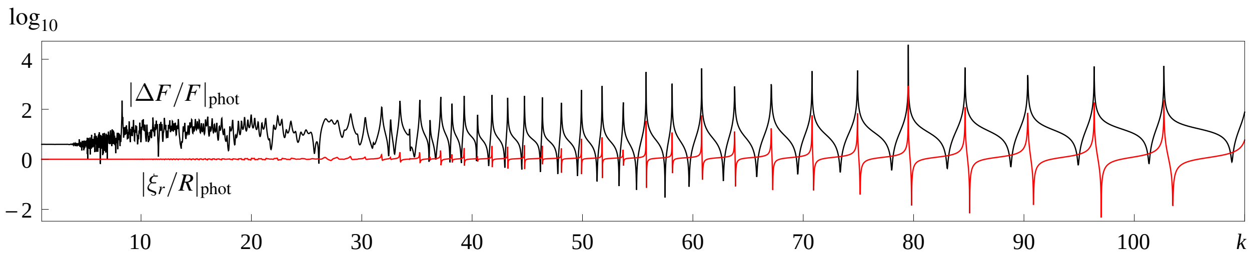

Figure 2.6: Amplitude of both the radial displacement ξ_r and Lagrangian flux perturbation ΔF evaluated at the photosphere as a function of $k = \omega/\Omega_{\rm orb}$ for a MESA model of star 1, using W11's best-fit parameters (Table 2.1). As a result of its larger amplitude, the Lagrangian flux perturbation has a much larger effect than the surface displacement on observed flux variations. Rotation is not included in this calculation. The radial dependence of the tidal potential is set to $U = -(GM_1/R_1)(r/R_1)^l$ with $l = 2$, which determines the vertical scale. Normal mode eigenfrequencies correspond to peaks in the curves. See the text for a discussion of the different regimes present in the stellar response for different forcing frequencies.

correspond to the resonant peaks in these curves. The surface radial displacement should approach its equilibrium tide value as the driving frequency tends to zero. Quantitatively, we find that this is true for orbital harmonics $k \lesssim 30$; note that in the units employed in Figure 2.6, this equilibrium tide value for ξ_r is $(\xi_r/R)^{\rm eq}_{\rm phot} = 1$ (Appendix A.2.2).

The surface flux perturbation shown in Figure 2.6, on the other hand, more clearly demonstrates the three qualitatively different regimes possible at the surface. First, the weakly damped standing wave regime, $k \gtrsim 30$, is characterized by strong eigenmode resonances and all perturbation variables having small imaginary parts. In Figure 2.1, this corresponds to the outer turning point, where the mode frequency intersects the Lamb frequency, lying inside the point where the mode frequency becomes comparable to the thermal frequency, so that the mode becomes evanescent before it becomes strongly nonadiabatic.

Next, the traveling wave regime, $5 \lesssim k \lesssim 30$, arises when modes instead propagate beyond where the mode and thermal frequencies become comparable, leading to rapid radiative diffusion near the surface. In the traveling wave limit, resonances become severely attenuated as waves are increasingly unable to reflect at the surface, and all perturbation variables have comparable real and imaginary parts (not including their equilibrium tide values).

Lastly, just as with the radial displacement, the flux perturbation also asymptotes to its overdamped equilibrium tide/von Zeipel value of $(\Delta F/F)^{\rm eq,vZ}_{\rm phot} = -(l+2)(\xi_r/R)^{\rm eq}_{\rm phot}$ (Appendix A.2.2) in the low-frequency limit, which is $|\Delta F/F|^{\rm eq,vZ}_{\rm phot} = |-l-2| = 4$ in Figure 2.6's units. Quantitatively, however, this only occurs for $k \lesssim 5$. At first glance, this suggests that the equilibrium tide modeling of KOI-54 in W11 and Figure 2.5 is invalid, since the equilibrium tide in KOI-54 has orbital power out to at least $k \sim 30$ (as can be seen e.g. in the plot of the Hansen coefficients for KOI-54's eccentricity in Figure 2.2).

Fortunately, as we describe in the next section, including rotation with a face-on inclination effectively stretches the graph in Figure 2.6 towards higher k. E.g., for $P_* = 2.0$ days, we find the equilibrium tide/von Zeipel approximation to hold for $k \lesssim 30$, justifying the simplifications used in W11 and Appendix A.2.2, although this may not apply for edge-on systems.

2.6.3 Effect of rotation on the dynamical tidal response

The most important effects of rotation in the context of tidal asteroseismology can be seen in Figure 2.7. Here we show the predicted flux perturbation for KOI-54 as a function of orbital harmonic k for four different rotation periods, having subtracted the equilibrium tide (Appendix A.2.2) to focus on resonant effects. [5] In Figure 2.7.a we use KOI-54's face-on inclination of $i = 5.5°$, while in Figure 2.7.b we use an inclination of $i = 90°$ to illustrate how a system like KOI-54 would appear if seen edge on; all other parameters are fixed to those from W11's modeling (and are thus not intended to quantitatively reproduce the data; see Figure 2.8 for an optimized model). The details of which specific higher harmonics have the most power vary as rotation changes mode eigenfrequencies, moving eigenmodes into and out of resonance. Nonetheless, several qualitative features can be observed.

For KOI-54's actual face-on orientation, as in Figure 2.7.a, rotation tends to suppress power in lower harmonics. This can be understood as follows. Primarily $m = 0$ modes are observable face on (§ 2.3.3). At fixed driving frequency σ, as the stellar rotation frequency Ω_*, and hence the Coriolis parameter $q = 2\Omega_*/\sigma$, increases in magnitude, $m = 0$ g-modes become progressively confined to the stellar equator (§ 2.3.4). As a result, these rotationally modified modes angularly couple more weakly to the tidal potential, diminishing their intrinsic amplitudes. Moreover, equatorial compression also corresponds to an increase in the effective multipole l, where $l \sim \sqrt{\lambda}$, and λ is a Hough eigenvalue from § 2.3.4 (e.g., Fig. 2 of Bildsten et al. 1996). Consequently, since g-modes asymptotically satisfy equation (2.6), the number of radial nodes n must increase commensurately. Larger n increases the radial wavenumber, which enhances the damping rate, further suppressing the resonant response of the modes and hence their contribution to the observed flux variation. This effectively corresponds to extending the highly damped traveling wave regime toward higher k in Figure 2.6.

As described in § 2.3.4, when the magnitude of the Coriolis parameter becomes greater than unity, a new branch of eigenmodes develops with negative Hough eigenvalues, $\lambda < 0$. These modes are confined to the stellar poles rather than the equator (Lindzen 1966). They also have an imaginary Lamb frequency, so that they are radially evanescent (explained further in Figure 2.1), and couple weakly to the tidal potential. We found negative-λ modes to produce only a small contribution to the stellar response, which increased with increasing rotation rate but which was roughly constant as a function of forcing frequency, thus mimicking the equilibrium tide. The role of these modes in the context of tidal asteroseismology should be investigated further, but for now we have neglected them in Figure 2.7.

For edge-on orbits, as in Figure 2.7.b, the situation is more complicated, and there are high-amplitude pulsations observable at all rotation periods. First, $m = 0$ modes very weakly affect edge-on lightcurves, since their Hansen coefficients (which peak at $k = 0$) do not intersect with the linear overlap integrals as strongly as for $m = 2$ modes (explained further in § 2.4.2 and shown in

[5] We assume that rotation is in the same sense as orbital motion throughout this section.

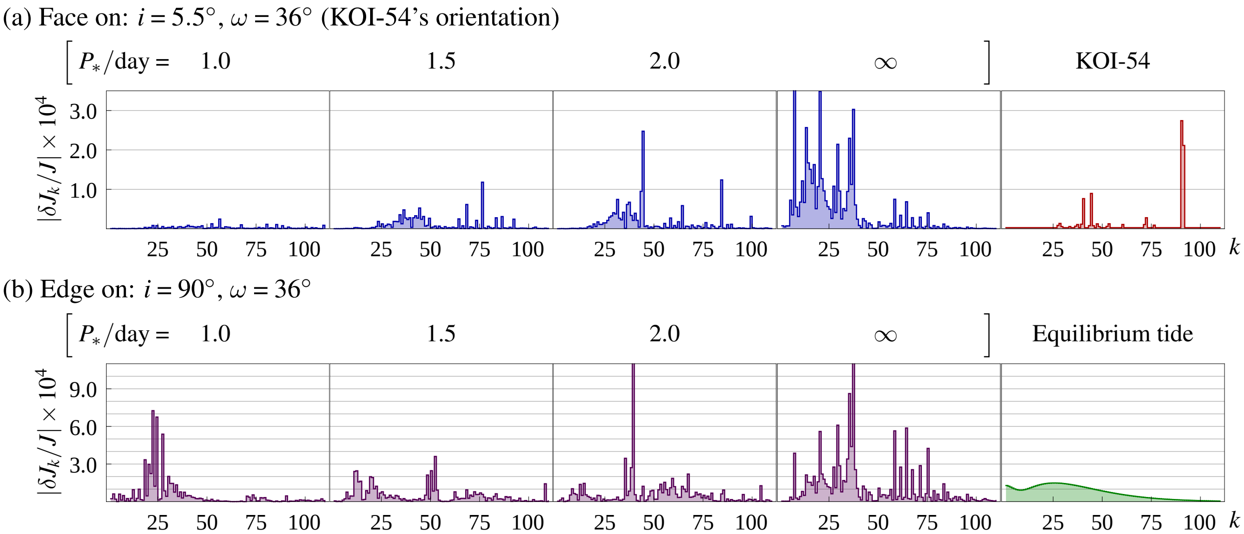

Figure 2.7: Influence of rotation on the lightcurve temporal power spectra of eccentric binaries. The eight leftmost plots show theoretical power spectra using fiducial stellar models and orbital parameters consistent with W11's mean values (Table 2.1), each as a function of orbital harmonic k. The top row uses KOI-54's known face-on inclination of $i = 5.5°$; the bottom row instead uses an edge-on inclination of $i = 90°$, showing how a system like KOI-54 would appear if viewed edge on. The vertical axis has different scales in the two rows. The effects of rotation on the stellar pulsations are included using the traditional approximation (§ 2.3.4). The equilibrium tide (Appendix A.2.2) has been subtracted in order to focus on resonant effects. We have not included negative-λ modes, as discussed in the text. (Note that parameters here have not been optimized to reproduce KOI-54's lightcurve; see Figure 2.8 for such a model.) The four leftmost columns show four different rigid-body rotation periods. **(a)** For a perfectly face-on orientation, only $m = 0$ modes can be observed (§ 2.3.3); however, larger rotation rates lead to equatorial compression of lower-frequency $m = 0$ g-modes, which increases the effective l and hence enhances the dissipation, leading to attenuated amplitudes. The rightmost panel shows the data for KOI-54, which is qualitatively most consistent with shorter rotation periods of 1.0 – 2.0 days, comparable to the pseudosynchronous period of ~ 1.8 days calculated in § 2.5. **(b)** For edge-on systems, a similar argument regarding rotational suppression of mode amplitudes applies, but instead near the Doppler-shifted harmonic $k = 2P_{\rm orb}/P_*$, rather than for k near zero for the $m = 0$ modes observable face on (see text for details). Comparison of the four left panels to the rightmost panel, which shows our simple analytical equilibrium tide model's harmonic decomposition (Appendix A.2.2), demonstrates that the dynamical tide can dominate the lightcurve in edge-on systems.

Figure 2.2). Similarly, modes with $m = -2$ have Hansen coefficients which peak near $-2\Omega_{\rm peri}/\Omega_{\rm orb}$ and are very small for $k \geq 0$.[6] Thus regardless of rotation, only $m = +2$ modes make significant lightcurve contributions.

Within the $m = +2$ modes, there are two regimes to consider: prograde modes excited by harmonics $k > 2\Omega_*/\Omega_{\rm orb}$ and retrograde modes with $k < 2\Omega_*/\Omega_{\rm orb}$ (see Appendix A.3.1). Prograde modes at a given corotating frame frequency are Doppler shifted toward large k, whereas the Hansen coefficients peak near $2\Omega_{\rm peri}/\Omega_{\rm orb}$, so their contribution to lightcurves is marginalized for fast rotation.

Retrograde, $m = +2$ g-modes with small corotating-frame frequencies $\sigma_{km} = k\Omega_{\rm orb} - m\Omega_*$ are subject to the same effect described earlier in the face-on case: they are suppressed by fast rotation due to weaker angular tidal coupling and stronger damping. The difference, however, is that although small driving frequencies are equivalent to small values of k for $m = 0$ modes, the Doppler shift experienced by $m = 2$ modes means that rotational suppression instead occurs for $k \sim 2\Omega_*/\Omega_{\rm orb}$, which is $84 \times ({\rm day}/P_*)$ for KOI-54's orbital period of 42 days. Figure 2.7.b demonstrates this, where e.g. little power can be observed near $k = 84$ for $P_* = 1$ day.

Furthermore, rotational suppression does *not* act on low-k harmonics in edge-on systems, as Figure 2.7.b also shows. Indeed, since fast rotation Doppler shifts lower-order retrograde modes—which radially couple more strongly to the tidal potential—toward values of k nearer to the Hansen peak of $\sim 2\Omega_{\rm peri}/\Omega_{\rm orb}$, the power in lower harmonics can even be *enhanced* by sufficiently fast rotation rates.

The rightmost panel of Figure 2.7.b shows the harmonic decomposition of our simple equilibrium tide model for an edge-on orientation, not including irradiation (§ 2.6.1; Appendix A.2.2). Comparing this plot to the left four panels shows in particular that, in edge-on orbits, the dynamical tide is not rotationally suppressed for harmonics where the equilibrium tide has large amplitudes, unlike for face-on orientations. Thus the ellipsoidal variation of edge-on systems may be buried beneath the dynamical tidal response. This implies that full dynamical modeling may be necessary to constrain system parameters for edge-on binaries, and that care must be taken in searches for eccentric binaries, since it cannot be assumed that their lightcurves will be dominated by ellipsoidal modulations.

2.6.4 Lightcurve power spectrum modeling

We performed preliminary quantitative modeling of the pulsation data in Table 2.2. As noted before, tidally driven pulsations should have frequencies which are pure harmonics of the orbital frequency, $\omega = k\Omega_{\rm orb}$ for $k \in \mathbb{Z}$. Although most of the pulsations W11 report are of this form, some clearly are not, and are as such unaccounted for in linear perturbation theory. Hence we only attempted to model pulsations within 0.03 in k of a harmonic (set arbitrarily); this limited our sample to 21 harmonics, as shown in Table 2.2. We provide an explanation for the nonharmonic pulsations in § 2.6.5.

[6] It is sufficient to consider only nonnegative k, i.e. to use a unimodal Fourier series, since the Fourier coefficient of orbital harmonic k must be the complex conjugate of that for $-k$, since the lightcurve is real valued.

There are eight primary parameters entering into our modeling of the remaining observed harmonics: stellar masses $M_{1,2}$, radii $R_{1,2}$, ZAMS metallicities $Z_{1,2}$, and rigid-body rotation periods $P_{1,2}$. To explore a range of stellar parameters, we used the stellar evolution code MESA (Paxton et al. 2011) to create two large sets of stellar models, one for each star, with ranges in M and R determined by W11's constraints (Table 2.1). We set both stars' metallicities to 0.04. The other two parameters, P_1 and P_2, were treated within our nonadiabatic code using the traditional approximation. We set $P_1 = P_2 = 1.5$ days, comparable to the expected pseudosynchronous rotation period (§ 2.5.1) and qualitatively consistent with the small-amplitude flux perturbations of lower harmonics seen in KOI-54 (§ 2.6.3). We fixed all of the orbital parameters to the mean values given in W11.

As discussed in § 2.6.6, it is possible that the 90th and 91st harmonics observed in KOI-54 are $m = \pm 2$ modes responsible for resonance locks, and are thus in states of nearly perfect resonance. Indeed, even if they are $m = 0$ chance resonances, which are ~ 200 times easier to observe with KOI-54's face-on orbital inclination than $m = \pm 2$ modes (§ 2.3.3), we find that a detuning of $|\delta\omega/\Omega_{\rm orb}| \sim 10^{-2}$ is required to reproduce the amplitude of either harmonic, where $\delta\omega$ is the difference between the eigenmode and driving frequencies (with $\delta\omega = 0$ representing a perfect resonance).

Such a close resonance represents a precise eigenfrequency measurement, and should place stringent constraints on stellar parameters. However, this degree of resonance is also very difficult to capture in a grid of stellar models because even changes in (say) mass of $\Delta M/M \sim 10^{-4}$ can alter the mode frequencies enough to significantly change the degree of resonance; future alternative modeling approaches may obviate this difficulty (§ 2.7). A second problem with trying to directly model the 90th and 91st harmonics is that the amplitudes of both of these harmonics may be set by nonlinear processes, as addressed in § 2.6.5. If correct, this implies that these particular modes strictly cannot be modeled using the linear methods we focus on in this paper.

We are thus justified in restricting our analysis to only those integral harmonics in the range $35 \leq k \leq 89$. We chose $k = 35$ as our lower bound to avoid modeling harmonics that contribute to ellipsoidal variation. We set $m = 0$ for all of our analysis for the reason stated above. We also only used $l = 2$ for the tidal potential, since additional l terms are suppressed by a) further powers of $R/D_{\rm peri} \sim 0.16$, and b) smaller disk-integral factors from § 2.3.3 (e.g., $b_3/b_2 = 0.2$).

To find a reasonable fit to the harmonic power observed in KOI-54, we attempted a simplistic, brute-force optimization of our model against the data: we first modeled the linear response of each stellar model in our grid separately, ignoring its companion, and calculated the resulting observed flux perturbations as a function of k. We then compared the absolute values of these flux perturbations to the observations of KOI-54 and selected the best 10^3 parameter choices (M,R) for each star. (In future work, pulsation phases should be modeled in addition to the amplitudes reported by W11, since this doubles the information content of the data; see also further discussion of phases in § 2.4.2.) Given this restricted set of stellar models, we computed the theoretical Fourier spectra for all 10^6 possible pairings of models.

Figure 2.8 shows one of our best fits to the observations of KOI-54; Table 2.4 gives the associated stellar parameters. We obtained many reasonable fits similar to Figure 2.8 with dissimilar stellar parameters, demonstrating that many local minima exist in this optimization problem. As a

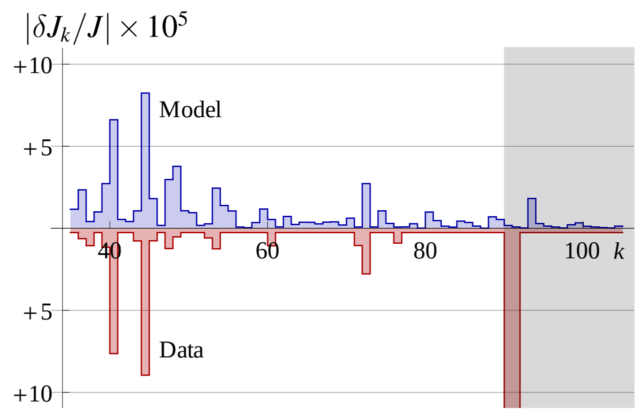

Figure 2.8: Exploratory modeling of the Fourier power spectrum of KOI-54's lightcurve. Our inhomogeneous theoretical model, including nonadiabaticity and rotation in the traditional approximation, is plotted above the graph's horizontal axis, while the data for KOI-54 (Table 2.2) is plotted below. Parameters corresponding to this plot are in Table 2.4. Since harmonics 90 & 91 represent extreme resonances, they are difficult to resolve in a given stellar model grid, and fits which reproduce their amplitudes cannot reproduce other parts of the Fourier spectrum. Thus we attempted to fit only $35 \le k \le 89$ and not the shaded region. Our fitting process was simplistic (see text), and we did not approach a full optimization, although our best fit does agree reasonably well with the data. Figure 2.9 shows the observed flux perturbation from this plot for both stars separately on a fine frequency grid.

Table 2.4: Stellar parameters used in Figures 2.8 and 2.9.

star	$M/M_\odot$	$R/R_\odot$	Z	P_*/day
1	2.278	2.204	0.04	1.5
2	2.329	2.395	0.04	1.5

result, Figure 2.8 and Table 2.4 should not be interpreted as true best fits but rather as an example of a model that can semi-quantitatively explain the observed harmonic power in KOI-54. We leave the task of using the observed pulsation data to quantitatively constrain the structure of the stars in KOI-54 to future work, as we discuss in § 2.7.

Responses from both stars were used to create the plot in Figure 2.8. Figure 2.9, on the other hand, uses the same parameters, but instead shows each star's observed flux perturbation separately and evaluated on a fine grid in frequency rather than only at integral orbital harmonics. As a result, Figure 2.9 exposes the position of normal modes (which correspond to peaks in the black curves) in relation to observed harmonics (shown as red vertical lines), as well as other features not captured in Figure 2.8's raw spectrum. Figure 2.9 also shows that harmonics 90 and 91 must come from different stars if they are indeed $m = 0$ g-modes (although this may not be the case; see § 2.6.6), since the g-mode spacing near $k \sim 90$ is much larger than the orbital period (with the same logic applying for harmonics 71 and 72).

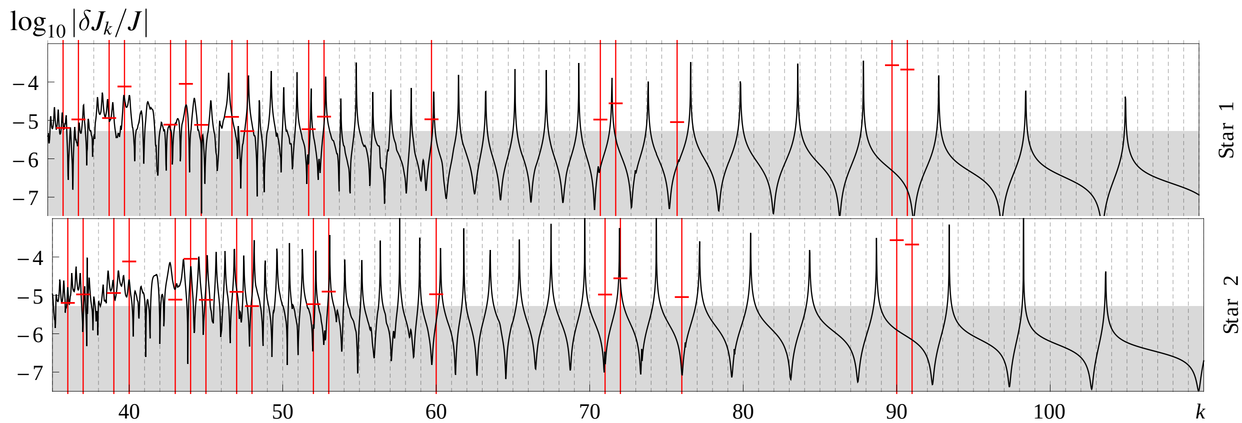

Figure 2.9: Individual stars' contributions to the Fourier spectrum from Figure 2.8 (black curves), evaluated on a fine grid in $k = \omega/\Omega_{\rm orb}$. The actual Fourier series decomposition (Figure 2.8) is obtained by adding both stellar responses (together with phases) at each integer value of k. Observed harmonics are displayed as red vertical lines, with short red horizontal lines indicating their amplitudes. We used a mesh of 50 points per unity increment in k to produce these plots, and find that the highest peaks of the eigenmode resonances nearest $k \sim 90$ are then at the same amplitude level as the observed 90th and 91st harmonics; this means that a detuning of $\Delta k = \delta\omega/\Omega_{\rm orb} \sim 0.02$ is required to explain these pulsations if they have $m = 0$ (see text). The regions below the minimum amplitude reported by W11 (Table 2.2) are shaded.

2.6.5 Nonharmonic pulsations: three-mode coupling

W11 report nine pulsations which are not obvious harmonics of the orbital frequency; these have asterisks next to them in Table 2.2. As we showed previously (§ 2.4.2 and Appendix A.1.1), these cannot be linearly driven modes. Here we present one possible explanation for the excitation of these pulsations.

To begin, we point out the following curious fact: the two highest-amplitude nonharmonic pulsations in Table 2.2 (F5 and F6) have frequencies which sum to 91.00 in units of the orbital frequency—precisely the harmonic with the second-largest amplitude (F2). (This is the only such instance, as we discuss below.)

Although this occurrence could be a numerical coincidence, it is strongly suggestive of parametric decay by nonlinear three-mode coupling, the essential features of which we now describe. First, however, we emphasize that the treatment we present here is only approximate. In reality, the process of nonlinear saturation is much more complicated, and a more complete calculation would involve fully coupling a large number of eigenmodes simultaneously (Weinberg & Quataert 2008).

If a parent eigenmode is linearly excited by the tidal potential to an amplitude that surpasses its three-mode-coupling threshold amplitude S_a, any energy fed into it above that value will be bled away into daughter mode pairs, each with frequencies that sum to the parent's oscillation frequency (Weinberg et al. 2012). In a tidally driven system, the sum of the daughter modes' frequencies must thus be a harmonic of the orbital frequency.

For a parent with indices $a = (n, l, m)$ linearly driven at a frequency σ, the threshold is given by

$$|S_a|^2 \simeq \min_{bc}\left(T_{abc}\right), \tag{2.37}$$

where

$$T_{abc} = \frac{\gamma_b \gamma_c}{4\omega_b \omega_c |\kappa_{abc}|^2}\left(1 + \frac{\delta\omega_{bc}^2}{(\gamma_a+\gamma_b)^2}\right), \tag{2.38}$$

ω_i is a mode frequency, γ_i is a mode damping rate, κ_{abc} is the normalization-dependent nonlinear coupling coefficient (Schenk et al. 2002), $\delta\omega_{bc} = \sigma - \omega_b - \omega_c$ is the detuning frequency, and the minimization is over all possible daughter eigenmodes b and c (each short for an (n, l, m) triplet).[7] The nonlinear coupling coefficient κ_{abc} is nonzero only when the selection rules

$$0 = \mathrm{mod}(l_a + l_b + l_c,\ 2), \tag{2.39}$$

$$0 = m_a + m_b + m_c, \tag{2.40}$$

$$|l_b - l_c| < \ l_a < l_b + l_c \tag{2.41}$$

are satisfied. Due to the second of these rules, any Doppler shifts due to rotation do not affect the detuning since they must cancel.

For a simple system of three modes, the nonlinear coupling's saturation can be determined analytically. The parent saturates at the threshold amplitude S_a, and the ratio of daughter energies within each pair is given by the ratio of the daughters' quality factors:

$$\frac{E_b}{E_c} = \frac{q_b}{q_c} = \frac{\omega_b/\gamma_b}{\omega_c/\gamma_c}. \tag{2.42}$$

Equations (2.37) and (2.38) exhibit a competition that determines which daughter pair will allow for the lowest threshold. At larger daughter l, modes are more finely spaced in frequency, since g-mode frequencies roughly satisfy the asymptotic scaling from equation (2.6); hence, the detuning $\delta\omega_{bc}$ becomes smaller (statistically) with increasing l. However, higher daughter l also leads to increased damping rates at fixed frequency (equation 2.17). As such, the minimum threshold will occur at a balance between these two effects.

In order to semi-quantitatively address the phenomenon of three-mode coupling in KOI-54, we produced an example calculation of S_a together with a list of best-coupled daughter pairs. To this end, we used a MESA stellar model (Paxton et al. 2011) consistent with the mean values of star 1's properties reported in W11 (Table 2.1). We computed this model's adiabatic normal modes using the ADIPLS code (Christensen-Dalsgaard 2008), and calculated each mode's global quasiadiabatic damping rate γ_{nl} due to radiative diffusion (§ 2.3.2).

We focus on the second-highest-amplitude $k = 91$ harmonic present in the data (F1 from Table 2.2) and set $\sigma = 91 \times \Omega_{\rm orb}$; as pointed out in W11, for $m_a = 0$ the quadrupolar eigenmode with natural frequency closest to the 91st orbital harmonic is the g_{14} mode, i.e., the g-mode with 14

[7] This section uses the normalization of Weinberg et al. (2012), whereas the rest of the paper uses the normalization given in § 2.3.2. We of course account for this when giving observable quantities.

Table 2.5: Ten best-coupled daughter mode pairs resulting from the procedure outlined in steps (i – iv) of § 2.6.5. This is an example calculation and is not meant to quantitatively predict the nonharmonic components of KOI-54's lightcurve. All frequencies and damping rates are in units of $\Omega_{\rm orb}$. The square root of the daughter quality factor ratio, $\sqrt{q_b/q_c}$, gives an estimate of the ratio of daughter mode amplitudes, and hence of their potential relative lightcurve contributions.

ID	$(l_b,n_b):(l_c,n_c)$	ω_b	ω_c	$\frac{1}{2}\log_{10}(q_b/q_c)$	$\log_{10}\lvert\delta\omega_{bc}\rvert$	$\log_{10}(2\sqrt{\gamma_b\gamma_c})$
P1	(2, -37) : (2, -23)	35.3	55.8	0.66	-1.4	-2.1
P2	(1, -25) : (3, -30)	29.9	61.0	0.057	-1.5	-2.5
P3	(1, -28) : (1, -11)	26.8	64.1	0.69	-1.3	-3.1
P4	(1, -50) : (3, -24)	15.3	75.7	1.2	-1.4	-1.7
P5	(1, -27) : (3, -29)	27.8	63.2	0.031	-1.4	-2.5
P6	(1, -42) : (3, -25)	18.0	73.1	1.2	-1.6	-1.7
P7	(1, -36) : (1, -10)	20.9	69.8	1.3	-0.61	-2.7
P8	(2, -35) : (2, -24)	37.2	53.7	0.51	-0.87	-2.2
P9	(2, -29) : (2, -28)	44.7	46.4	0.038	-0.99	-2.5
P10	(1, -35) : (1, -10)	21.5	69.8	1.2	-0.51	-2.8

radial nodes. We thus take this as our parent mode.

The minimization in equation (2.37) is over all normal modes, of which there is an infinite number. To make this problem tractable numerically, we essentially followed the procedure described in Weinberg & Quataert (2008):

1. We restricted daughter modes to $1 \le l \le 6$. There is no reason *a priori* to suggest l should be in this range, but, as shown in Table 2.5, $1 \le l \le 3$ turns out to be the optimum range for minimization in this particular situation, and modes with $l > 6$ are irrelevant.

2. The quantity to be minimized in equation (2.37), T_{abc}, achieves its minimum at fixed $\delta\omega_{bc}$ and κ_{abc} for $\omega_b \approx \omega_c$, given the scaling from equation (2.17). As such, we computed all normal modes b with frequencies in the range $f < \omega_b/\omega_a < 1-f$; we took $f = 1/10$, which yielded 344,479 potential pairs, but trying $f = 1/5$, which yielded 61,623, did not change the result.

3. We computed T_{abc}, not including the three-mode-coupling coefficient κ_{abc} (since it is computationally expensive to evaluate), for all possible pairs of modes satisfying (i) and (ii) as well as the selection rules in equations (2.39) – (2.41).

4. From the results of (iii), we selected the $N = 5000$ smallest threshold energies, and then recomputed T_{abc} for these pairs this time including κ_{abc} (Weinberg et al. 2012). (Trying $N = 1000$ did not change the results.) We set $m_b = m_c = 0 = m_a$ for simplicity, since κ_{abc} depends only weakly on the values of m so long as equation (2.40) is satisfied. Sorting again then yielded the best-coupled daughter pairs and an approximation for the saturation amplitude S_a.

Table 2.5 shows the best-coupled daughter mode pairs resulting from this procedure. It is interesting to note that most daughter pairs a) involve an $l = 1$ mode coupled to an $l = 3$ mode (P2, P4, P5, P6), and/or b) have a large quality-factor ratio (all except P2, P5, & P9 have $|\frac{1}{2}\log_{10}(q_b/q_c)| > 0.5$).

For daughter pairs satisfying (a), the $l = 3$ mode would be much harder to observe in a lightcurve since disk averaging involves strong cancellation for larger-l modes—indeed, Table 2.3 shows $b_3/b_1 \sim 0.1$ for Eddington limb darkening, where b_l is a disk-integral factor defined in equation (2.23). (The other disk-integral factor, c_l, does not decline as sharply with increasing l, but corresponds to cross-section perturbations, which are small relative to emitted flux perturbations as discussed below.) For daughter pairs satisfying (b), since the ratio of daughter amplitudes scales as the square root of the ratio of their quality factors, one of the modes would again be difficult to observe.

Furthermore, if the parent had $m_a = \pm 2$ instead of $m_a = 0$ (see § 2.6.6), each daughter pair would have several options for m_b and m_c, introducing the possibility of $|m_b| \neq |m_c|$. This would mean daughters would experience even greater disparity in disk-integral cancellation due to the presence of $Y_{lm}(\theta_\mathrm{o}, \phi_\mathrm{o})$ in equation (2.22); e.g., $|Y_{10}(\theta_o, \phi_o)/Y_{32}(\theta_o, \phi_o)| \sim 0.02$ for KOI-54.

The above results provide a reasonable explanation for why there is only one instance of two nonharmonic pulsations adding up to an observed harmonic in the data for KOI-54—only P9 from Table 2.5 has the potential to mimic pulsations F5 and F6 from W11. Nonetheless, the nonlinear interpretation of the nonharmonic pulsations in KOI-54 predicts that every nonharmonic pulsation should be paired with a lower-amplitude sister such that their two frequencies sum to an exact harmonic of the orbital frequency. This prediction may be testable given a sufficient signal-to-noise ratio, which may be possible with further observations of KOI-54.

Lastly, we can attempt to translate our estimate of the parent threshold amplitude S_a into an observed flux perturbation, $\delta J_\mathrm{sat}/J$, using the techniques of § 2.3.3. Since our nonlinear saturation calculation was performed with adiabatic normal modes, we strictly can only calculate the observed flux variation due to cross-section perturbations, δJ_cs (the ξ_r component of equation 2.22), and not that due to emitted flux perturbations, δJ_ef (the ΔF component of equation 2.22). It evaluates to

$$\begin{aligned}\left|\frac{\delta J_\mathrm{cs}}{J}\right| &= |S_a \times (2b_l - c_l) \times \xi_{r,a}(R) \times Y_{20}(\theta_o, \phi_o)| \\ &\simeq 1.7 \text{ mmag},\end{aligned}$$

However, we can employ our nonadiabatic code to calibrate the ratio of δJ_cs to δJ_ef, which we find to be $\delta J_\mathrm{ef}/\delta J_\mathrm{cs} \simeq 9$ for the 91st harmonic. We can then estimate the total saturated flux perturbation:

$$\left|\frac{\delta J_\mathrm{sat}}{J}\right| = \left(\frac{\delta J_\mathrm{ef}}{\delta J_\mathrm{cs}} + 1\right)\left|\frac{\delta J_\mathrm{cs}}{J}\right| \simeq 17 \text{ mmag}.$$

This result is a factor of ~ 100 too large relative to the observed amplitude of 229 μmag for the 91st harmonic (Table 2.2). Taken at face value, this would mean that the inferred mode amplitude is below threshold, and should not be subject to nonlinear processes, despite evidence to the contrary. There are several possible explanations for this discrepancy. If the 91st harmonic is actually an $m = \pm 2$ mode, which we proposed in § 2.5.1, then the intrinsic amplitude required to produce a given observed flux perturbation is a factor of ~ 200 times larger than for $m = 0$ modes given KOI-54's face-on inclination (§ 2.3.3). This would make the observed flux perturbation of the 91st harmonic comparable to that corresponding to the threshold for three-mode coupling, consistent with the existence of nonharmonic pulsations in the lightcurve. We discuss this further in § 2.6.6.

Alternatively, if the 91st harmonic is in fact an $m = 0$ mode, many daughter modes may coherently contribute to the parametric resonance, reducing the threshold considerably, as in Weinberg et al. (2012). A more detailed calculation, coupling many relevant daughter and potentially granddaughter pairs simultaneously, should be able to address this more quantitatively.

2.6.6 Are harmonics 90 and 91 caused by prograde, resonance-locking, $|m| = 2$ g-modes?

As introduced in § 2.5.1, having two pseudosynchronized stars presents an ostensibly appealing explanation for the large-amplitude 90th and 91st harmonics observed in KOI-54 (henceforth F1 and F2; Table 2.2): each is the manifestation of a different highly resonant eigenmode effecting a resonance lock for its respective star by opposing the equilibrium tide's torque.

We discuss the viability of this interpretation below. First, however, what alternate explanation is available? The most plausible would be that F1 and F2 are completely independent, resonantly excited $m = 0$ modes. Each coincidence would require a detuning of $|\omega_{nl} - \sigma_{km}|/\Omega_{\rm orb} \sim 2 \times 10^{-2}$ (Figure 2.9), which is equivalent to $|\omega_{nl} - \sigma_{km}|/\omega_{nl} \sim 10^{-4}$, where ω_{nl} is the nearest eigenfrequency and $\sigma_{km} = k\Omega_{\rm orb} - m\Omega_*$ is the driving frequency. The probability of having a detuning equal to or smaller than this value, given ~ 10 available modes (Figure 2.9), is $\sim 10\%$, so the combined probability if the resonances are independent is $\sim 1\%$. Moreover, in § 2.6.4 we show that in this $m = 0$ interpretation, F1 and F2 must come from different stars, yet there is no explanation for why the two excited modes are so similar.

If instead F1 and F2 are due to highly resonant $m = \pm 2$ resonance locking modes, several observations are naturally explained. The high degree of resonance is an essential feature of the inevitable pseudosynchronous state reached when the torque due to the dynamical tide cancels that due to the equilibrium tide (§ 2.5.1). The fact that the resonant modes correspond to similar k would be largely a consequence of the fact that the two stars in the KOI-54 system are similar in mass and radius to $\sim 10\%$, so that a similar mode produces the dynamical tide torque in each star (although a corresponding $\sim 10\%$ difference in k would be equally possible in this interpretation).

In addition, we showed in § 2.6.5 that the observed amplitudes of F1 and F2 are a factor of up to ~ 100 smaller than their nonlinear threshold values assuming $m = 0$. There is also strong evidence that at least F2 has its amplitude set by nonlinear saturation. Having $m \neq 0$ would help to resolve this discrepancy because the intrinsic amplitude of $m = \pm 2$ modes would need to be ~ 200 times larger to produce the observed flux perturbation. This would then imply that the amplitudes of F1 and F2 are indeed above the threshold for three-mode coupling, naturally explaining the presence of the nonharmonic pulsations in the KOI-54 lightcurve.

However, several significant problems with the resonance-locking interpretation arise upon closer examination. Assume that F1 and F2 indeed correspond to $m = \pm 2$ g-modes that generate large torques effecting $P_{\rm ps} \sim 1.8$ days pseudosynchronization locks. In order to create positive torques, equation (A.39) shows that we must have $m(k\Omega_{\rm orb} - m\Omega_*) > 0$, which reduces to

$$(k/m)\Omega_{\rm orb} > \Omega_*. \tag{2.43}$$

In order to determine which modes correspond to F1 and F2, we can enforce a close resonance by setting

$$\omega_{nl} \simeq 90\,\Omega_{\rm orb} - 2\,\Omega_*, \tag{2.44}$$

where we have used the fact that equation (2.43) requires k and m to have the same sign for a positive torque. For $l = 2$ and using a MESA stellar model consistent with W11's mean modeled parameters for star 1 (Table 2.1), equation (2.44) yields $n \simeq 30$, neglecting rotational modification of the modes (i.e., not employing the traditional approximation).

However, in our calculations in § 2.5.1 we find that the resonant torque due to the dynamical tide is instead typically caused by g-modes with n of 8 – 15 (basically set by the intersection of the Hansen coefficient and linear overlap curves, as discussed in § 2.4.2 in the context of flux perturbations). Using equation (2.44) again, this would mean we would expect k of 140 – 200. Furthermore, we find that even a perfectly resonant $n = 30$ g-mode makes a negligible contribution to the torque. This is true both for ZAMS models and for evolved models consistent with the observed radii in KOI-54, indicating that there is little uncertainty introduced by the details of the stellar model. This result suggests that the g-modes inferred to correspond to F1 and F2 are inconsistent with what would be expected from our torque calculation if the rotation rate is indeed ~ 1.8 days.

If we account for rotation in the traditional approximation (§ 2.3.4), the n of a prograde mode of a given frequency can be at most a factor of $\sqrt{4/6}$ times smaller than its corresponding nonrotating value; this follows from the fact that the angular eigenvalue λ asymptotes to $m^2 = 4$ in the limit $\omega_{nl} \ll \Omega_*$ for prograde modes, instead of $\lambda = l(l+1) = 6$ in the nonrotating limit. This reduces the n of the 90th harmonic from $n \simeq 30$ to $n \simeq 24$, still insufficient to yield a significant torque.

Another major problem with the resonance lock interpretation is that although our orbital evolution simulations described in § 2.5.1 ubiquitously produce resonance locks, they always occur in only one star at a time. This is because if a mode is in a resonance lock in one star and a mode in the other star tries to simultaneously resonance lock, the first lock typically breaks since the orbital frequency begins to evolve too quickly for the lock to persist. Although it is possible for simultaneous resonance locks in both stars to occur, such a state is very improbable. Similar orbital evolution simulations presented in Fuller & Lai (2011) did produce simultaneous resonance locks, but only because they simulated only one star and simply doubled the energy deposition rate and torque, thus not allowing for the effect just described.

Finally, we point out one last inconsistency in the resonance lock interpretation of F1 and F2. It is straightforward to calculate the predicted flux perturbation associated with perfectly resonant $|m| = 2$ g-modes in resonance locks (using, e.g., the calibration discussed at the end of § 2.6.5): for modes ranging from $n \sim 8$ – 15, we find that the predicted flux perturbation for KOI-54's parameters is $\sim 10 - 30$ μmag. This is a factor of ~ 10 smaller than the observed flux perturbations, yet somewhat larger than the smallest-amplitude pulsation reported by W11. It is also a factor of ~ 2 smaller than the nonlinear coupling threshold for an $m = 2$ mode (which we determined using the same procedure as in § 2.6.5, extended to allow for an $m \neq 0$ parent), although the uncertainties involved in our nonlinear estimates are significant enough that we do not consider this to be a substantial problem.

Thus even if F1 and F2 can be attributed to modes undergoing resonance locks (which is highly nontrivial, as we have seen), the observed amplitudes are larger than those we predict. Conversely, if F1 and F2 are simply chance $m = 0$ resonances, it appears that if a resonance lock existed, it would have been detected, although the possibility exists that the resonant mode's flux perturbation was marginally smaller than those of the 30 reported pulsations due to uncertainties in our calculations. Firmer constraints on the flux perturbations in KOI-54 at $k \sim 140 - 200$ would be very valuable in constraining the existence of such $m = \pm 2$ modes, as would information about the phases of the 90th and 91st harmonics (see § 2.4.2).

2.7 Discussion

We have developed a set of theoretical tools for understanding and modeling photometric observations of eccentric stellar binaries. This work is motivated by the phenomenal photometry of the Kepler satellite and, in particular, by the discovery of the remarkable eccentric binary system KOI-54 (Welsh et al. 2011; henceforth W11). This system consists of two similar A stars exhibiting strong ellipsoidal lightcurve variation near periastron passage due to the system's large ($e = 0.83$) eccentricity. W11 successfully modeled this phenomenon, and also reported the detection of at least 30 distinct sinusoidal pulsations in KOI-54's lightcurve (§ 2.2), ~ 20 at exact harmonics of the orbital frequency and another ~ 10 nonharmonic pulsations. Although our work has focused on modeling KOI-54, our methods and techniques are more general, and are applicable to other similar systems.

We developed a simple model of KOI-54's periastron brightening, including both the irradiation and equilibrium tide components of this effect, which agrees at the $\sim 20\%$ level with the results W11 obtained using a much more detailed simulation (§ 2.6.1). Our model may be useful for analysis of other eccentric stellar binaries, allowing determination of orbital and stellar parameters; its simplicity should enable it to be implemented in an automated search of Kepler data.

In § 2.4 we used the adiabatic normal mode formalism (see § 2.3.2 and, e.g., Christensen-Dalsgaard 2003; Kumar et al. 1995), to establish a qualitative connection between the range of stellar modes excited in a given binary system and the system's orbital properties. For more detailed quantitative modeling of the harmonic pulsation spectrum of a given binary system, we further developed the nonadiabatic, inhomogeneous tidal method from Pfahl et al. (2008) by including the Coriolis force in the traditional approximation (§ 2.6.2; Appendix A.1).

In § 2.6.3 we used this method to show that fast rotation tends to suppress power in the lower harmonics of a face-on binary system's lightcurve (Figure 2.7). This can qualitatively explain why there is a scarcity of large-amplitude, lower-harmonic pulsations in KOI-54's lightcurve, relative to predictions for nonrotating stars (Figure 2.3). We also showed in § 2.6.3, however, that the dynamical tidal response may be much larger than ellipsoidal variation in edge-on binaries, unlike in KOI-54 (which has an inclination of $i = 5.5°$; see Table 2.1). For such systems, simultaneous modeling of the dynamical and equilibrium tides may be required in order to constrain system properties.

Moreover, in § 2.5 we showed that rapid rotation periods of ~ 1.8 days are expected for the A stars in KOI-54, due to pseudosynchronization with the orbital motion near periastron. This pseudosynchronous rotation period is shorter than the value of 2.53 days assumed by W11. The latter value is appropriate if the only appreciable torque is that produced by the equilibrium tide (Appendix A.3.2). Since resonantly excited stellar g-modes can produce a torque comparable to that of the equilibrium tide, pseudosynchronous rotation can occur at even shorter rotation periods (Figure 2.4). This involves a stochastic equilibrium between prograde resonance locks and the equilibrium tide. These same rapid rotation periods (~ 1.8 days) yield predicted lightcurve power spectra that are the most qualitatively consistent with the pulsation data for KOI-54 (Figure 2.7).

In § 2.6.4 we performed a preliminary optimization of our nonadiabatic model by comparing its results in detail to the Fourier decomposition of KOI-54's lightcurve (Table 2.2). We searched over an extensive grid of stellar masses and radii, assuming a metallicity of twice solar and a rotation period of 1.5 days. We also set $m = 0$, since KOI-54's nearly face-on orientation implies that this is the case for almost all of the pulsations we modeled (§ 2.3.3). The modeling challenge in tidal asteroseismology contrasts with that of standard asteroseismology in that a) we must simultaneously model both stars, and b) pulsation amplitudes and phases contain the key information in our case, since we are considering a forced system, whereas pulsation frequencies constitute the data in traditional asteroseismology. Moreover, stellar rotation is sufficiently rapid in eccentric binaries that its effect on stellar g-modes cannot be treated perturbatively.

Although our minimization procedure was quite simple, we were able to obtain stellar models with power spectra semi-quantitatively consistent with the observations of KOI-54 (Figure 2.8 & Figure 2.9). The resulting model in Figure 2.8 is not formally a good fit, but this is not surprising given that two of the key parameters (metallicity and rotation period) were not varied in our analysis. Moreover, in our preliminary optimization we found that there were many local minima that produced comparably good lightcurves.

As noted above, *a priori* calculations suggest that both stars in the KOI-54 system should have achieved a pseudosynchronous state at rotation periods of ~ 1.8 days. This requires frequent resonance locks to occur, when a single $|m| = 2$ eigenmode comes into a near-perfect prograde resonance. A natural question is whether such a highly resonant mode could contribute to the KOI-54 lightcurve; this possibility is particularly attractive for the two largest-amplitude harmonics observed, the 90th and 91st. (See also our calculation of nonlinear saturation from § 2.6.5, discussed below.)

However, we find quantitative problems with this interpretation (§ 2.6.6). First, our orbital evolution simulations (§ 2.5.1) indicate that only one resonance lock should exist at a time, meaning that only one of the two large-amplitude harmonics could be explained in this way. This result is in disagreement with the simulations performed by Fuller & Lai (2011), since they did not simultaneously model both stars.

Further, in our calculations, the g-modes capable of producing torques large enough to effect resonance locks have n typically in the range of 8 – 15 (where n is the number of radial nodes), while the 90th harmonic corresponds to n of 25 – 40 for $m = \pm 2$ and rotation periods of 2.0 – 1.5 days. Also, we predict that g-modes producing resonance locks should have k of 140 – 200, much larger than ~ 90, and flux perturbations of 10 – 30 μmag. The latter values are a factor of ~ 10 less than that observed for the 90th and 91st harmonics, but slightly larger than the smallest observed pulsations.

It thus seems quantitatively difficult to interpret harmonics 90 and 91 in KOI-54 as manifestations of $m = \pm 2$ modes in resonance locks, although we cannot conclusively rule out this possibility. Instead, it seems likely that they are simply chance $m = 0$ resonances (as is almost certainly the case for the overwhelming majority of the other observed pulsations in KOI-54). One theoretical uncertainty resides in our omission of rotational modification of the stellar eigenmodes when computing tidal torques. Our estimates suggest that this is a modest effect and is unlikely to qualitatively change our conclusions, but more detailed calculations are clearly warranted.

We note that in future work, pulsation phases should be modeled in addition to the amplitudes reported by W11, since this effectively doubles the information content of the data. Indeed, we showed in § 2.4.2 that a resonant pulsation's phase is strongly influenced by the mode's value of m. In particular, since harmonics 90 and 91 are likely standing waves, as can be seen in the propagation diagram in Figure 2.1, measurement of their phases could help to resolve the uncertainties pointed out above by supplying direct information about their degrees of resonance, thus potentially confirming or disproving the $m = \pm 2$ resonance lock interpretation.

In § 2.6.5 we pointed out evidence for nonlinear mode coupling in KOI-54's observed pulsations: the existence of nonharmonic pulsations (which does not accord with linear theory; § 2.4.2) and the fact that two of them have frequencies that sum to exactly the frequency of the 91st harmonic, the second-largest-amplitude harmonic pulsation in KOI-54's lightcurve. This is consistent with parametric resonance, the leading-order nonlinear correction to linear stellar oscillation theory (Weinberg et al. 2012).

Motivated by this observation, we performed a nonlinear stability calculation that qualitatively explains why no other similar instance of a nonharmonic pair summing to an observed harmonic is present in the data: for the majority of daughter pairs likely to be nonlinearly excited, there are sufficient differences in the l and m values of the daughter pair members, or sufficient differences in their predicted saturated energies, that only one member of the pair would be observable given current sensitivity. Nonetheless, the nonlinear interpretation makes the strong prediction that every nonharmonic pulsation should be paired with a lower-amplitude sister such that their two frequencies sum to an exact harmonic. This prediction may well be testable given a better signal-to-noise ratio.

One additional feature of the nonlinear interpretation is that if the nonlinearly unstable parent is an $m = 0$ mode, then the threshold amplitude for a linearly excited mode to be unstable to parametric resonance, which we have just argued exists in KOI-54, implies flux perturbations that are a factor of ~ 100 larger than those observed. In contrast, the parent being an $m = \pm 2$ mode ameliorates this discrepancy because the parent's intrinsic amplitude must be ~ 200 times larger for a given flux perturbation due to KOI-54's face-on orientation. This result thus argues in favor of the 91st harmonic in KOI-54 being an $m = \pm 2$ mode caught in a resonance lock, as discussed above.

There are many prospects for further development of the analysis begun in this paper. For example, in traditional asteroseismology, standard methods have been developed allowing a set of observed frequencies to be inverted uniquely, yielding direct constraints on stellar parameters, including the internal sound speed profile (Unno et al. 1989). The essential modeling difficulty in tidal asteroseismology is our inability to assign each observed pulsation amplitude to either star of a given binary *a priori*, hindering our attempts to develop a direct inversion technique. We leave the existence of such a technique as an open question.

Future observations of eccentric binaries may avoid this difficulty if one star is substantially more luminous than the other. However, for eccentric binaries with similar stars, in the absence of a means of direct inversion, we are left with a large parameter space over which to optimize, consisting at minimum of eight quantities: both stars' masses, radii/ages, metallicities, and rotation periods. Even this parameter set may ultimately prove insufficient, if modeling of tidally forced pulsations is found to be sensitive to the details of e.g. chemical mixing or convective overshoot, which can modify the Brunt-Väisälä frequency and thus g-mode frequencies.

One possible approach that should be explored in future work is to apply standard numerical optimization algorithms such as simulated annealing to this parameter space, attempting to minimize the χ^2 of our nonadiabatic code's theoretical Fourier spectrum against the observed harmonic pulsation data. In practice, it may be preferable to develop interpolation techniques over a grid of models given the high resolution in stellar parameters needed to resolve the close resonances responsible for large-amplitude pulsations.

Although KOI-54's stars lie near the instability strip, this fact is unimportant for the tidal asteroseismology theory presented in this work. Consequently, future high-precision photometric observations of other eccentric binaries may supply a window into the structure of stars previously inaccessible by the techniques of asteroseismology. Constructing a data pipeline capable of reliably flagging eccentric binary candidates—e.g., finding efficient ways of searching for the equilibrium tide/irradiation lightcurve morphologies shown in Figure 2.5 (Appendix A.2)—is also an important, complementary prospect for future work.

Chapter 3

Linear tides in inspiraling white dwarf binaries: resonance locks

3.1 Introduction

In this work, we consider the effect of tides in detached white dwarf (WD) binaries inspiraling due to energy and angular momentum loss by gravitational waves. Our analysis is motivated by several important questions. For example, to what degree should short-period WD binaries exhibit synchronized rotational and orbital motion? Should WDs in close binaries be systematically hotter than their isolated counterparts, as a result of tidal dissipation? What is the thermal state of WDs prior to the onset of mass transfer?

Several past studies have applied linear perturbation theory to the problem considered in this work. Campbell (1984) and Iben et al. (1998) applied the theory of the equilibrium tide to WD binaries, using parameterized viscosities to estimate the tidal torque. Willems et al. (2010) considered turbulent convective damping acting on the equilibrium tide, as originally considered by Zahn (1977) for late-type stars, and showed that this effect is not able to synchronize a WD binary within its gravitational wave inspiral time.

Rathore et al. (2005) and Fuller & Lai (2011) moved beyond the large-scale, nonresonant equilibrium tide, and considered the tidal excitation of standing g-modes during inspiral, analyzing the behavior of wave amplitudes as a system sweeps through resonances. However, neither study allowed the WD's spin rate to evolve, an assumption that eliminated the physics highlighted in this work.

In this paper we also focus on tidally excited g-modes in WD binaries; one of our goals is to assess whether the resonantly excited "dynamical tide" represents a traveling or standing wave. This amounts to whether a tidally generated wave is able to reflect at its inner and outer radial turning points. If reflection cannot occur, then a damping time of order the group travel time across the mode propagation cavity results; if reflection does occur, then the wave amplitude can build up significantly during close resonances between g-mode frequencies and the tidal forcing frequency.

This question has been addressed before in the context of main-sequence stars. Zahn (1975) employed a traveling wave description of the dynamical tide in the context of early-type stars with radiative envelopes, assuming waves would be absorbed near the surface by rapid radiative diffusion. Goldreich & Nicholson (1989a) enhanced this argument, showing that dynamical tides first cause tidal synchronization in such a star's outer regions, leading to the development of critical layers and even stronger radiative damping. However, they did not assess whether angular momentum redistribution could enforce solid-body rotation and thereby eliminate critical layers; we address this important point in § 3.6.2. In the absence of critical layers, Witte & Savonije (1999) introduced the phenomenon of resonance locks (§ 3.4), which rely on the large wave amplitudes produced during eigenmode resonances. We will show that similar resonance locks occur ubiquitously in close WD binaries.

Goodman & Dickson (1998) considered the case of late-type stars with convective envelopes, and showed that tidally generated waves excited at the edge of the convection zone steepen and break near the cores of such stars. Fuller & Lai (2012a), in their study of the tidal evolution of WD binaries, found that the dynamical tide in a carbon/oxygen WD instead breaks near the outer turning point. As such, they invoked an outgoing-wave boundary condition in their analysis. We find that their assumption may not be generally applicable due to an overestimate of the degree of wave breaking; see § 3.6.1. As a result the dynamical tide may represent a standing wave for a substantial portion of a WD binary's inspiral epoch.

This paper is organized as follows. In § 3.2 we provide pertinent background information on WDs and tidal effects that our subsequent results rely on. In § 3.3 we give a broad overview of the results we derive in more detail in §§ 3.4 – 3.8. In § 3.4 we consider the case of resonance locks created by standing waves. We analyze the resulting tidal efficiency and energetics in § 3.5. In § 3.6 we analyze whether standing waves are able to occur, considering wave breaking in § 3.6.1 and critical layers in § 3.6.2. In § 3.7 we turn our attention to traveling waves, discussing wave excitation and interference in § 3.7.1 and showing that traveling waves can also create resonance locks in § 3.7.2. In § 3.8 we then employ numerical simulations to combine our standing and traveling wave results. In § 3.9 we compare our results to observational constraints and discuss physical effects that need to be considered in future work. We then conclude in § 3.10 with a summary of our salient results.

3.2 Background

A short-period compact object binary efficiently emits gravitational waves that carry off energy and angular momentum. This process causes its orbit to circularize; as such, we will restrict our attention to circular WD binaries in this work (however, see Thompson 2011). Gravitational waves also cause such a binary's orbit to decay according to $\dot{\Omega} = \Omega/t_{\rm gw}$, where the characteristic gravitational wave inspiral timescale for a circular orbit is (Peters 1964)

$$t_{\rm gw} = \omega_{\rm dyn}^{-1} \frac{5}{96} \frac{\left(1+M'/M\right)^{1/3}}{M'/M} \beta_*^{-5} \left(\frac{\omega_{\rm dyn}}{\Omega}\right)^{8/3}. \tag{3.1}$$

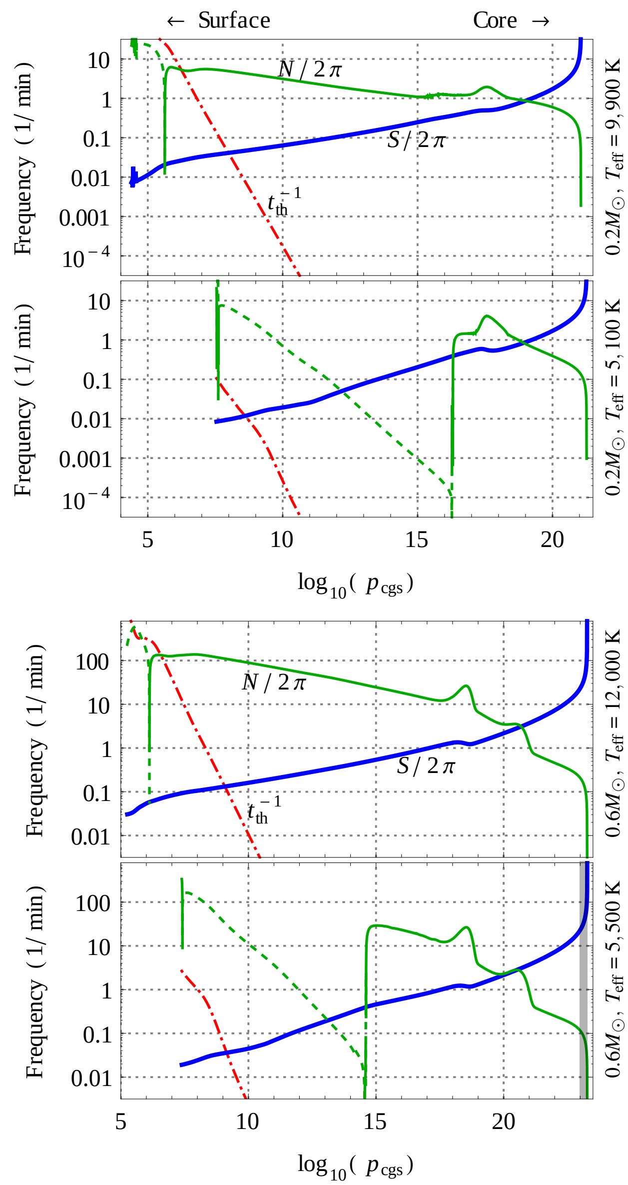

Figure 3.1: Propagation diagrams for several of our WD models listed in Table 3.1. The top two panels are our $0.2M_\odot$ `He10` and `He5` helium WDs, with $T_{\rm eff} = 9{,}900$ and 5,100 K respectively; the bottom two panels are our $0.6M_\odot$ `CO12` and `CO6` carbon/oxygen WDs, with $T_{\rm eff}$ = 12,000 and 5,500 K respectively. Each plot shows the Brunt-Väisälä frequency N (green line; dashed indicates $N^2 < 0$), the quadrupolar Lamb frequency S (thick blue line), and inverse local thermal time $1/t_{\rm th} = gF/pc_pT$ (red dot-dashed line). A g-mode is able to propagate where its frequency is less than both N and S. In the bottom panel showing our `CO6` model, the shaded region at high pressure indicates the plasma interaction parameter $\Gamma > 220$, implying crystallization occurs (which is not included in our model); see § 3.9.3.

Table 3.1: WD models. Masses of the helium models (top three) are $0.2M_\odot$; masses of the carbon/oxygen models (bottom two) are $0.6M_\odot$. Helium models each have a hydrogen layer of mass $0.0033M$, and were generated with MESA (Paxton et al. 2011); carbon/oxygen models each have a helium layer of mass $0.017M$ and a hydrogen layer of mass $0.0017M$. Further details on white dwarf models are given in Appendix B.4; Figure 3.1 provides propagation diagrams for several models. The dynamical time is $t_*^2 = R^3/GM$; the thermal time at the radiative-convective boundary (RCB) is $t_{\rm th}|_{\rm rcb} = pc_pT/gF|_{\rm rcb}$, where we take $2\pi/N =$ 100 min to define the RCB; the WD cooling time is $t_{\rm cool} = E_{\rm th}/L$, where $E_{\rm th} = \int c_pT\,dM$ approximates the total thermal energy; $M_{\rm conv}$ is the mass in the outer convection zone, which increases in size by many orders of magnitude as a WD cools (see Figure 3.1); the plasma interaction parameter at the center of the WD is $\Gamma_{\rm core} = Z^2e^2/kTd_{\rm i}|_{r=0}$, where Ze is the mean ion charge, $d_{\rm i}$ is the ion spacing, and the value of Γ corresponding to the onset of crystallization is discussed in § 3.9.3; the relativity parameter is $\beta_*^2 = GM/Rc^2$; and I_* is the WD moment of inertia.

ID	$T_{\rm eff}$ (K)	$L/L_\odot$	$R/R_\odot$	t_* (sec)	$t_{\rm th}\|_{\rm rcb}$ (yr)	$t_{\rm cool}$ (Gyr)	$M_{\rm conv}/M$	$\Gamma_{\rm core}$	$\beta_*/10^{-2}$	I_*/MR^2
He10	9,900	1.3×10^{-2}	0.038	26.	7.7×10^{-8}	0.36	3×10^{-14}	1.2	0.34	0.085
He7	7,000	1.9×10^{-3}	0.029	18.	5.1×10^{1}	0.98	1×10^{-7}	2.7	0.38	0.11
He5	5,100	3.9×10^{-4}	0.025	14.	1.3×10^{6}	2.5	2×10^{-4}	5.1	0.41	0.14
CO12	12,000	3.0×10^{-3}	0.013	3.1	6.5×10^{-9}	0.59	1×10^{-16}	71.	0.99	0.16
CO6	5,500	1.3×10^{-4}	0.013	2.9	7.3×10^{2}	4.5	3×10^{-8}	260.	1.0	0.18

Here $\omega_{\rm dyn}^2 = GM/R^3$ is the dynamical frequency of the primary, M' is the mass of the companion, $\beta_*^2 = GM/Rc^2$ is the relativity parameter of the primary, and Ω is the orbital frequency. The time a binary will take until it begins to transfer mass is given by $t_{\rm merge} = 3t_{\rm gw}/8$. For a $0.6M_\odot$ WD with an equal-mass companion, orbital periods of less than ~ 530 min imply the binary will begin mass transfer within 10 Gyr; this restriction reduces to $P_{\rm orb} \lesssim 270$ min for a $0.2M_\odot$ WD with an equal-mass companion.

During the process of inspiral, the tidal force acting on each element of the binary steadily grows. The tidal response on a star is typically divided conceptually into two components: the equilibrium tide and the dynamical tide. The equilibrium tide represents the large-scale distortion of a star by a companion's tidal force (Zahn 1977); it is often theoretically modeled as the filling of an equipotential surface, but can also be treated as the collective nonresonant response of all of a star's eigenmodes. The two viewpoints are equivalent, as in both the tidal forcing frequency is set to zero. Except near very strong resonances, the equilibrium tide contains the great majority of the tidal energy. Nonetheless, whether it produces a strong torque is also influenced by the degree to which it lags behind the tidal potential, which is determined by how strongly the equilibrium tide is damped. For WDs, Willems et al. (2010) showed that turbulent convection acting on the equilibrium tide does not cause significant synchronization (Appendix B.2.2).

The dynamical tide, on the other hand, corresponds to the tidal excitation of internal stellar waves (Zahn 1975). In particular, given that tidal forcing periods are much longer than the stellar dynamical timescale, buoyancy-supported gravity waves or g-modes are predominantly excited (although rotationally supported modes become important when the rotation and tidal forcing frequencies become comparable; see § 3.9.2). Propagation of gravity waves is primarily determined by the Brunt-Väisälä frequency N, given by

$$N^2 = \frac{1}{g}\left(\frac{1}{\Gamma_1}\frac{d\ln p}{dr} - \frac{d\ln\rho}{dr}\right), \tag{3.2}$$

where Γ_1 is the adiabatic index. A g-mode is able to propagate where its frequency lies below both N as well as the Lamb frequency $S_l^2 = l(l+1)c_s^2/r^2$. Plots of both N and S_l for several helium and carbon/oxygen WD models are provided in Figure 3.1.

Degeneracy pressure satisfies $p \propto \rho^{\Gamma_1}$; substituting this into equation (3.2) yields $N = 0$. Thus the Brunt-Väisälä frequency becomes very small in the WD core where degeneracy pressure dominates gas pressure, scaling as $N^2 \propto kT/E_F$, where E_F is the Fermi energy. Moreover, WDs also often possess outer convection zones with $N^2 < 0$. As a result, a typical tidally excited g-mode in a WD possesses both an inner turning point near the core as well as an outer turning point near the radiative-convective boundary.

Lastly, temporarily ignoring degeneracy pressure and assuming an ideal gas equation of state, equation (3.2) can be expressed as (Hansen et al. 2004)

$$N^2 = \frac{\nabla_{\rm ad}\rho^2 g^2 c_p T}{p^2}(\nabla_{\rm ad} - \nabla) - g\frac{d\ln\mu}{dr}, \tag{3.3}$$

where μ is the mean molecular weight. From this expression we can see that the Brunt-Väisälä frequency becomes larger in composition gradient zones, where μ decreases with radius. This can be seen in Figure 3.1, where a "bump" in N occurs in helium models due to the helium to hydrogen transition; two bumps are present in carbon/oxygen models, resulting from carbon/oxygen $\rightarrow$ helium and helium $\rightarrow$ hydrogen.

3.3 Dynamical tide regimes in white dwarfs

Here we will give a general overview of the results covered in §§ 3.4 – 3.8 by enumerating four essential regimes of the dynamical tide in WDs, which comprises the wavelike tidal response. The two basic distinctions made by our four regimes are a) whether tidally excited gravity waves can reflect and become large-amplitude standing modes, or whether they instead represent traveling waves; and b) whether or not a resonance lock can be created. Resonance locks are described in detail in §§ 3.4 & 3.7.2; they occur when the tidal torque causes the tidal forcing frequency $\sigma = 2(\Omega - \Omega_{\rm spin})$ to remain constant even as the orbit shrinks.

First, the two regimes where standing waves exclusively occur are:

S1) In this regime the dynamical tide represents a purely standing wave, but with a resulting torque that is insufficient to effect a resonance lock even during a perfect resonance. This occurs for long orbital periods or small companion masses. As such, the system quickly sweeps through resonances, and the time-averaged torque is dominated by its value away from resonances. This nonresonant torque is proportional to the eigenmode damping rate, and is thus very small for WDs, due to their long thermal times. As a consequence the average tidal quality factor is very large, tidal heating is negligible, and the spin rate remains essentially constant.

S2) Here the dynamical tide is again a standing wave, but with eigenmode amplitudes large enough to create resonance locks. This regime is addressed in detail in § 3.4; we estimate the orbital period corresponding to its onset in equation (3.10). During a resonance lock, tides become efficient: due to strong tidal torques, the spin frequency changes at the same rate as the orbit decays due to gravitation wave emission. Definite predictions result for the tidal energy deposition rate (equation 3.20) and tidal quality factor (equation 3.17).

Next, the regimes strongly influenced by traveling waves are:

T1) In this regime, the off-resonance dynamical tide is still a standing wave, but near resonances the wave amplitude becomes so large that reflection near the surface cannot occur due to wave breaking (§ 3.6.1). Furthermore, the traveling wave torque is too weak to cause a resonance lock. Since the typical torque experienced by the WD is once again the off-resonance standing wave value, the synchronization and tidal heating scenario is very similar to regime (S1)—in other words, tides are ineffective.

T2) Just as with regime (T1), the standing wave torque is capped at resonances, becoming a traveling wave; however in this regime the traveling wave torque itself is strong enough to create a resonance lock (terminology discussed further in footnote 5), as addressed in § 3.7. We estimate the onset of this regime in equation (3.33). The predictions for the tidal energy deposition rate and quality factor are the same as in (S2).

Although we consider only these four regimes in this work, at shorter orbital periods and nearly synchronous rotation, physical effects such as Coriolis modification of stellar eigenmodes and nonlinear tidal excitation mechanisms are likely to become very important; see § 3.9.2.

The archetypal scenario is as follows. A WD binary with a sufficiently long orbital period begins in regime (S1). Eventually, as the orbit shrinks due to gravitational radiation and the tidal force correspondingly increases in magnitude, the dynamical tide becomes strong enough that a resonance lock takes effect and regime (S2) is reached. However, as inspiral accelerates, the torque necessary to maintain the resonance lock becomes larger, requiring larger wave amplitudes. When the amplitude becomes too great, the wave begins to break near the outer turning point, and the system enters regime (T1). Finally, when the traveling wave torque becomes large enough to create a resonance lock, it enters regime (T2). In § 3.8, we verify this picture numerically.

3.4 Resonance locks by standing waves

We assume in this section that the dynamical tide is a superposition of standing waves and proceed to predict the tidal evolution of a WD binary. We discuss the applicability of the standing wave limit in § 3.6.

Assuming a circular orbit and alignment of spin and orbital angular momenta, the secular tidal torque on a star can be expressed as a sum over quadrupolar ($l = 2$) eigenmodes indexed by their number of radial nodes n (Appendix B.2.2):

$$\tau = 8mE_*\varepsilon^2 W^2 \sum_n Q_n^2 \left[\frac{\omega_n^2 \sigma \gamma_n}{(\omega_n^2 - \sigma^2)^2 + 4\sigma^2\gamma_n^2} \right]. \tag{3.4}$$

Here $\sigma = m(\Omega - \Omega_{\rm spin})$ is the tidal driving frequency in the corotating frame, Ω is the orbital frequency, $\Omega_{\rm spin}$ is the solid-body rotation rate, $m = 2$, $E_* = GM^2/R$ is the WD energy scale, $\varepsilon = (M'/M)(R/a)^3$ is the tidal factor, M' is the companion mass, a is the orbital separation, $W^2 = 3\pi/10$, and γ_n is an eigenmode damping rate (Appendix B.2.3). Our eigenfunction normalization convention is given in equation (B.17); physical quantities such as the torque are of course independent of the choice of normalization.

The linear overlap integral Q_n appearing in equation (3.4) represents the spatial coupling strength of an eigenmode to the tidal potential, and is normalization dependent. Since the tidal potential spatially varies only gradually, Q_n is large for low-order modes, and becomes much smaller for high-order, short-wavelength modes. We describe various methods of computing Q_n in Appendix B.2.4.

The factor in brackets in equation (3.4) describes the temporal coupling of an eigenmode to the tidal potential, and becomes very large during resonances, when the tidal driving frequency becomes close to a stellar eigenfrequency. The nonresonant limit of this factor, which corresponds to the equilibrium tide, increases with stronger damping. Paradoxically, however, the torque during a resonance is inversely proportional to the damping rate, since damping limits the maximum energy a resonant mode attains.

We note that by invoking steady-state solutions to the mode amplitude equations, as we have done here, we fail to account for the energy and angular momentum transfer required to bring a mode's amplitude up to the steady-state value. Additionally, the steady-state solution itself may fail to model the behavior of mode amplitudes very close to resonances correctly; we address this in § 3.6.3. Correctly accounting for these two considerations would involve simultaneously solving both the mode amplitude equations for all relevant modes as well as the orbital evolution equations, a task we leave to future study.

Continuing, we focus on resonant tidal effects, and consider the case of a particular eigenmode with a frequency close to the tidal driving frequency, i.e. $\omega_n \approx \sigma$. We can then make this substitution everywhere in equation (3.4) other than in the detuning frequency $\delta\omega_n = \omega_n - \sigma$ to find

$$\tau \approx 2mE_*\varepsilon^2 W^2 Q_n^2 \left(\frac{\omega_n \gamma_n}{\delta\omega_n^2 + \gamma_n^2} \right), \tag{3.5}$$

having dropped nonresonant terms. One might expect that since the strongest torques are achieved very near resonance, where $\delta\omega_n \sim 0$, a system should evolve quickly through resonances, and they should have little effect on the long-term orbital and spin evolution. This is often accounted for by using a "harmonic mean" of the torque to produce a synchronization time, i.e., $t_{\rm sync} = \int I_* d\Omega/\tau$, where I_* is the moment of inertia (Goodman & Dickson 1998).

Under particular circumstances, however, it is possible to achieve a resonance lock, where an eigenmode remains in a highly resonant state for an extended period of time, as originally proposed by Witte & Savonije (1999). Very near a resonance, the torque depends very strongly on the detuning frequency $\delta\omega_n$, and very weakly on the orbital period by itself; as a result, the essential criterion that must be satisfied for a resonance lock to occur is that the detuning frequency must remain constant:

$$0 = \dot{\delta\omega_n} = m\left((1-C_n)\dot{\Omega}_{\rm spin} - \dot{\Omega}\right), \tag{3.6}$$

where $\partial\omega_n/\partial\Omega_{\rm spin} = -mC_n$ accounts for rotational modification of the stellar eigenmodes, $C_n \approx 1/6$ for high-order $l = 2$ g-modes and slow rotation (Unno et al. 1989), and we have assumed the WD rotates as a solid body. (We justify the solid-body rotation assumption in § 3.6.2.)

For simplicity, we will henceforth ignore rotational modification of the stellar eigenfrequencies, so that $C_n \to 0$. This limits the quantitative applicability of our results to where $\Omega - \Omega_{\rm spin} \gtrsim \Omega_{\rm spin}$. We also neglect progressive WD cooling, which decreases the Brunt-Väisälä frequency and consequently lowers eigenmode frequencies; this is valid so long as the cooling time $t_{\rm cool}$, which is on the order of $\sim$ Gyr for the models listed in Table 3.1, is much longer than the gravitational wave decay time $t_{\rm gw}$ (equation 3.1). Subject to these simplifications, equation (3.6) then reduces to $\dot{\Omega} = \dot{\Omega}_{\rm spin}$, i.e., that the orbital and spin frequencies evolve at the same rate. Since the orbital frequency increases due to the emission of gravitational waves, and the spin frequency increases due to tidal synchronization, this phenomenon is plausible at first glance. We now work out the mathematical details.

The evolution of $\Omega_{\rm spin}$ and Ω proceed as

$$\begin{pmatrix} \dot{\Omega}_{\rm spin}/\Omega_{\rm spin} \\ \dot{\Omega}/\Omega \end{pmatrix} = \begin{pmatrix} \tau/I_*\Omega_{\rm spin} \\ 1/t_{\rm gw} + (3/2)(\dot{E}_{\rm tide}/|E_{\rm orb}|) \end{pmatrix}, \tag{3.7}$$

where $\dot{E}_{\rm tide}$ is the secular tidal energy transfer rate[1] and the gravitational wave inspiral time $t_{\rm gw}$ is given in equation (3.1). Here we have failed to account for tidal effects in the companion, which would provide an extra contribution to $\dot{E}_{\rm tide}$; see below.

Using equations (3.7) and (B.20), equation (3.6) becomes

$$\frac{\Omega}{t_{\rm gw}} = \tau\left(\frac{1}{I_*} - \frac{3}{2}\frac{1}{\mu a^2}\right), \tag{3.8}$$

where $\mu = MM'/(M+M')$ is the reduced mass. Since $\mu a^2 \gg I_*$, in the present context we can neglect any tidal influence on $\dot{\Omega}$ even in this extreme-resonance scenario; this also now justifies dropping

[1] Our convention is that $\tau > 0$ or $\dot{E}_{\rm tide} > 0$ implies that orbital angular momentum or energy is being transfered to the WD(s).

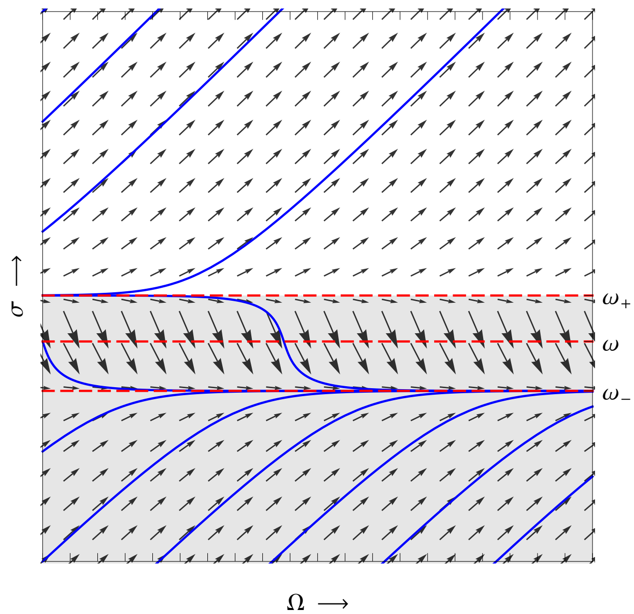

Figure 3.2: Plot schematically illustrating the dynamics of a resonance lock. The abscissa is the orbital frequency Ω, which increases due to gravitational wave radiation, and the ordinate is the Doppler-shifted $l = m = 2$ tidal driving frequency $\sigma = 2(\Omega - \Omega_{\rm spin})$. The arrows depict the vector field describing the orbital evolution equations (equation 3.7). The eigenfrequency of the included mode is ω, which is flanked by stable and unstable fixed points of the evolution equations: ω_- and ω_+, respectively. The dashed red horizontal lines show these three frequencies, while the blue curves are example system trajectories. The stable point ω_- corresponds to a resonance lock, while the unstable fixed point ω_+ corresponds to the upper boundary of the stable fixed point's basin of attraction (shaded region). In producing this plot, the correct functional form of the equation of motion has been used, except with $t_{\rm gw}$ and ε taken as constant, and with artificially chosen values of the various germane parameters. In particular, for realistic resonance lock situations in WDs, the three frequencies shown are very close together, and the basin of attraction barely extends beyond ω_-.

the companion's contribution to $\dot{E}_{\rm tide}$. We can then approximate the resonance lock criterion as

$$\frac{\Omega}{t_{\rm gw}} = \frac{\tau}{I_*}. \tag{3.9}$$

This implies that in a resonance lock, the torque increases as $\tau \propto \Omega^{11/3}$ as the orbit decays.

Once equation (3.9) is satisfied, the lock can persist for a long period of time, since the quantities in equation (3.5) affecting the magnitude of the torque other than $\delta\omega_n$ change only very gradually in time. (We verify this using numerical orbital evolution simulations in § 3.8.) In other words, a resonance lock represents a dynamical attractor; Figure 3.2 provides an illustration of the nonlinear dynamics behind a resonance lock. The lock could eventually be destroyed if the mode responsible began to break near its outer turning point, which would drastically increase the effective damping rate. This phenomenon is explained in § 3.6.

If we assume that the system begins completely unsynchronized, so that $\sigma = 2\Omega$, we can determine the orbital period where a lock first occurs, which we denote $P_{\rm rl}$, by substituting equations (3.5) and (3.1) into (3.9), setting $\omega_n = \sigma$ and hence $\delta\omega_n = 0$, and then solving for the orbital period. To this end, we invoke the following approximate scalings for the eigenmode linear tidal overlap integral Q and damping rate γ:

$$Q \approx Q_0(\sigma/\omega_{\rm dyn})^a \quad \text{and} \quad \gamma \approx \gamma_0(\sigma/\omega_{\rm dyn})^{-b},$$

where values of the various parameters in these expressions are listed in Table 3.3 for our fiducial WD models. Scaling parameter values to those for our `CO6` model, we have

$$P_{\rm rl} \sim 170 \text{ min} \left(\frac{t_*}{2.9 \text{ s}}\right) F_{\rm rl}^p, \tag{3.10}$$

where $t_* = (R^3/GM)^{1/2}$ is the WD's dynamical time, the factor $F_{\rm rl}$ is

$$\begin{aligned} F_{\rm rl} \sim &\left(\frac{M'}{M}\right)\left(\frac{1+M'/M}{2}\right)^{-5/3} \\ &\times \left(\frac{\beta_*}{0.010}\right)^{-5}\left(\frac{I_*}{0.18MR^2}\right)^{-1} \\ &\times \left(\frac{Q_0}{27}\right)^2\left(\frac{\gamma_0}{2.9\times10^{-14}\omega_{\rm dyn}}\right)^{-1} \\ &\times \left(2.15\times10^{26}\right)(0.00327)^{1/p}, \end{aligned} \tag{3.11}$$

the power p is in general

$$p = \frac{1}{4/3+2a+b} \ll 1, \tag{3.12}$$

and $p = 0.094$ for our `CO6` model (Table 3.3). (The last line of equation 3.11 is equal to unity for $p = 0.094$.)

For comparison, direct numerical evaluation of eigenmode properties with our `CO6` WD model yields $P_{\rm rl}$ = 170 min for an equal-mass companion, due to an n = 122 g-mode. This is in very good agreement with the analytic approximation in equation (3.10), and is also consistent with our numerical results in § 3.8. We provide values of $P_{\rm rl}$ for each of our fiducial models in Table 3.2. These results show that resonance locks begin at longer orbital periods for cooler WD models, due to larger outer convective zones and longer overall diffusive damping times (smaller γ_n; see Table 3.3 & Figure B.1). This increases the maximum possible tidal torque, which is proportional to $1/\gamma_n$ (equation 3.5).

Table 3.2: WD tidal parameters. For each of our fiducial WD models from Table 3.1, we list the orbital period $P_{\rm rl}$ of its first resonance lock (§ 3.4, equation 3.10), the orbital period $P_{\rm trl}$ below which traveling wave resonance locks can occur (§ 3.7.2, equation 3.33), its value of λ (§ 3.5, equation 3.14), and the tidal quality factor $Q_{\rm t}|_{100\ {\rm min}}$ for a resonance lock (§ 3.5.1, equation 3.17) evaluated at $P_{\rm orb} = 100$ min. All values are for an equal-mass companion. We determined $P_{\rm rl}$ and $P_{\rm trl}$ by directly searching over numerically computed eigenmode properties.

ID	$P_{\rm rl}$ (min)	$P_{\rm trl}$ (min)	$\lambda/10^{-2}$	$Q_{\rm t}\vert_{100\ {\rm min}}$
`He10`	67	49	1.2	2×10^{9}
`He7`	270	49	2.4	1×10^{9}
`He5`	1,400	90	4.6	1×10^{9}
`CO12`	31	22	6.3	1×10^{7}
`CO6`	170	40	7.4	1×10^{7}

3.5 Energetics

3.5.1 Tidal quality factor

A star's tidal quality factor $Q_{\rm t}$ can be defined as

$$Q_{\rm t} = \frac{\Omega E_{\rm tide}}{\dot{E}_{\rm tide}}, \tag{3.13}$$

where the energy content of the tide $E_{\rm tide}$ is approximately given by (Appendix B.2.2)

$$E_{\rm tide} = \lambda\varepsilon^2 E_*, \tag{3.14}$$

$\lambda = 2W^2\sum_n Q_n^2$, and values of λ for various WD models are given in Table 3.2. Using the relationship between the tidal torque and energy transfer rate from equation (B.20), we see that the tidal torque can be expressed in terms of $Q_{\rm t}$ by

$$\tau = \frac{E_{\rm tide}}{Q_{\rm t}}. \tag{3.15}$$

Since $E_{\rm tide} \sim \lambda F_{\rm tide} h$, where $h \sim \varepsilon R$ is the height of the equilibrium tide and $F_{\rm tide} \sim \varepsilon E_*/R$ is the tidal force, we see that our definition of $Q_{\rm t}$ is consistent with $1/Q_{\rm t}$ representing an effective tidal lag angle; see e.g. Goldreich & Soter (1966). Note that since $Q_{\rm t}$ parameterizes the total tidal energy deposition rate, which includes mechanical energy transfer associated with increasing the WD spin, the value of $Q_{\rm t}$ alone does not fully determine the tidal heating rate; see § 3.5.2.

Using the previous three equations along with the resonance lock condition from equation (3.9), we have that the value of $\mathcal{Q}_{\rm t}$ during a resonance lock is

$$\mathcal{Q}_{\rm t} = \frac{\lambda \varepsilon^2 t_{\rm gw} E_*}{I_* \Omega}. \tag{3.16}$$

Substituting further yields

$$\begin{aligned} \mathcal{Q}_{\rm t} \approx 9.7 \times 10^6 & \left(\frac{P_{\rm orb}}{100 \text{ min}}\right)^{-1/3} \left(\frac{t_*}{2.9 \text{ s}}\right)^{1/3} \\ \times & \left(\frac{M'}{M}\right) \left(\frac{1+M'/M}{2}\right)^{-5/3} \left(\frac{\lambda}{0.074}\right) \\ \times & \left(\frac{I_*}{0.18 M R^2}\right)^{-1} \left(\frac{\beta_*}{0.010}\right)^{-5}. \end{aligned} \tag{3.17}$$

Here I_* is the moment of inertia, $\beta_*^2 = GM/Rc^2$, and all values have been scaled to those appropriate for our `CO6` model (Tables 3.1 & 3.2).

Equation (3.17) is a central result of this paper. It is independent of eigenmode properties and is only weakly dependent on the orbital period, although it depends strongly on the mass, radius, and companion mass. Eigenmode properties do of course dictate when this value of $\mathcal{Q}_{\rm t}$ is applicable, i.e., when resonance locks are able to occur. We will further show in § 3.7.2 that equation (3.17) can hold even when the dynamical tide is a traveling wave, and the standing wave formalism presented thus far is invalid.

Values of the various quantities entering into equation (3.17) are provided for a selection of helium and carbon/oxygen WD models in Table 3.1. In particular, since the inspiral time is much longer for low-mass helium WDs than for more massive carbon/oxygen WDs, equation (3.17) predicts that the tidal quality factor $\mathcal{Q}_{\rm t}$ should be much larger ($\sim 100\times$) for helium WDs, as shown in Table 3.2, meaning tidal effects are more efficient in carbon/oxygen WDs.

3.5.2 Tidal heating

The rate at which heat is dissipated in the WD assuming solid-body rotation can be derived using equation (B.20):

$$\begin{aligned} \dot{E}_{\rm heat} &= \dot{E}_{\rm tide} - \dot{E}_{\rm mech} \\ &= \Omega \tau - \frac{d}{dt}\left(\frac{1}{2} I_* \Omega_{\rm spin}^2\right) \\ &= I_* \dot{\Omega}_{\rm spin} \delta\Omega = \frac{E_{\rm tide}\, \delta\Omega}{\mathcal{Q}_{\rm t}}, \end{aligned} \tag{3.18}$$

where $\delta\Omega = \Omega - \Omega_{\rm spin}$. During a resonance lock we have $\dot{\Omega}_{\rm spin} \approx \dot{\Omega} = \Omega/t_{\rm gw}$, so that

$$\dot{E}_{\rm heat} \approx \frac{I_* \Omega\, \delta\Omega}{t_{\rm gw}}, \tag{3.19}$$

with $\delta\Omega$ then being approximately constant (having neglected rotational modification of WD eigenmodes; see § 3.9.2). Defining the asynchronicity period as $\delta P = 2\pi/\delta\Omega$, we can evaluate this further as

$$\begin{aligned}\dot{E}_{\rm heat} \approx 1.4 \times 10^{-2}\, L_\odot \left(\frac{M'}{M}\right) \left(\frac{1+M'/M}{2}\right)^{-1/3} \\ \times \left(\frac{P_{\rm orb}}{10\ {\rm min}}\right)^{-11/3} \left(\frac{\delta P}{200\ {\rm min}}\right)^{-1} \\ \times \left(\frac{I_*}{0.18MR^2}\right) \left(\frac{M}{0.6M_\odot}\right)^{8/3} \left(\frac{R}{0.013R_\odot}\right)^{2},\end{aligned} \tag{3.20}$$

again scaling variables to our `CO6` model's properties (Table 3.1).

As a simple analytical estimate, consider the example of a resonance lock beginning with the WD unsynchronized at an orbital period P_0 and continuing until the Roche period of $P_{\rm Roche} \sim t_* \ll P_0$. The total orbital energy dissipated in the WD as heat in this example is

$$\begin{aligned}\Delta E_{\rm heat} &= \frac{2\pi I_*}{P_0} \int \frac{\Omega}{t_{\rm gw}} dt \\ &\approx \frac{4\pi^2 I_*}{t_* P_0} \\ &\sim 7.0 E_* \left(\frac{t_*}{P_0}\right) \left(\frac{I_*}{0.18MR^2}\right),\end{aligned} \tag{3.21}$$

which could be very large depending on the value of P_0. If for P_0 we use our estimate from § 3.4 of $P_{\rm rl} \sim 170$ min appropriate for our `CO6` model, we have $\Delta E_{\rm heat} \sim 2 \times 10^{47}$ ergs, a factor of ~ 3 larger than the `CO6` model's thermal energy.

Tidal heating can directly add to a WD's luminosity and minimally affect its thermal structure if a) the thermal time $t_{\rm th} = pc_p T/gF$ at the outer turning point, where wave damping is most efficient, is smaller than $t_{\rm gw}$, and b) $\dot{E}_{\rm heat} \ll L$. The outer turning point occurs due to the outer convection zone, so $t_{\rm th}|_{\rm rcb}$ (radiative-convective boundary) is an appropriate value to use. We find $t_{\rm th}|_{\rm rcb} \lesssim 10^6$ years for all of our WD models, as shown in Table 3.1; this is $\ll t_{\rm gw}$ for $P_{\rm orb} \gtrsim 10$ min, implying that criterion (a) is satisfied. Moreover, for all models other than our $T_{\rm eff} = 5,100$ K helium and $T_{\rm eff} = 5,500$ K carbon/oxygen WDs, $t_{\rm th}|_{\rm rcb} \lesssim 50$ years, and $t_{\rm th}|_{\rm rcb} \lesssim t_{\rm gw}$ is satisfied even directly prior to mass transfer.

Criterion (b) above is more restrictive: examining equation (3.20) shows that near orbital periods of ~ 10 min, the tidal heating rate approaches typical WD luminosities. The orbital period where this occurs depends weakly on the various parameters appearing in equation (3.20), since

$\dot{E}_{\rm heat} \propto P_{\rm orb}^{-11/3}$. Thus the thermal structure of WDs in close binaries may adjust significantly to accommodate the additional heat input for $P_{\rm orb} \lesssim 10$ min. We discuss the consequences of tidal heating further in § 3.9.2.

3.5.3 Tidally enhanced orbital decay

Although the rate $\dot{P}_{\rm orb}$ at which the orbital period of an inspiraling WD binary decays is dominated by the gravitational wave term $\dot{P}_{\rm gw} = -P_{\rm orb}/t_{\rm gw}$, tidal energy dissipation implies a small deviation from this value (see also Piro 2011).[2] We can compute this difference for a system consisting of two WDs both undergoing resonance locks by using equations (3.6), (3.7), and (B.20), which yield

$$\dot{P}_{\rm orb} = \dot{P}_{\rm gw} + \dot{P}_{\rm tide}, \tag{3.22}$$

where

$$\dot{P}_{\rm tide} = \left(\frac{S}{1-S}\right)\dot{P}_{\rm gw}, \quad S \approx 3\left(\frac{I_1+I_2}{\mu a^2}\right), \tag{3.23}$$

$I_{1,2}$ are the moments of inertia of the two WDs, $\mu = M_1 M_2/(M_1+M_2)$ is the reduced mass, a is the semi-major axis, and we have again neglected rotational modification of WD eigenmodes (i.e. $\partial\omega_n/\partial\Omega_{\rm spin} = 0$, where ω_n is a corotating-frame eigenfrequency; see § 3.9.2). This effect may be detectable in future observations of close WD binaries, as discussed in § 3.9.1.

3.6 Applicability of standing waves

3.6.1 Wave breaking

It is important to determine whether the dynamical tide we are attempting to study represents a standing wave or a traveling wave. If it is a standing wave, meaning it is able to reflect at its inner and outer turning points without being absorbed, then it can achieve large amplitudes due to resonances with tidal forcing frequencies (as assumed in § 3.4). In the absence of nonlinear effects that can occur at large amplitudes, a standing wave's damping rate is well approximated by the quasiadiabatic value (Appendix B.2.3), which is small for WDs due to their high densities and long thermal times (see Figure B.1). On the other hand, if the dynamical tide instead behaves as a traveling wave, resulting from absorption prior to reflection, then its damping time is approximately a group travel time.

In this section we determine whether the nonlinear process of gravity wave breaking causes tidally excited g-modes in WDs to be absorbed near the surface and hence to become traveling waves, as has been suggested in recent studies (Fuller & Lai 2011, 2012a). Gravity wave breaking has been considered extensively in the atmospheric science community, since it occurs in Earth's

[2]Note that the purpose of this section is to determine the influence of the tidal energy deposition term $\dot{E}_{\rm tide}$ on the rate of orbital decay, even though this term is neglected everywhere else in this work, as justified in § 3.4.

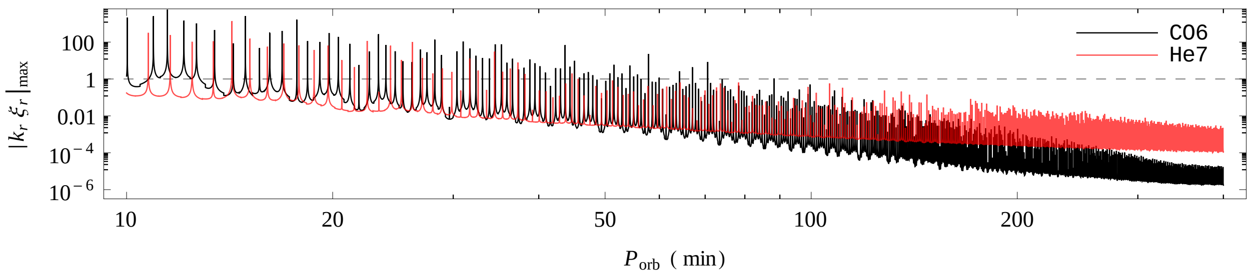

Figure 3.3: The maximum value of $|k_r\xi_r|$ attained throughout the propagation cavity of our `CO6` (black line) and `He7` (red line) WD models (Table 3.1), assuming adiabatic standing waves, $\Omega_{\rm spin} = \Omega/2$, and an equal-mass companion. Where $|k_r\xi_r|_{\max} > 1$, wave breaking occurs (§ 3.6.1), and the effective wave damping time becomes roughly the group travel time across the WD. This occurs very near resonances for $P_{\rm orb} \lesssim 0.5 - 1$ hr.

atmosphere; see e.g. Lindzen (1981). It is also thought to occur in the cores of solar-type stars (Goodman & Dickson 1998; Barker & Ogilvie 2010).

Breaking occurs when a wave's amplitude becomes large enough to disrupt the stable background stratification. One way to derive the condition under which this happens is to determine when a wave would produce its own convective instability, which is equivalent to the perturbed Brunt-Väisälä frequency (squared) becoming comparable to the background value—this then makes the total value negative, implying convection. The Eulerian perturbation to N^2 is given in linear theory by

$$\frac{\delta N^2}{N^2} \approx k_r\xi_r - \frac{\delta p}{p} - \frac{\xi_r}{H_\rho} + \frac{\delta g}{g}, \tag{3.24}$$

where H_ρ is the density scale height and k_r is the wavenumber in the direction of gravity. Since $k_r\xi_r$ is much larger in magnitude than the other terms for g-modes, the wave breaking condition thus becomes

$$|k_r\xi_r| \sim 1. \tag{3.25}$$

Other nonlinear processes also come into play when $|k_r\xi_r| \sim 1$. Indeed, this criterion is equivalent to Ri $\sim 1/4$, where Ri is the Richardson number due to the wave's shear, which implies the wave is Kelvin-Helmholtz unstable. Equation (3.25) is also similar to the condition under which surface ocean waves break: when the vertical displacement becomes comparable to the wavelength.

To determine whether g-modes break, we evaluated the linear, quadrupolar tidal fluid response assuming global adiabatic normal modes and an equal-mass companion; see Appendix B.2. Under these assumptions, we find that for both our helium and carbon/oxygen WD models, the dynamical tide breaks for close resonances at orbital periods as large as ~ 1 hr, as shown in Figure 3.3. The off-resonance dynamical tide begins to break more generically at $P_{\rm orb} \lesssim 10-20$ min.[3] Furthermore, for all of the WD models we have considered (Table 3.1), we find that at sufficiently long orbital periods, the dynamical tide doesn't break even for a perfect resonance, and thus that standing wave resonance locks should be able to occur. As such, we expect wave breaking not to operate during a significant portion of the inspiral epoch, in which case the analysis presented in § 3.4 may be valid. We address this in more detail in § 3.8.

3.6.2 Differential rotation and critical layers

The possibility of differential rotation represents a significant challenge to the standing wave assumption we utilized in § 3.4. Indeed, tidal angular momentum is preferentially deposited in the outer layers of a WD, since that is where damping times are shortest and waves are able to communicate their energy and angular momentum content to the background stellar profile (Goldreich & Nicholson 1989b). Thus tides do not naturally induce solid-body rotation, and instead tend to first synchronize layers near the outer part of the gravity wave propagation cavity (Goldreich & Nicholson 1989a), absent the influence of efficient internal angular momentum transport.

The presence of a synchronized or "critical" layer at the edge of a mode propagation cavity implies that the mode's corotating frequency tends to zero at that location, which in turn means its radial wavenumber becomes very large due to the asymptotic g-mode dispersion relation $\omega \sim N(k_{\rm h}/k_r)$, where $k_{\rm h}$ and k_r are respectively the perpendicular and radial wavenumbers. As a result, the mode's local damping time becomes very short, and it is absorbed rather than reflected, eliminating the possibility of achieving resonant amplitudes (although traveling waves can also effect resonance locks at short orbital periods; § 3.7).

In Appendix B.1 we analyze angular momentum redistribution by fossil magnetic fields, possibly generated by a progenitor star's convective core (during hydrogen or helium fusion) and amplified by flux freezing as the core contracts. We calculate that a field strength of only ~ 200 G is required to maintain solid-body rotation during a resonance lock for an orbital period of ~ 100 min in our `CO6` model, and only ~ 20 G in our `He7` model (Table 3.1). Liebert et al. (2003) conclude that at least $\sim 10\%$ of WDs have fields $\gtrsim 10^6$ G, and speculate that this fraction could be substantially higher; field strengths in WD interiors may be even more significant. With a field of 10^6 G, our calculations indicate that critical layers should not occur until orbital periods of less than 1 min, or even less if the field can wind up significantly without becoming unstable.

3.6.3 Validity of the secular approximation

The Lorentzian mode amplitude solutions invoked in Appendix B.2 to produce the standing wave torque in equation (3.4) are strictly valid only when a mode's amplitude changes slowly

[3]This is in conflict with the claims made in Fuller & Lai (2012a), since that work used $k_r|\boldsymbol{\xi}| \sim 1$ to assess wave breaking, instead of equation (3.25). The total displacement $|\boldsymbol{\xi}| = (\xi_r^2 + \xi_{\rm h}^2)^{1/2}$ includes horizontal motion, which is perpendicular to the stratification and thus does not contribute to breaking. As a g-mode's horizontal motion is much greater than its vertical motion, Fuller & Lai (2012a) overestimated the degree of breaking by a factor of $\sim \xi_{\rm h}/\xi_r \sim \omega_{\rm dyn}/\sigma \gg 1$, where $\sigma = 2(\Omega - \Omega_{\rm spin})$ is the $l = m = 2$ tidal driving frequency.

relative to its damping time. Further examining equation (3.5), we see that near a perfect resonance the amplitude changes by a factor of ~ 2 as the detuning frequency changes by of order the damping rate γ_n. Thus the Lorentzian solution is applicable near a perfect resonance only when

$$\gamma_n^{-1} \lesssim t_{\rm gw} \frac{\gamma_n}{\Omega}, \tag{3.26}$$

which evaluates to

$$P_{\rm orb} \gtrsim 90 \text{ min} \left(\frac{M}{0.6 M_\odot} \right)^{5/11} F_{\rm sec}, \tag{3.27}$$

where

$$F_{\rm sec} = \left(\frac{M'}{M} \right)^{3/11} \left(\frac{1 + M'/M}{2} \right)^{-1/11} \left(\frac{\gamma_n^{-1}}{80 \text{ yr}} \right)^{6/11}.$$

Equation (3.27) is scaled to values for our `CO6` model (Figure 3.6); the restriction instead evaluates to $P_{\rm orb} \gtrsim 50$ min for our `He7` model, using a damping time of $\gamma_n^{-1} \sim 60$ yr appropriate for the initial resonance lock. Below these periods, the Lorentzian solution becomes invalid and the exact outcome is unclear, although our preliminary numerical integrations of fully coupled mode amplitude and orbital evolution equations indicate that resonance locks can still occur even beyond the validity of the Lorentzian solution. (We address a similar concern relating to angular momentum transport in Appendix B.1.2.) Nonetheless, we find that the initial standing wave resonance lock occurs at orbital periods larger than the critical value from equation (3.27) in our `CO6` and `He7` models (Table 3.2), meaning resonance locks should proceed as expected.

3.7 Traveling waves

3.7.1 Excitation and interference

In this section, we will describe two different mechanisms of tidal gravity wave excitation considered in the literature. We will then compare both sets of theoretical predictions to our numerical results to assess which mechanism predominantly operates in our fiducial WD models.

Zahn (1975) showed that when a gravity wave is well described by its WKB solution, a conserved wave energy flux results. Thus gravity waves must be excited where the WKB approximation is invalid: where the background stellar model—particularly the Brunt-Väisälä frequency N—changes rapidly relative to a wavelength.

One natural candidate for wave excitation, then, is at a radiative-convective boundary (RCB), where N^2 abruptly becomes negative. WDs possess convective envelopes near their surfaces (Figure 3.1), so this mechanism is plausible. The resulting theoretical prediction (Zahn 1975; Goodman & Dickson 1998) is that the traveling wave tidal torque should scale as $\tau \propto \sigma^{8/3}$, where $\sigma = 2(\Omega - \Omega_{\rm spin})$ is the $m = 2$ tidal driving frequency. Using our calculation of the traveling wave torque in equation (3.32) from § 3.7.2, we see that this in turn implies that the linear overlap integral (Appendix B.2.4) should scale as $Q_n \propto \omega_n^{11/6}$, given our normalization convention in equation (B.17).

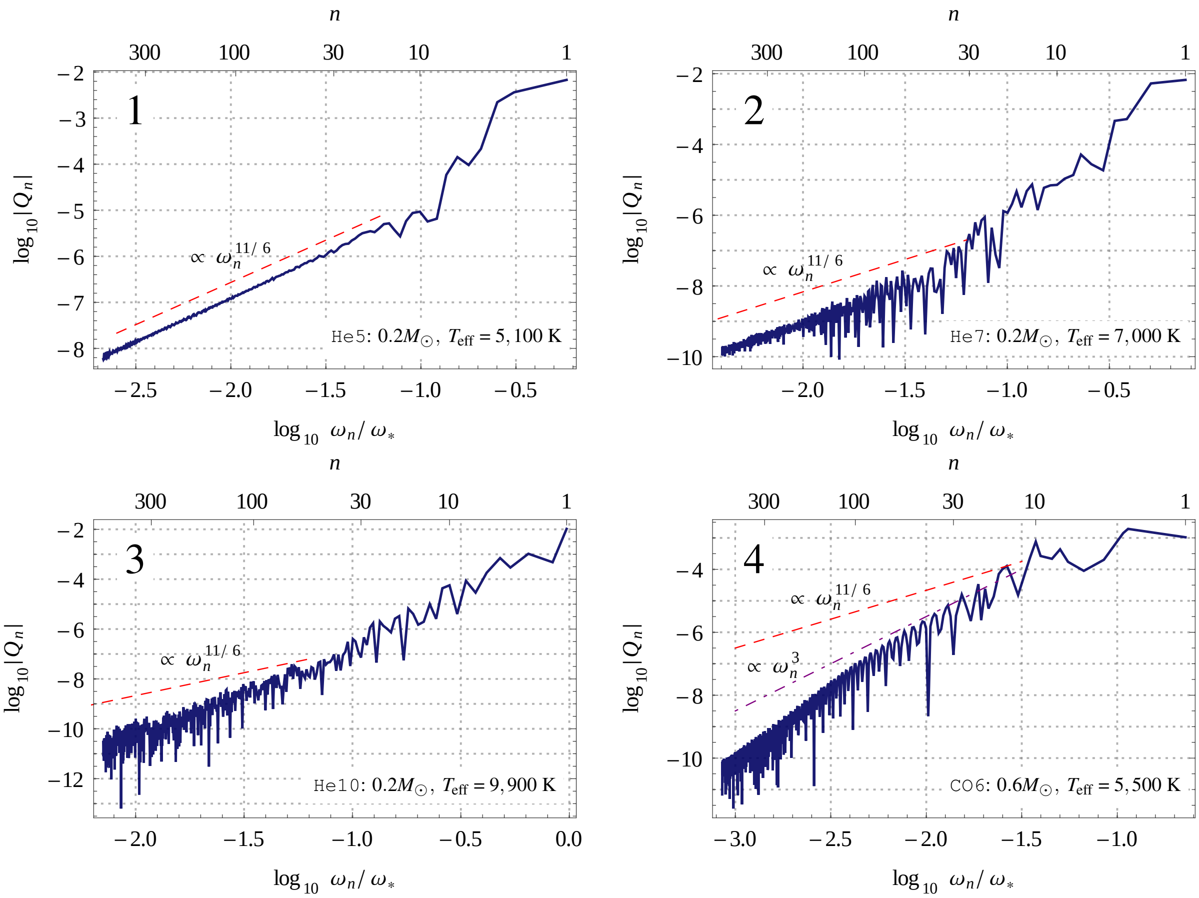

Figure 3.4: Plots of the linear tidal overlap integral Q_n, which characterizes the spatial coupling strength between the tidal potential and a given mode (Appendix B.2.4), as a function of the eigenmode frequency ω_n and radial order n, for the first 500 g-modes in four of our fiducial WD models (Table 3.1). Panels 1 – 3 are helium WDs ordered by increasing temperature; panel 4 is a carbon/oxygen WD. A smooth power law scaling of $Q_n \propto \omega_n^{11/6}$ implies that gravity wave excitation by the tidal potential occurs at the interface between a WD's outer convection zone and its inner radiative core (§ 3.7.1); this can be seen in the cooler helium models from panels 1 & 2. Hotter WDs have smaller convective regions, and wave excitation instead may occur at composition gradient zones (Fuller & Lai 2012a); this mechanism predicts steeper, more jagged profiles of Q_n with ω_n, as in panels 3 & 4.

Table 3.3: WD $l = 2$ eigenmode properties. Asymptotic fits to numerically computed eigenmode properties for the WD models from Table 3.1. The linear overlap integral Q_n (Appendix B.2.4 & Figure 3.4) is fit as $Q_n = Q_0(\omega_n/\omega_{\rm dyn})^a$; the damping rate γ_n (Appendix B.2.3 & Figure B.1) is fit as $\gamma_n = \gamma_0(\omega_n/\omega_{\rm dyn})^{-b}$; and the inverse group travel time $\alpha_n = 2\pi/t_{{\rm group},n}$ (Appendix B.2.3) is fit as $\alpha_n = \alpha_0(\omega_n/\omega_{\rm dyn})^c$. †Note that rapid thermal diffusion near the outer turning point causes g-modes of radial order $n \gtrsim 50$ to become traveling waves in our `CO12` and `He10` models, meaning our fits for γ_n are not relevant in this regime; see Appendix B.2.3 and Figure B.1.

ID	Q_0	a	$\gamma_0/\omega_{\rm dyn}$	b	$\alpha_0/\omega_{\rm dyn}$	c
`He10`†	9.6×10^{-6}	2.61	1.5×10^{-11}	6.16	0.0891	2.00
`He7`	3.6×10^{-6}	1.83	2.1×10^{-12}	2.00	0.158	2.00
`He5`	7.8×10^{-4}	1.90	7.7×10^{-15}	1.99	0.298	2.00
`CO12`†	7.2×10^{1}	4.40	1.2×10^{-14}	6.41	0.403	2.00
`CO6`	2.7×10^{1}	3.69	2.9×10^{-14}	1.88	0.743	2.00

More recently, Fuller & Lai (2012a) showed that excitation can also proceed near the spike in the Brunt-Väisälä frequency that occurs at the transition between carbon/oxygen and helium in a carbon/oxygen WD (see Figure 3.1). Their corresponding prediction for the torque scaling is $\tau \propto \sigma^5$, implying $Q_n \propto \omega_n^3$. Thus this mechanism predicts a steeper overlap scaling with frequency than for excitation at the RCB.

An additional feature of excitation at a composition boundary is that waves originate from a location inside the propagation cavity, meaning both an ingoing and outgoing wave are created. Since the ingoing wave reflects at the inner turning point, interference occurs between the reflected ingoing wave and the purely outgoing wave. Constructive interference implies a large overlap integral Q_n, whereas destructive interference makes the overlap small, thus this mechanism predicts a jagged overlap profile with respect to the wave frequency ω_n.

With these theoretical predictions in hand, the essential question to answer is which excitation mechanism—RCB or composition gradient—is most efficient in a given WD model.[4] The answer hinges on the properties of the convective envelope. Table 3.1 and Figure 3.1 show that this envelope is very small in hot WDs, and exists at very low densities, but that its extent increases rapidly as a WD cools. Thus it seems possible that excitation at the RCB may occur for cooler WDs, whereas hotter WDs must rely on the composition gradient mechanism.

One method we can utilize to distinguish between the two mechanisms is simply to observe the power law scaling $Q_n \propto \omega_n^a$ of numerically computed linear overlap integrals for our various WD models, given in Table 3.3. Consistent with our expectations, cooler helium WDs have a power law index $a \sim 1.83 \approx 11/6$, implying excitation at the RCB, while hotter helium WDs and our carbon/oxygen models have larger values of a. Furthermore, Figure 3.4 shows that models with

[4]This question was not addressed in Fuller & Lai (2012a) since they adopted an absorbing boundary condition near the outer turning point, and thus did not include the convection zone in their calculations.

steeper overlap power laws also show jagged variation of Q_n with frequency, thus demonstrating the interference predicted by composition gradient excitation.

Note that if a gravity wave in a cool helium WD begins to break near its outer turning point (§ 3.6.1), this implies that the tidal excitation and wave breaking regions would be almost directly adjacent. It might then be possible for breaking to inhibit excitation, meaning that the composition gradient mechanism would again dominate. A more sophisticated hydrodynamical calculation is required to address this concern.

3.7.2 Traveling wave resonance locks

The resonance lock scenario we described in § 3.4 relied on resonances between standing WD eigenmodes and the tidal driving frequency. However, resonance locks are in fact a more general phenomenon that does not explicitly require standing waves.[5] In the context of WD binary inspiral, the two essential requirements on the tidal torque function τ in order for a resonance lock to occur are:

a) The torque profile must be a jagged function of the $l = m = 2$ tidal driving frequency $\sigma = 2(\Omega - \Omega_{\rm spin})$ (equation 3.31 below).

b) The magnitude of the tidal torque must be large enough that it can satisfy equation (3.9): $\tau = I_* \Omega / t_{\rm gw}$.

When these conditions are satisfied and a resonance lock occurs, the tidal quality factor $\mathcal{Q}_{\rm t}$ and heating rate are given by equations (3.17) and (3.20), respectively.

We first address criterion (a). Dropping the tidal energy deposition term from equation (3.7), as justified in § 3.4, yields the simplified orbital evolution equation

$$\frac{1}{m}\frac{d\sigma}{d\Omega} = 1 - \frac{t_{\rm gw}\tau}{I_*\Omega}, \tag{3.28}$$

where the gravitational wave decay time $t_{\rm gw}(\Omega)$ is defined in equation (3.1).

Let us assume that the tidal torque satisfies criterion (b) at an orbital frequency Ω_0 and a tidal driving frequency σ_0, so that $d\sigma/d\Omega = 0$ and equation (3.28) reduces to

$$I_*\Omega_0 = t_{\rm gw}(\Omega_0)\tau(\Omega_0, \sigma_0). \tag{3.29}$$

As long as τ increases with σ, equation (3.29) represents a stable fixed point of the evolution equations; see Figure 3.2. Next, since the orbital frequency steadily increases due to the emission of gravitational waves, we examine what happens to this fixed point when Ω changes by a small

[5] In the traveling wave regime, true "resonances" do not occur. Nonetheless, we continue using the term "resonance lock" in this context due to the many similarities between standing wave and traveling wave results. In particular, the tidal evolution scenario associated with what we call a traveling wave resonance lock is identical to that associated with a true resonance lock in the standing wave regime, and the transition between standing and traveling wave torques introduced by wave breaking occurs near would-be standing wave resonances.

amount $+\Delta\Omega$. In order to preserve equation (3.29), the tidal driving frequency must commensurately change by an amount $\Delta\sigma$ given by

$$\frac{\Delta\sigma}{\sigma} = -\frac{1}{3}\left(\frac{\Delta\Omega}{\Omega}\right)\left(\frac{\partial\log\tau}{\partial\log\sigma}\right)^{-1}, \tag{3.30}$$

which can be derived by differentiating equation (3.29) and substituting equation (3.1).

Equation (3.30) allows us to appropriately quantify the "jagged" variation of the torque function required by criterion (a): if

$$\left|\frac{\partial\log\tau}{\partial\log\sigma}\right| \gg 1, \tag{3.31}$$

then the fixed point can be maintained by only a minimal change in the forcing frequency for a given increase in the orbital frequency, thus constituting a resonance lock. Any general power law trend of τ with σ will fail to satisfy this condition—additional sharp features are required.[6]

Torque profiles consistent with equation (3.31) can be provided in several ways. For standing waves, the comb of Lorentzians produced by resonances with eigenmodes (see equation 3.4 and Figure 3.3) easily satisfies equation (3.31), since WD eigenmodes are weakly damped, meaning on- and off-resonance torque values differ by many orders of magnitude. For traveling waves, if the composition gradient mechanism of Fuller & Lai (2012a) discussed in § 3.7.1 is the dominant source of wave excitation, it naturally provides sharp features in the torque function due to wave interference. This can also be observed in Figure 3.5, where the traveling wave torque changes by a factor of ~ 5 as $\sigma = 2\delta\Omega$ changes by only $\sim 10\%$, implying $|d\log\tau/d\log\sigma| \sim 50$.

Lastly, wave breaking can also provide rapid variation in the torque profile due to a sudden transition between standing and traveling wave torques that occurs near resonances at short orbital periods. Specifically, as the tidal driving frequency σ sweeps towards a resonance due to orbital decay by gravitational waves, a tidally excited g-mode's amplitude can become large enough to induce wave breaking (§ 3.6.1), which causes the effective damping rate and hence the resulting torque to increase enormously (see the blue curve in Figure 3.5).

The precise shape of this transition requires hydrodynamical simulations to ascertain. Fortunately, we find that essentially any transition between a nonresonant standing wave torque in between resonances and a traveling wave torque near resonance will satisfy equation (3.31) for WDs, due to the large disparity between typical damping times associated with standing waves and the group travel time, which approximates the damping time for a traveling wave (Table 3.3 & Figure B.1). We discuss this further in § 3.8.

Next, we address criterion (b) for a resonance lock stated at the beginning of this section by estimating the magnitude of the traveling wave torque $\tau_{\rm trav}$. Goodman & Dickson (1998) computed $\tau_{\rm trav}$ caused by dynamical tides raised in solar-type stars by semi-analytically solving for the trav-

[6] Fuller & Lai (2012a) also noticed that $\sigma \approx$ constant occurred in their simulations, although they attributed this to the overall power law trend of their torque function with σ. Indeed, their results possess sharp interference-generated features that provide a much larger contribution to $|d\log\tau/d\log\sigma|$ than the trend, meaning a resonance lock was likely responsible for maintaining $\sigma \approx$ constant.

eling wave tidal response.[7] Then, to approximate the effect of discrete resonances, they attached Lorentzian profiles to their formula for $\tau_{\rm trav}$. We reverse this procedure, and instead approximate $\tau_{\rm trav}$ by our standing wave formula in the limit that the mode damping time approaches the group travel time. We establish the fidelity of this approximation in Appendix B.3.

We thus compute $\tau_{\rm trav}$ by first using equation (3.5) with the tidal driving frequency σ set to a particular eigenfrequency ω_n, γ_n replaced by $\alpha_n = 2\pi/t_{{\rm group},n}$ (where $t_{\rm group}$ is the group travel time; see Appendix B.2.3), and $\delta\omega_n$ set to zero. This yields

$$\tau_{\rm trav}(\sigma = \omega_n, \Omega) \sim 4E_*\varepsilon^2 Q_n^2 \omega_n/\alpha_n, \tag{3.32}$$

where we have approximated $W^2 \approx 1$. Then, in order to evaluate an effective traveling wave torque for arbitrary σ, we simply interpolate over values computed using equation (3.32).

To estimate the first orbital period $P_{\rm trl}$ at which traveling wave resonance locks can occur, we follow the same procedure as in § 3.4 and again invoke approximate scalings for the eigenmode linear tidal overlap integral Q (Appendix B.2.4) and the effective traveling wave damping rate α (Appendix B.2.3):

$$Q \approx Q_0(\sigma/\omega_{\rm dyn})^a \quad \text{and} \quad \alpha \approx \alpha_0(\sigma/\omega_{\rm dyn})^c,$$

where $c = 2$; see Table 3.3 and Figure B.1. The resulting formula, scaled to values for our `CO6` model (Table 3.1), is

$$P_{\rm trl} \sim 43 \text{ min} \left(\frac{t_*}{2.9 \text{ s}}\right) F_{\rm trl}^q, \tag{3.33}$$

where $t_* = (R^3/GM)^{1/2}$ is the WD's dynamical time, the factor $F_{\rm trl}$ is

$$\begin{aligned} F_{\rm trl} \sim & \left(\frac{M'}{M}\right)\left(\frac{1+M'/M}{2}\right)^{-5/3} \\ & \times \left(\frac{\beta_*}{0.010}\right)^{-5}\left(\frac{I_*}{0.18MR^2}\right)^{-1} \\ & \times \left(\frac{Q_0}{27}\right)^{2}\left(\frac{\alpha_0}{0.74\omega_{\rm dyn}}\right)^{-1} \\ & \times \left(8.41\times 10^{12}\right)(0.0119)^{1/q}, \end{aligned} \tag{3.34}$$

the power q is in general

$$q = \frac{1}{-1/3+2a} < 1, \tag{3.35}$$

and $q = 0.15$ for our `CO6` model (Table 3.3). (The last line of equation 3.34 is equal to unity for $q = 0.15$.) Equation (3.33) assumes the WD begins completely unsynchronized; it is equivalent to equation (79) of Fuller & Lai (2012a).

[7] Goodman & Dickson (1998) explicitly computed the tidal energy deposition rate $\dot{E}_{\rm tide}$; this can be converted to a torque using equation (B.20).

Direct numerical evaluation of eigenmode properties with our `CO6` WD model yields $P_{\rm trl} = 40$ min for an equal-mass companion, due to an $n = 27$ g-mode, which agrees well with equation (3.33). Values of $P_{\rm trl}$ for each of our fiducial models are provided in Table 3.2. Note, however, that in deriving these results for $P_{\rm trl}$ we have assumed that the WD spin is much smaller than the orbital frequency; if significant synchronization has already occurred, the true value of $P_{\rm trl}$ will deviate from our prediction by an order-unity factor.

3.8 Numerical simulations

To address the tidal evolution of an inspiraling WD binary undergoing resonance locks, we aim to combine the standing and traveling wave results from §§ 3.4 & 3.7 numerically. To this end, we evaluate the complete standing wave tidal torque from equation (3.4) and solve for the spin and orbital evolution using equation (3.7). To account for wave breaking, we check that all eigenmodes satisfy $|k_r\xi_r|_{\rm max} < 1$ throughout the WD (§ 3.6.1); when an eigenmode exceeds unit shear, we instead set its damping rate to $\alpha_n = 2\pi/t_{{\rm group},n}$ (Appendix B.2.3), which approximates the traveling wave regime (Goodman & Dickson 1998). We smoothly transition between the standing and traveling wave regimes using the interpolation formula

$$\tau = \frac{\tau_{\rm stand} + \tau_{\rm trav}\left(|k_r\xi_r|_{\rm max}\right)^z}{1+\left(|k_r\xi_r|_{\rm max}\right)^z}, \tag{3.36}$$

where $\tau_{\rm stand}$ is the standing wave torque from equation (3.4), $\tau_{\rm trav}$ is the traveling wave torque produced by interpolating over equation (3.32), and $|k_r\xi_r|_{\rm max}$ is the maximum value of the wave shear over all relevant eigenmodes and across the entire propagation cavity (§ 3.6.1), evaluated assuming standing waves. We arbitrarily adopt $z = 25$ to induce a sharp transition that occurs only when $|k_r\xi_r|_{\rm max}$ is very close to 1; our results are insensitive to the value of z so long as it is $\gtrsim |\ln(\tau_{\rm trav}/\tau_{\rm stand})|$. Figure 3.5 shows a comparison of $\tau_{\rm stand}$, $\tau_{\rm trav}$, and the transition function in equation (3.36).

Figure 3.6 shows the results of two of our simulations. The left column used our $0.2M_\odot$, $T_{\rm eff} = 7{,}000$ K `He7` model, while the right column used our $0.6M_\odot$, $T_{\rm eff} = 5{,}500$ K `CO6` model (Table 3.1). We did not account for WD cooling or tidal heating, and instead used fixed WD models throughout both simulations. We initialized our simulations with $\Omega_{\rm spin} \sim 0$, and the orbital period set so that the time until mass transfer $t_{\rm merge} = 3t_{\rm gw}/8$ (equation 3.1) was equal to 10 billion years.

Both simulations follow the archetypal scenario laid out in § 3.3, transitioning amongst the four regimes (S1), (S2), (T1), and (T2). Both begin in (S1), where the dynamical tide is a standing wave even near resonances, but the tidal torque is too weak to create a resonance lock. As the orbit shrinks due to gravitational wave radiation, the tidal force waxes and the first resonance lock eventually begins in both simulations at the appropriate value of $P_{\rm rl}$ estimated in § 3.4 and provided in Table 3.2; this is regime (S2). At this point tidal heating and synchronization suddenly become much more efficient (§ 3.5), and the difference between orbital and spin frequencies remains con-

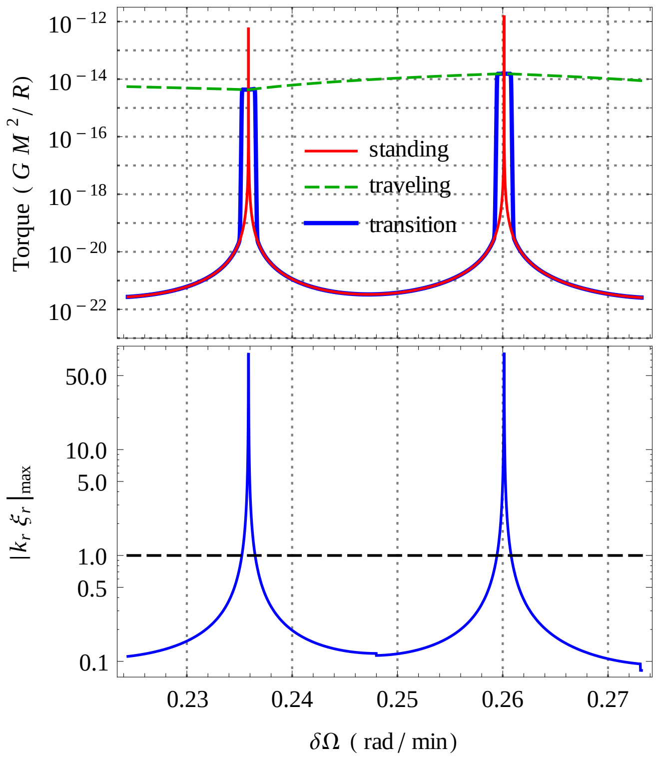

Figure 3.5: *Top panel:* Example plot of the standing wave torque $\tau_{\rm stand}$ (equation 3.4; red line), the traveling wave torque $\tau_{\rm trav}$ (interpolation over equation 3.32 evaluated at eigenmode frequencies; dashed green line), and our interpolation between the two regimes (equation 3.36; thick blue line), as functions of $\delta\Omega = \Omega - \Omega_{\rm spin}$ at fixed $P_{\rm orb}$ = 30 min for our `CO6` model (Table 3.1) and an equal-mass companion. The standing wave torque on average is many orders of magnitude smaller than the traveling wave torque; however, near resonances it becomes many orders of magnitude larger. Wave breaking acts to "cap" the Lorentzian peaks of the standing wave torque in the interpolation function. *Bottom panel:* Plot of the wave breaking criterion $|k_r\xi_r|$ maximized over all eigenmodes and the entire propagation cavity (blue line), using the same parameters and model as the top panel. When $|k_r\xi_r|_{\rm max} < 1$, the dynamical tide represents a traveling wave, and the torque $\tau \to \tau_{\rm stand}$; when $|k_r\xi_r|_{\rm max} > 1$, wave breaking occurs, and $\tau \to \tau_{\rm trav}$ (§ 3.6.1).

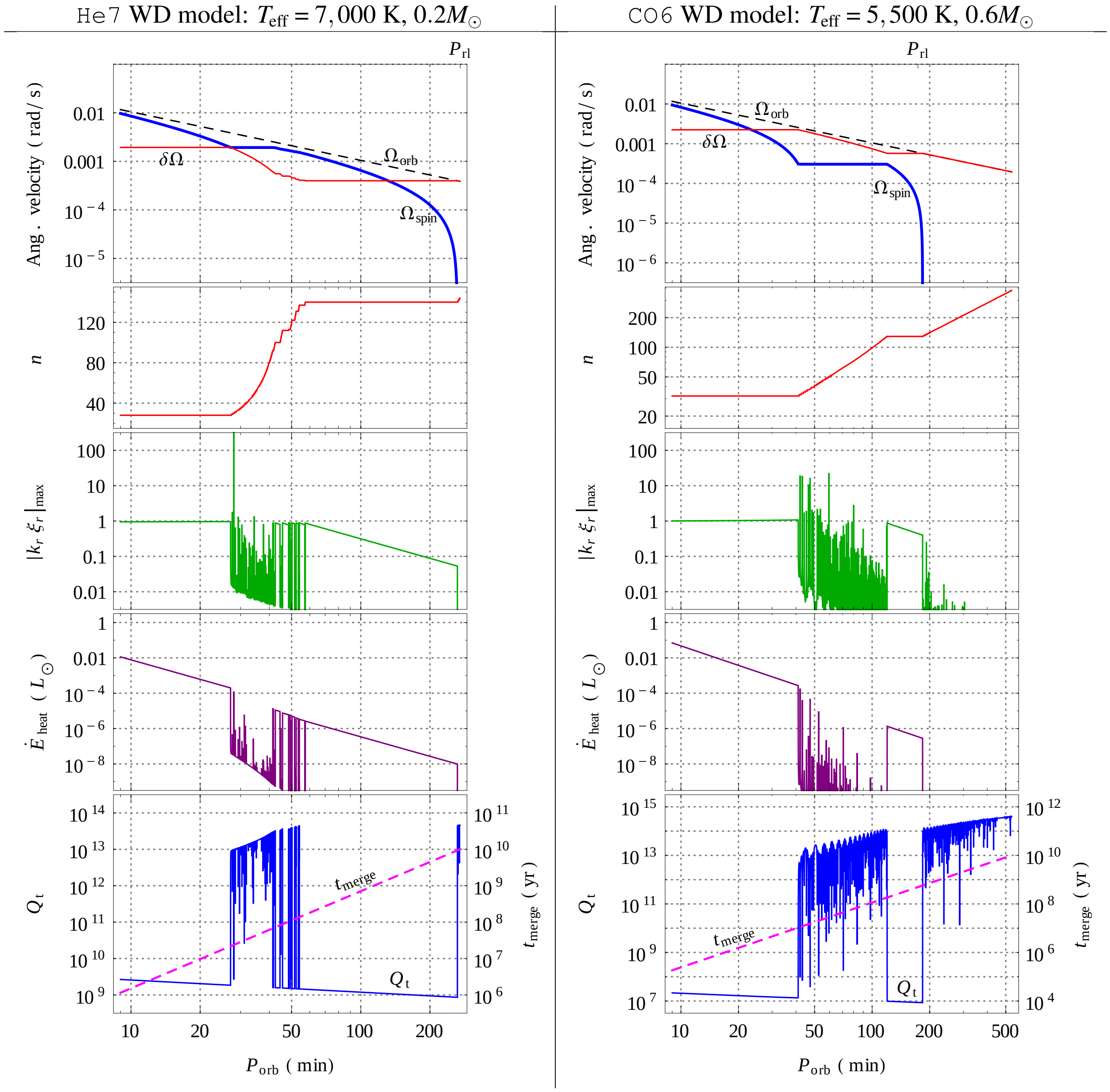

Figure 3.6: Results of numerical simulations of the secular evolution of WD binaries, the details of which are described in § 3.8. The left column shows results using our $0.2M_\odot$, $T_{\rm eff} = 7{,}000$ K He7 model, while the right column used our $0.6M_\odot$, $T_{\rm eff} = 5{,}500$ K CO6 model (Table 3.1). *Top row:* The orbital (dashed black line) and spin (thick blue line) frequencies, as well as their difference $\delta\Omega = \Omega - \Omega_{\rm spin}$ (red line); the latter sets the tidal forcing frequency $\sigma = 2\delta\Omega$. Resonance locks correspond to regions where $\delta\Omega$ is constant. Our assumption of slow rotation breaks down when $\delta\Omega \lesssim \Omega_{\rm spin}$ due to nonlinear rotational modification of stellar eigenmodes. *Second row:* Number of radial nodes n of dominant eigenmode/wave. *Third row:* Maximum value of $|k_r\xi_r|$ across entire WD, evaluated assuming standing waves, which assesses whether wave breaking occurs (§ 3.6.1). During the initial resonance lock, $|k_r\xi_r|_{\rm max}$ starts < 1, but gradually rises until it becomes ~ 1 and breaking begins. *Fourth row:* Rate at which orbital energy is dissipated as heat in the WD, in units of $L_\odot$. *Bottom row:* Tidal quality factor $Q_{\rm t}$ (blue line) and time until mass transfer $t_{\rm merge} = 3t_{\rm gw}/8$ (equation 3.1; dashed magenta line). See equations (3.17) and (3.20) for analytic estimates of the tidal quality factor $Q_{\rm t}$ and heating rate, respectively.

stant. Analytic formulas for the tidal quality factor and heating rate appropriate for this situation (as well as T2 discussed below) are given in equations (3.17) and (3.20), respectively, and exactly reproduce their numerically derived values appearing in the bottom two rows of Figure 3.6.

Both simulations begin the standing wave resonance lock regime (S2) with a value of the wave breaking criterion $|k_r \xi_r|_{\rm max} < 1$; however, as the orbit shrinks further, progressively larger and larger wave amplitudes become necessary to support a resonance lock, eventually leading to wave breaking near the outer turning point (§ 3.6.1). At the onset of (S2) in the `CO6` simulation, the inequality $|k_r \xi_r|_{\rm max} < 1$ is only weakly satisfied, meaning that the standing wave lock regime (S2) is short lived. In the `He7` simulation, however, (S2) begins with $|k_r \xi_r|_{\rm max} \ll 1$, so that the initial resonance lock persists from $P_{\rm rl} = 270$ min to a period of $P \approx 50$ min, corresponding to an interval of time of about 5 billion years.

Once $|k_r \xi_r|_{\rm max}$ becomes ~ 1, both simulations enter regime (T1), where near would-be resonances the dynamical tide becomes a traveling wave too weak to create a resonance lock. The otherwise steeply peaked standing wave torque is thus capped in this regime; see Figure 3.5. Regime (T1) results in a weak tidal synchronization and heating scenario, very similar to (S1).

Eventually, at an orbital period $\sim P_{\rm trl}$ (§ 3.7.2; Table 3.2), both simulations enter regime (T2), where even the traveling wave torque can create a resonance lock (terminology discussed further in footnote 5). Tides again become efficient, with synchronization and heating scenarios quantitatively consistent with the analytic results in § 3.5 (just as in S2). In the `He7` simulation, (T2) begins at an orbital period of ≈ 27 min, which differs from its value of $P_{\rm trl} = 49$ min listed in Table 3.2, since that value is only strictly applicable when $\Omega_{\rm spin} = 0$, whereas significant synchronization has already occurred. The value of $P_{\rm trl}$ in the `CO6` simulation is a better estimate of the onset of (T2) due to the brief duration of (S2) in that case.

The maximum wave shear $|k_r \xi_r|_{\rm max}$ shown in Figure 3.6 (which is evaluated assuming standing waves) remains very close to unity throughout much of regime (T2). A reasonable question, then, is whether this is an artifact of the interpolation function we used to transition between standing and traveling waves torques (equation 3.36).

On the contrary, we believe there is a physical reason why $|k_r \xi_r|_{\rm max}$ should saturate at ~ 1, and that it is a natural consequence of the traveling wave resonance lock scenario we proposed in § 3.7.2. Specifically, at this point in the system's evolution, if the dynamical tide attempts to set up a standing wave, the orbital frequency will evolve, increasing the tidal driving frequency $\sigma = 2(\Omega - \Omega_{\rm spin})$ towards a resonance and inducing wave breaking. However, fully transitioning to the traveling wave regime then creates a much larger torque (due to the much larger effective damping rate), causing the spin frequency to increase rapidly and sending σ away from resonance, ending wave breaking and reinstituting the standing wave regime. The end result is that $|k_r \xi_r|_{\rm max}$ should average to be ~ 1.

This line of reasoning suggests that the true phenomenon may be episodic in nature. Alternatively, a weak-breaking regime may be possible, allowing the system to smoothly skirt the boundary between linear and nonlinear fluid dynamics. Full hydrodynamical simulations may be necessary to understand this in more detail.

3.9 Discussion

3.9.1 Observational constraints

The theoretical results we have developed can be compared to the recently discovered system SDSS J065133.33+284423.3 (henceforth J0651), which consists of a $T_{\rm eff} = 16,500$ K, $0.26M_\odot$ helium WD in a 13-minute eclipsing binary with a $T_{\rm eff} = 8,700$ K, $0.50M_\odot$ carbon/oxygen WD (Brown et al. 2011). Orbital decay in this system consistent with the general relativistic prediction was discovered by Hermes et al. (2012).

Piro (2011) studied tidal interactions in J0651, and produced lower limits on values of the tidal quality factor $Q_{\rm t}$ by assuming that the observed luminosity of each WD is generated entirely by tidal heating, and that both WDs are nonrotating. However, the definition of $Q_{\rm t}$ used in that work differs with ours (equation 3.13), which hinders straightforward comparison.[8]

Instead, we compare the observed luminosities with our expression for $\dot{E}_{\rm heat}$ from equation (3.20), which is applicable during a resonance lock. All parameters for J0651 entering into (3.20) were determined observationally except the moments of inertia I_* and the asynchronicity periods $\delta P = 2\pi/\delta\Omega$, where $\delta\Omega = \Omega - \Omega_{\rm spin}$. Note that equation (3.20) counterintuitively shows that greater synchronization leads to diminished tidal heating, since the heating rate is proportional to the degree of synchronization (and hence inversely proportional to δP). We can thus use appropriate values of I_* from Table 3.1 and impose the inequality $L \gtrsim \dot{E}_{\rm heat}$, since cooling can also contribute to each luminosity, in order to constrain δP for each WD.

This calculation yields $\delta P \gtrsim 7$ min for the helium WD and $\delta P \gtrsim 400$ min for the carbon/oxygen WD, each with uncertainties of $\sim 20\%$. Since the orbital period of J0651 is such that resonance locks should currently exist in both WDs—$P_{\rm orb}$ is less than both $P_{\rm rl}$ from § 3.4 for standing waves and $P_{\rm trl}$ from § 3.7.2 for traveling waves (Table 3.2)—and since our simulations developed wave breaking long before $P_{\rm orb} = 13$ min (Figure 3.6), our *a priori* expectation is that δP should be $\sim P_{\rm trl} \sim 50$ min for each WD. It is encouraging that the inferred constraints on δP for both WDs are within an order of magnitude of this prediction.

We can nonetheless comment on what the deviations from our predictions may imply. First, the fact that $\delta P > 7$ min $< P_{\rm orb} = 13$ min for the helium WD means that explaining its luminosity purely by tidal heating would require retrograde rotation. Since this situation would be highly inconsistent with our results, we can conclude that its luminosity must be generated primarily by standard WD cooling or residual nuclear burning rather than tidal heating. If this is correct, it would imply an age for the helium WD of only ~ 40 Myr (Panei et al. 2007); dividing this age by a cooling time of ~ 1 Gyr (Table 3.1) yields a very rough probability for finding such a system of $\sim 4\%$. This scenario does not seem unlikely, however, since selection bias favors younger WDs.

On the other hand, the inferred lower limit of ~ 400 min placed on δP for the carbon/oxygen WD is much larger than our predictions for both $P_{\rm rl}$ and $P_{\rm trl}$. Furthermore, we find that tidal heat is deposited very close to the photosphere in hot carbon/oxygen WD models (Table 3.1), so we expect

[8] The relationship between our value of the tidal quality factor, $Q_{\rm t}$, and that used in Piro (2011), $Q'_{\rm t}$, is $Q'_{\rm t} = Q_{\rm t}\sigma M/\lambda\Omega\mu$, where μ is the reduced mass. Our value $Q_{\rm t}$ is consistent with being the reciprocal of an effective tidal lag angle, which is the conventional definition; see § 3.5.1.

tidal heating to contribute directly to the luminosity of the carbon/oxygen WD in J0651 (§ 3.5.2). The constraint on δP thus means that the carbon/oxygen WD appears to be more synchronized than our theoretical expectation, and consequently less luminous than our prediction by a factor of $\sim 400\,\mathrm{min}/P_{\mathrm{trl}} \sim 10$.

Although this is formally inconsistent with our results, examining the first row of Figure 3.6 shows that both of our numerical simulations have $\delta\Omega \ll \Omega_{\mathrm{spin}}$ near $P_{\mathrm{orb}} = 13$ min. This means that the influence of rotation on eigenmode properties is likely to be very important at such short orbital periods (§ 3.9.2), which is not included in our analysis. This could lead to enhanced synchronization and hence mollify the discrepancy (since, again, increased synchronization implies less tidal heating). Damping and excitation of WD eigenmodes by nonlinear processes are also likely to be important considerations, which could also increase the efficiency of tidal synchronization.

Lastly, assuming resonance locks are occurring in both WDs, we predict that the rate of orbital decay should be enhanced due to tides by (§ 3.5.3)

$$\left(\frac{\dot{P}_{\mathrm{tide}}}{\dot{P}_{\mathrm{gw}}}\right)_{\mathrm{J0651}} \sim 3\%,$$

where $\dot{P}_{\mathrm{gw}} = -P_{\mathrm{orb}}/t_{\mathrm{gw}}$. Although this estimate fails to include the effect of rotation on eigenmode frequencies, which we already argued may be important in J0651, it should nonetheless be robust at the order-of-magnitude level. This $\sim 3\%$ deviation between the system's period derivative and the general relativistic prediction not accounting for tides may be detectable given further sustained observations (Piro 2011).

3.9.2 Rotation and WD evolution

In our analysis we have neglected the influence of rotation on the stellar eigenmodes beyond the simple geometrical Doppler shift of the forcing frequency into the corotating frame. To linear order in the rotation frequency, the correction to the stellar eigenfrequencies makes very little difference to the results we have derived—it just means there should be factors of $(1-C_n) \sim 5/6$ appearing in various formulas in § 3.4, which we neglected for simplicity.

However, when $\delta\Omega = \Omega - \Omega_{\mathrm{spin}} \lesssim \Omega_{\mathrm{spin}}$, nonlinear rotational effects become important. Figure 3.6 shows that this inequality is satisfied below $P_{\mathrm{orb}} \sim 25$ min in our `CO6` simulation, and takes hold soon after the first resonance lock in our `He7` simulation, at only $P_{\mathrm{orb}} \sim 150$ min. Below these orbital periods, fully accounting for the Coriolis force in the stellar oscillation equations becomes necessary.

For example, excitation of rotationally supported modes—Rossby waves and inertial waves—could prove very efficient. Such modes have corotating-frame eigenfrequencies that are strongly dependent on the rotation frequency, so a resonance lock would follow the more general trajectory (Witte & Savonije 1999)

$$0 = \delta\dot{\omega} = m\left[\left(1 + \frac{1}{m}\frac{\partial\omega_n}{\partial\Omega_{\mathrm{spin}}}\right)\dot{\Omega}_{\mathrm{spin}} - \dot{\Omega}\right]. \tag{3.37}$$

Since our analysis in § 3.5 relied on resonance locks producing $\dot{\Omega} \approx \dot{\Omega}_{\rm spin}$, which no longer holds when $\partial\omega_n/\partial\Omega_{\rm spin} \neq 0$, it is unclear whether nonlinear rotational effects could substantially alter our results for e.g. the tidal quality factor (equation 3.17) and tidal heating rate (equation 3.20).

WD cooling and tidal heating could also potentially modify the synchronization trajectory that results during a resonance lock. For example, since g-mode frequencies approximately satisfy $\omega_{nl} \sim \langle N \rangle l/n$, and since the Brunt-Väisälä frequency scales with temperature as $N \propto T^{1/2}$ in a degenerate environment (§ 3.2), progressive changes in a WD's thermal structure due to either heating or cooling would introduce an additional $\partial\omega_n/\partial t$ term on the right-hand side of equation (3.37).

3.9.3 Crystallization

Whether a plasma begins to crystallize due to ion-ion electromagnetic interactions is determined by the Coulomb interaction parameter Γ, which is defined as the ratio of the Coulomb to thermal energy,

$$\Gamma = \frac{Z^2 e^2}{d_{\rm i} kT}, \tag{3.38}$$

where Ze is the mean ion charge and $d_{\rm i}$ is the ion separation, defined by $1 = n_{\rm i}(4\pi/3)d_{\rm i}^3$. When $\Gamma \gtrsim 1$, the plasma under consideration behaves as a liquid; when $\Gamma > \Gamma_{\rm crys}$, the plasma crystallizes. This critical value is $\Gamma_{\rm crys} \sim 175$ in single-component plasmas (Dewitt et al. 2001). However, more recent observational studies of carbon/oxygen WD populations (Winget et al. 2009) as well as detailed theoretical simulations (Horowitz et al. 2007) indicate that a larger value of $\Gamma_{\rm crys} \sim 220$ is applicable for two-component plasmas, as in the cores of carbon/oxygen WDs.

As shown in Table 3.1, the central value of Γ does not exceed the appropriate value of $\Gamma_{\rm crys}$ for any of our helium WDs. However, for `CO6`, our $0.6M_\odot$, $T_{\rm eff} = 5{,}500$ K carbon/oxygen WD, we have $\Gamma_{\rm core} = 260 > \Gamma_{\rm crys}$, and further $\Gamma > \Gamma_{\rm crys}$ for 19% of the model by mass (taking $\Gamma_{\rm crys} = 220$). This is indicated in the bottom panel of Figure 3.1 as a shaded region.

The excitation of dynamical tides in WDs possessing crystalline cores is an interesting problem that deserves further study. We will only speculate here on the possible physical picture. Our preliminary calculations of wave propagation inside the crystalline core, using expressions for the shear modulus of a Coulomb crystal from Hansen & van Horn (1979), indicate that the shear wave Lamb frequency is several orders of magnitude too large to allow gravity waves to propagate as shear waves in the core.

Thus it seems possible that dynamical tides could be efficiently excited at the edge of the core, as in excitation at the edge of a convective core in early-type stars (Zahn 1975). In this scenario the deviation of the tidal response inside the crystal from the potential-filling equilibrium tide solution excites outward-propagating g-modes. As a consequence, tidal gravity waves may be much more efficiently excited in crystalline core carbon/oxygen WDs, since the Brunt-Väisälä frequency gradient near the core would be much steeper than in any composition gradient zone, as discussed in § 3.7.1.

3.9.4 Nonlinear damping

Since eigenmodes responsible for resonance locks in the standing wave regime attain large amplitudes, it is natural to worry that they might be unstable to global nonlinear damping by the parametric instability, even if they don't experience wave breaking (e.g. Arras et al. 2003; Weinberg et al. 2012). To address this, we performed a rough estimate of the threshold amplitude T for the parametric instability to begin sapping energy from the eigenmode responsible for the standing wave resonance lock in our `CO6` simulation from § 3.8. Using the procedure detailed in § 6.5 of Burkart et al. (2012), we found $T \sim 2 \times 10^{-8}$. On the other hand, during the resonance lock the mode in question began with an amplitude of $|q| \sim 4 \times 10^{-8}$, which grew to $\sim 10^{-7}$ before wave breaking destroyed the lock.

This demonstrates that parametric instabilities may limit the achievable amplitudes of standing waves in close WD binaries, potentially somewhat more stringently than wave breaking alone. Exactly how this affects the overall tidal synchronization scenario requires more detailed study.

3.10 Conclusion

In this paper, we have studied the linear excitation of dynamical tides in WD binaries inspiraling subject to gravitational wave radiation. We showed that the phenomenon of resonance locks occurs generically in this scenario, both when the dynamical tide represents a standing wave or a traveling wave. (Our choice of terminology is discussed further in footnote 5.)

In a resonance lock, as the orbital frequency increases according to $\dot{\Omega} = \Omega/t_{\rm gw}$, where $t_{\rm gw}$ is the gravitational wave inspiral time (equation 3.1), a synchronizing torque produced by the dynamical tide causes the WD spin frequency to evolve at nearly the same rate: $\dot{\Omega}_{\rm spin} \approx \dot{\Omega}$ (§ 3.4). This means the $l = m = 2$ tidal driving frequency $\sigma = 2(\Omega - \Omega_{\rm spin})$ remains constant, which in turn keeps the tidal torque nearly constant, leading to a stable situation. In other words, a resonance lock is a dynamical attractor (Figure 3.2).

We first considered resonance locks created by standing waves, where resonances between the tidal driving frequency and WD eigenmodes create the synchronizing torque required to maintain $\sigma \approx$ constant. We derived analytic estimates of the orbital period $P_{\rm rl}$ at which such resonance locks can first occur (§ 3.4; also Table 3.2): $P_{\rm rl} \sim 30$ min for hot carbon/oxygen WDs ($T_{\rm eff} \sim 12{,}000$ K) and $P_{\rm rl} \sim 200$ min for cold carbon/oxygen WDs ($T_{\rm eff} \sim 6{,}000$ K). For helium WDs, we found $P_{\rm rl} \sim 70$ min for hot models ($T_{\rm eff} \sim 10{,}000$ K), and $P_{\rm rl} \sim 1$ day for colder models ($T_{\rm eff} \sim 5{,}000$ K).

Tides preferentially deposit orbital angular momentum into a WD's outermost layers, where wave damping is most efficient. A concern thus exists that a synchronously rotating critical layer might develop, causing rapid wave damping and eliminating the possibility of maintaining a standing wave (Goldreich & Nicholson 1989b). However, we showed that critical layers are in fact unlikely to develop in the standing wave regime of WD binary inspiral, since a typical WD fossil magnetic field is capable of winding up and enforcing solid-body rotation throughout the WD down to orbital periods of ~ 10 min or less (§ 3.6.2; Appendix B.1).

We derived analytic formulas for the tidal quality factor $\mathcal{Q}_{\rm t}$ (equation 3.17) and heating rate $\dot{E}_{\rm heat}$ (equation 3.20) during a resonance lock (§ 3.5). (Since $\mathcal{Q}_{\rm t}$ parametrizes the total tidal energy transfer rate, including mechanical energy associated with changing the WD spin, values of Q_t alone do not determine the tidal heating rate.) Our results predict that, for orbital periods of $\lesssim$ hours, $Q_t \sim 10^7$ for carbon/oxygen WDs and $Q_t \sim 10^9$ for helium WDs. Our formula for Q_t is independent of WD eigenmode properties and weakly dependent on the orbital period, scaling as $Q_t \propto P_{\rm orb}^{-1/3}$. It is, however, strongly dependent on the WD mass and radius. We also found that tidal heating begins to rival typical WD luminosities for $P_{\rm orb} \lesssim 10$ min, a result that is relatively insensitive to WD properties due to the steep power law scaling $\dot{E}_{\rm heat} \underset{\sim}{\propto} P_{\rm orb}^{-11/3}$. The analytic results we derived can easily be incorporated into population synthesis models for the evolution of close WD binaries.

As a standing wave resonance lock proceeds, the wave amplitude required to maintain synchronization grows. Eventually, the amplitude becomes so large that the standing wave begins to break near the surface convection zone (§ 3.6.1). This causes the dynamical tide to become a traveling wave, eliminating the resonance lock. This occurred soon after the initial resonance lock in our $0.6 M_\odot$, $T_{\rm eff} = 5{,}500$ K carbon/oxygen WD simulation; however, the standing wave resonance lock lasted much longer in our $0.2 M_\odot$, $T_{\rm eff} = 7{,}000$ K helium WD simulation, from $P_{\rm orb} \sim 250$ min down to ~ 40 min, amounting to ~ 10 Gyr of binary evolution.

Resonance locks have traditionally been considered only when the dynamical tide represents a standing wave (Witte & Savonije 1999). We showed, however, that given sufficiently short orbital periods, resonance locks can even occur in the traveling wave regime (§ 3.7.2). We derived two simple criteria for whether traveling waves can effect resonance locks: the traveling wave torque must be large enough to enforce $\dot{\Omega} \approx \dot{\Omega}_{\rm spin}$, and the torque profile as a function of the tidal driving frequency $\sigma = 2(\Omega - \Omega_{\rm spin})$ must possess "jagged" features, a concept quantified by $|d \log \tau / d \log \sigma| \gg 1$ (equation 3.31), where τ is the tidal torque.

The first criterion is satisfied for orbital periods below a critical period $P_{\rm trl}$, which we found to be $P_{\rm trl} \sim 40 - 50$ min in most WD models (equation 3.33; Table 3.2). The second criterion can be satisfied by rapid transitions between standing and traveling wave torques (which differ by orders of magnitude) near resonances as a result of wave breaking (§ 3.6.1), or by wave interference due to excitation by a composition gradient (§ 3.7.1; Fuller & Lai 2012a). Excitation likely proceeds at a composition gradient in carbon/oxygen WDs and hot helium WDs, but excitation at the radiative-convective boundary becomes important for colder helium WDs with larger surface convection zones (§ 3.7.1). Excitation off a crystalline core may also be important in cold carbon/oxygen WDs (§ 3.9.3).

Even after the initial standing wave resonance lock is destroyed by wave breaking, a new traveling wave resonance lock takes hold once the orbital period declines to $P_{\rm orb} \sim P_{\rm trl} \sim 40 - 50$ min. The synchronization trajectory and corresponding values of the tidal quality factor (equation 3.17) and tidal heating rate (equation 3.20) are the same during a traveling wave resonance lock. We confirmed our analytic derivations with numerical simulations that smoothly switched between standing and traveling wave torques based on the maximal value of the wave shear $|k_r \xi_r|$ (Figure 3.5), with wave breaking leading to traveling waves for $|k_r \xi_r| \gtrsim 1$ (§ 3.6.1). We presented the results of two simulations, one with a helium WD and one with a carbon/oxygen WD, in § 3.8. Once the traveling wave resonance lock began, synchronization in our numerical calculations proceeded until the spin frequency $\Omega_{\rm spin}$ became larger than $\delta\Omega = \Omega - \Omega_{\rm spin}$, meaning nonlinear rotational effects not included in our analysis were likely to be important (§ 3.9.2).

Our numerical calculations (Figure 3.6) demonstrate that efficient tidal dissipation is produced by standing wave resonance locks at large orbital periods, and by traveling wave resonance locks at smaller orbital periods. The importance of the standing wave resonance lock regime at large orbital periods can be tested by measuring the rotation rates of wide WD binaries. We predict that systems with orbital periods of hours should have undergone significant synchronization (Figure 3.6), while models that focus solely on excitation of traveling waves (Fuller & Lai 2012a) would predict synchronization only at significantly shorter orbital periods. A second prediction of our model is that there may be a range of intermediate orbital periods (e.g., 20 min $\lesssim P_{\rm orb} \lesssim$ 40 min) where tidal dissipation is relatively inefficient compared to both smaller and somewhat larger orbital periods.

The results derived here can be directly compared to the recently discovered 13-minute WD binary J0651 (§ 3.9.1). We predict a $\sim 3\%$ deviation of the orbital decay rate from the purely general relativistic value, which may be measurable given further observations. We also find that our predicted tidal heating rates are within an order of magnitude of the observed luminosities. This broad agreement is encouraging given the well-known difficulties tidal theory has accurately predicting the efficiency of tidal dissipation in many stellar and planetary systems.

In detail, we find that even if the helium WD is nonrotating (which maximizes the tidal energy dissipated as heat), tidal heating is a factor of ~ 2 less than the observed luminosity, strongly suggesting that much of its luminosity must derive from residual nuclear burning or cooling of thermal energy rather than tidal heating. In contrast, we predict that the carbon/oxygen WD in J0651 should be ~ 10 times more luminous than is observed. We suspect that the origin of this discrepancy is the importance of rotational modification of stellar eigenmodes at the short orbital period present in J0651 (§ 3.9.2), and perhaps the effects of nonlinear damping/excitation of stellar oscillations (e.g. § 3.9.4; Weinberg et al. 2012). These will be studied in future work.

Chapter 4

Dynamical resonance locking

4.1 Introduction

The most frequent treatment of tidal effects in detached binaries relies on the weak-friction theory (Murray & Dermott 1999), which considers only the large-scale "equilibrium tide" (i.e., filling of the Roche potential) with dissipation parameterized by the tidal quality factor Q (Goldreich & Soter 1966). Such a treatment fails to account for the resonant excitation of internal stellar waves with intrinsic frequencies comparable to the tidal forcing—the so-called "dynamical tide" (Zahn 1975).

Many studies have considered the dynamical tide in different astrophysical contexts. There are two possible regimes: when the character of the excited modes is that of radially traveling waves, or when they represent standing waves. A traveling wave occurs when reflection is prohibited by a strong dissipative process at some radial location in the star or planet in question—e.g., rapid linear dissipation near the surface or nonlinear wave breaking.

The standing wave regime is the subject of this paper. This is applicable when a wave's amplitude can be built up by many reflections. Existing calculations in this regime have used at least one of the following two approximations: 1) tides do not backreact on the spin of the star or planet in question (Lai 1994; Rathore et al. 2005; Fuller & Lai 2011), or 2) the mode amplitude is not treated as a dynamical variable, and instead has its amplitude set by the adiabatic approximation discussed in § 4.6.1 (Witte & Savonije 1999; Fuller & Lai 2012b; Burkart et al. 2013).

In this paper we are interested in understanding the phenomenon of resonance locking, in which the orbital and spin frequencies vary in concert so as to hold the Doppler-shifted tidal forcing frequency $k\Omega_{\rm orb} - m\Omega_{\rm spin}$ constant (Witte & Savonije 1999). Resonance locking is analogous to the phenomenon of capture into resonance in planetary dynamics (Goldreich 1965; Goldreich & Peale 1968); we provide a comparison in § 4.10. Resonance locks can accelerate the course of tidal evolution, as we will show in § 4.8. Moreover, recent studies (Fuller & Lai 2012b; Burkart et al. 2012) have proposed that resonance locks may have been observed in the *Kepler* system KOI-54 (Welsh et al. 2011), although this has been contested by O'Leary & Burkart (2013).

Since resonance locking involves a changing spin frequency, clearly it cannot occur under approximation (1) noted above. The domain of validity of approximation (2) is given in § 4.6.1

(see also Burkart et al. 2013). In this paper, we drop both of the above assumptions and examine resonance locks accounting for a dynamically evolving mode amplitude coupled to both the orbital and spin evolution. Our aim is to investigate the general dynamical properties of resonance locking, rather than to focus on a specific astrophysical application. Our key questions concern determining when resonance locks can occur and under what conditions they are dynamically stable.

This paper is structured as follows. We first describe the essential idea behind resonance locking in § 4.2, and enumerate the approximations we make in order to limit the complexity of our analysis in § 4.3. We then develop evolution equations for a single stellar or planetary eigenmode in § 4.4.1, and determine the implied backreaction upon the binary orbit and stellar or planetary spin in § 4.4.2. We establish the existence and assess the stability of fixed points in the evolution equations associated with resonance locking in § 4.5. We describe two analytic approximations that a mode's amplitude follows in certain limits in § 4.6.1, and then present example numerical integrations of resonance locks in § 4.6.2. In § 4.6.3 we discuss the possibility of chaos during resonance locking. We numerically and analytically determine the parameter regimes that lead to resonance locking in § 4.7, and show that resonance locks can accelerate tidal evolution in § 4.8. We apply our results to two example astrophysical systems—inspiraling compact object binaries and eccentric stellar binaries—in § 4.9. We then conclude in § 4.10.

4.2 Basic idea

We first explain the essential mechanism behind resonance locking by considering the example situation of a circular white dwarf binary inspiraling due to the emission of gravitational waves (Burkart et al. 2013). Focusing on a particular white dwarf, and shifting to a frame of reference corotating with the white dwarf's spin, the tidal forcing frequency is $\sigma = m(\Omega_{\rm orb} - \Omega_{\rm spin})$, where m is the azimuthal spherical harmonic index and we temporarily assume $\Omega_{\rm orb} \gg \Omega_{\rm spin}$. Due to the influence of gravitational waves, $\Omega_{\rm orb}$ gradually increases, and thus so does σ. As such, σ sweeps towards resonance with the nearest normal mode, and this mode gains energy as it becomes increasingly resonant (Rathore et al. 2005).

Along with energy, however, comes angular momentum (for $m \neq 0$ modes). As the mode then damps, this angular momentum is transferred to the background rotation, increasing $\Omega_{\rm spin}$ and consequently decreasing σ. Thus if the mode is capable of achieving a sufficient amplitude, fixed points can exist where σ (but not $\Omega_{\rm orb}$ or $\Omega_{\rm spin}$ individually) is held *constant* by tidal synchronization balancing orbital decay by gravitational waves, as illustrated in Figure 4.1. This is the idea behind a tidal resonance lock.

The properties of such fixed points corresponding to resonance locking clearly depend on the rate of externally driven orbital evolution and the strength of tidal coupling to the mode in question. Furthermore, the mode's damping rate influences both its maximum achievable amplitude as well as the rate at which it dissipates angular momentum into the background rotation profile. Lastly, since resonance locking involves a balance between orbital and spin evolution, the ratio of the associated moments of inertia—roughly $MR^2/\mu a^2$ where μ is the reduced mass and a is the semi-major axis—also plays a key role. We will see in subsequent sections that dimensionless pa-

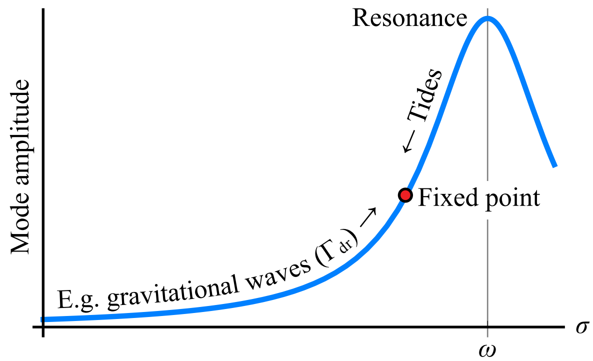

Figure 4.1: Diagram illustrating the basic mechanism behind tidal resonance locking. Forcing frequency drift caused for example by gravitational waves causes the tidal forcing frequency σ to advance towards the right. The influence of tidal synchronization, on the other hand, becomes stronger as resonance approaches, and tends to push the forcing frequency to the left. This creates a fixed point on the resonant mode's Lorentzian amplitude profile. (The mirror image of this situation is also possible.)

rameters corresponding to these four quantities will entirely determine the dynamics of resonance locking.

The ideas we have presented here in the context of inspiraling white dwarf binaries carry over to the more general scenario where some generic physical process causing the forcing frequency σ or the eigenmode frequency ω to evolve in one direction—e.g., gravitational waves, magnetic braking, the equilibrium tide, stellar evolution, etc.—is balanced by the resonant tidal interaction with a planetary or stellar normal mode causing σ to evolve in the opposite direction.

4.3 Essential assumptions

Throughout this work, we invoke the following principal assumptions.

1. As discussed in § 4.1, we assume that the dynamical tide is composed of standing waves, and thus that linear dissipation (provided e.g. by radiative diffusion) is not strong enough to prohibit wave reflection.

2. As a mode's amplitude grows, nonlinear processes can become important. For example, gravity waves break and catastrophically dissipate when their vertical displacement becomes comparable to their vertical wavelength (Lindzen 1966). Moreover, global parametric resonances can occur at smaller amplitudes, which transfer energy to a pair of daughter modes (e.g. Weinberg et al. 2012).

   We completely neglect nonlinear hydrodynamical phenomena in this work. The applicability of this approximation depends on the particular star or planet's structure and the binary's parameters. For example, although Witte & Savonije (2002) considered resonance locking in solar-type binaries, Goodman & Dickson (1998) showed that the lack of a convective core in such stars allows geometric focusing to progressively amplify the local amplitude of an inward-propagating gravity wave to the point where wave breaking occurs over a wide range of binary parameters (see also Barker & Ogilvie 2010). This precludes the establishment of the standing waves required for a resonance lock.

3. We assume that the star or planet in question rotates as a rigid body, even though tidal torques are typically applied to the background rotation profile in a thin spherical shell where mode damping is strongest (Goldreich & Nicholson 1989a). We thus rely upon the action of an efficient angular momentum transport process. Whether such a process is available strongly depends on the application in question; see e.g. Burkart et al. (2013) and accompanying references. Without solid-body rotation, critical layers can develop where angular momentum is deposited, which would provide rapid, local dissipation and hence violate assumption (i).

4. We take the overall strength of a mode's tidal forcing to be constant, and account for orbital evolution only insofar as it affects the forcing *frequency*. We thus ignore, for example, that the magnitude of the tidal force depends on the binary's semi-major axis, which necessarily must evolve if $\Omega_{\rm orb}$ is to change. We determine when this assumption is valid in § 4.5.1; it would never be appropriate for long-timescale simulations that follow the evolution of many resonance locks (which are not performed in this paper).

5. Lastly, to simplify our analysis, we only consider binary systems where the spin and orbital angular momenta are aligned. Generalization to spin-orbit-misaligned systems is straightforward (Lai 2012), and ultimately only introduces a Wigner $\mathcal{D}$-matrix element into our definition of the tidal coupling coefficient U in § 4.4.1.

4.4 Formalism

4.4.1 Mode amplitude evolution

We work in a frame of reference corotating with the spin of the body in question, where the rotation axis lies along the $\hat{z}$ direction. Following Schenk et al. (2002), we invoke a phase space eigenmode decomposition of the tidal response (Dyson & Schutz 1979). The standard stellar mode inner product for arbitary vector fields $\boldsymbol{\eta}$ and $\boldsymbol{\eta}'$ is

$$\langle \boldsymbol{\eta}, \boldsymbol{\eta}' \rangle = \int \boldsymbol{\eta}^* \cdot \boldsymbol{\eta}' \rho \, dV, \tag{4.1}$$

and the anti-Hermitian Coriolis force operator is defined by $B\boldsymbol{\eta} = 2\Omega_{\rm spin}\hat{z} \times \boldsymbol{\eta}$.

We consider the resonant interaction between a time-varying tidal potential evaluated on a Keplerian orbit and a single linear mode of our expansion. The mode has spherical harmonic indices l and m, and has complex amplitude q. The differential equation describing the mode's linear evolution is (Schenk et al. 2002)

$$\dot{q}+(i\omega+\gamma)q=\frac{i\omega}{\varepsilon}\left\langle\boldsymbol{\xi},\mathbf{a}_{\rm tide}\right\rangle, \tag{4.2}$$

where ω is the mode's eigenfrequency, γ is its damping rate, $\boldsymbol{\xi}$ is its Lagrangian displacement vector,

$$\varepsilon=2\omega^2\langle\boldsymbol{\xi},\boldsymbol{\xi}\rangle+\omega\langle\boldsymbol{\xi},iB\boldsymbol{\xi}\rangle \tag{4.3}$$

is a normalization factor (equal to the mode energy at unit amplitude), and $\mathbf{a}_{\rm tide}$ is the time-dependent tidal acceleration vector. We assume $\gamma \ll \omega$ and, without loss of generality, we take $\omega > 0$.

Allowing for an arbitrary eccentricity, the projection of the tidal acceleration onto the mode $\langle\boldsymbol{\xi},\mathbf{a}_{\rm tide}\rangle$ is proportional to

$$\left(\frac{a}{D}\right)^{l+1}e^{-im\left(f-\psi_{\rm spin}\right)},$$

where D is the binary separation, a is the semi-major axis, f is the true anomaly, and

$$\begin{pmatrix}\psi_{\rm orb}\\ \psi_{\rm spin}\end{pmatrix}=\int\begin{pmatrix}\Omega_{\rm orb}\\ \Omega_{\rm spin}\end{pmatrix}dt. \tag{4.4}$$

Assuming that changes in the orbital frequency and eccentricity occur on timescales much longer than an orbital period, we can expand the dependence on D and f in a Fourier series:

$$\left(\frac{a}{D}\right)^{l+1}e^{-im\left(f-\psi_{\rm spin}\right)}\approx\sum_k X_{lm}^k e^{-i\left(k\psi_{\rm orb}-m\psi_{\rm spin}\right)}, \tag{4.5}$$

where $X_{lm}^k(e)$ is a Hansen coefficient (Appendix C.2), with $X_{lm}^k(e=0)=\delta_m^k$ for circular orbits. Since we are concerned with resonant mode-tide interaction, we henceforth consider only a single harmonic component of this expansion. The phase associated with this component is $\psi = k\psi_{\rm orb}-m\psi_{\rm spin}$.

Our mode amplitude equation from (4.2) then becomes

$$\dot{q}+(i\omega+\gamma)q=i\omega U e^{-i\psi}. \tag{4.6}$$

The dimensionless mode-tide coupling strength associated with our harmonic component is

$$U=\left(\frac{M'}{M}\right)\left(\frac{R}{a}\right)^{l+1}\left(\frac{E_*}{\varepsilon}\right)\mathcal{I}_{lm}X_{lm}^k W_{lm}, \tag{4.7}$$

where M' is the companion mass,

$$\mathcal{I}_{lm}=\frac{1}{MR^l}\left\langle\boldsymbol{\xi},\boldsymbol{\nabla}\left(r^lY_{lm}\right)\right\rangle \tag{4.8}$$

is the mode's linear tidal overlap integral (Press & Teukolsky 1977),

$$W_{lm} = \frac{4\pi}{2l+1} Y_{lm}^{*}\left(\frac{\pi}{2}, 0\right) \tag{4.9}$$

is an order-unity angular coupling coefficient, and $E_* = GM^2/R$ is the gravitational energy scale. We also define the tidal forcing frequency to be $\sigma = \dot{\psi} = k\Omega_{\rm orb} - m\Omega_{\rm spin}$, and take $\sigma > 0$ without loss of generality. We are free to choose the sign of σ since we are considering a complex conjugate mode pair—one member of the pair is resonant with σ while the other is resonant with $-\sigma$. Because m can possess either sign, both prograde and retrograde modes are allowed for $\sigma > 0$. Since we are considering resonant interaction, our assumption is $\sigma \approx \omega$.

4.4.2 Forcing frequency evolution

We will first obtain the time derivative of the stellar or planetary spin frequency implied by equation (4.6). The canonical angular momentum associated with the mode together with its complex conjugate is given by (Appendix C.3)

$$J_{\rm mode} = \frac{m\varepsilon}{\omega}|q|^2. \tag{4.10}$$

Differentiating with respect to time and substituting equation (4.6), we find

$$\dot{J}_{\rm mode} = -2\gamma J_{\rm mode} + 2m\varepsilon U \mathrm{Im}\left[q e^{i\psi}\right]. \tag{4.11}$$

The first term in equation (4.11) results from damping, and is imparted to the stellar or planetary spin (Goldreich & Nicholson 1989b).[1] We thus set

$$\dot{J}_{\rm spin} = 2\gamma J_{\rm mode}, \tag{4.12}$$

meaning that

$$\dot{\Omega}_{\rm spin} = \frac{2\gamma J_{\rm mode}}{I_*} + \alpha_{\rm spin}, \tag{4.13}$$

where I_* is the planet or star's moment of inertia, and we have incorporated an additional term $\alpha_{\rm spin}$ to account for processes that can change $\Omega_{\rm spin}$ other than interaction with the mode in question—e.g., the equilibrium tide, magnetic braking, etc. We take $\alpha_{\rm spin}$ to be constant.

The rate at which the orbital energy changes is given by (Weinberg et al. 2012)

$$\dot{E}_{\rm orb} = -2k\Omega_{\rm orb}\varepsilon U \mathrm{Im}\left[q e^{i\psi}\right]. \tag{4.14}$$

[1] It can be shown that the second term in equation (4.11) is exactly the angular momentum transfer rate from the orbit; see e.g. Weinberg et al. (2012). This justifies attributing the first term to changes in the spin.

We can convert equation (4.14) into an expression for $\dot{\Omega}_{\rm orb}$ using

$$\frac{\dot{\Omega}_{\rm orb}}{\Omega_{\rm orb}} = -3\,\frac{\dot{E}_{\rm orb}}{\mu a^2 \Omega_{\rm orb}^2}, \tag{4.15}$$

which yields

$$\dot{\Omega}_{\rm orb} = \left(\frac{3k}{\mu a^2}\right) 2\varepsilon U \,\mathrm{Im}\left[q e^{i\psi}\right] + \alpha_{\rm orb}, \tag{4.16}$$

where we have again included an extra term $\alpha_{\rm orb}$ to account for e.g. orbital decay by gravitational waves.

It is useful to combine equations (4.13) & (4.16) to determine the time derivative of $\delta\omega = \omega - \sigma$, which can be expressed as

$$\frac{\delta\dot{\omega}}{\omega} = -\Gamma_{\rm dr} + \Gamma_{\rm tide}\left(\frac{\gamma |q|^2}{\omega U^2} - r\,\mathrm{Im}\left[\frac{q e^{i\psi}}{U}\right]\right). \tag{4.17}$$

Here we have combined both α parameters from earlier into the "drift" rate

$$\Gamma_{\rm dr} = \frac{k\alpha_{\rm orb} - m(1-C)\alpha_{\rm spin}}{\omega} - \frac{\partial \ln\omega}{\partial t}, \tag{4.18}$$

where

$$C = -\frac{1}{m}\frac{\partial\omega}{\partial\Omega_{\rm spin}} \tag{4.19}$$

allows for a rotationally dependent corotating-frame eigenmode frequency and $\partial\omega/\partial t$ accounts for changes in the eigenmode frequency due to progressive modifications of the background hydrostatic profile from e.g. stellar evolution.[2] The tidal backreaction rate is

$$\Gamma_{\rm tide} = \frac{2m^2 U^2 (1-C)\varepsilon}{I_* \omega}, \tag{4.20}$$

and parameterizes the strength of tidal coupling to the mode in question; it is related to the rate at which the mode can synchronize the star or planet at nonresonant amplitudes ($|q| \sim |U|$). Lastly, the moment of inertia ratio is

$$r = \frac{k^2}{m^2}\frac{3I_*}{(1-C)\mu a^2}. \tag{4.21}$$

We assume that both $\Gamma_{\rm tide}$ and r are positive throughout this work, but allow $\Gamma_{\rm dr}$ to possess either sign.

[2]Tidal heating could contribute to the $|q|^2$ term in equation (4.17), due to heat deposited by the mode in question affecting the background star or planet; we neglect this for simplicity.

4.5 Resonance lock fixed points

4.5.1 Existence of fixed points

We first remove the overall oscillatory time dependence of q by changing variables to $Q = qe^{i\psi}/U$, so that equation (4.6) becomes

$$\dot{Q} + \left(i\delta\omega + \gamma + \frac{\dot{U}}{U}\right) Q = i\omega, \tag{4.22}$$

where again $\delta\omega = \omega - \sigma$. For simplicity, we now assume that γ is much larger than terms contributing to $\dot{U}/U$, such as $\dot{a}/a$ and $\dot{e}/e$, so that equation (4.22) becomes

$$\dot{Q} + (i\delta\omega + \gamma)\, Q = i\omega; \tag{4.23}$$

as we will see in § 4.8, this essentially amounts to assuming $\gamma \gg |\Gamma_{\rm dr}|$. Equation (4.17) becomes

$$\frac{\dot{\delta\omega}}{\omega} = -\Gamma_{\rm dr} + \Gamma_{\rm tide}\left(\frac{\gamma}{\omega}|Q|^2 - r\,{\rm Im}[Q]\right). \tag{4.24}$$

Having thus eliminated direct dependence on the phase ψ, our two dynamical variables are now Q and $\delta\omega$. Since Q is complex, we have a third-order differential system.

Resonance locking corresponds to a fixed point in the evolution equations. We thus set time derivatives to zero in equation (4.23) to derive

$$Q_{\rm f} = \frac{\omega}{\delta\omega_{\rm f} - i\gamma}, \tag{4.25}$$

and hence

$$\begin{bmatrix} {\rm Re}(Q_{\rm f}) \\ {\rm Im}(Q_{\rm f}) \end{bmatrix} = \frac{\omega}{\delta\omega_{\rm f}^2 + \gamma^2} \times \begin{bmatrix} \delta\omega_{\rm f} \\ \gamma \end{bmatrix}. \tag{4.26}$$

Similarly, setting $\dot{\delta\omega} = 0$ in equation (4.24) and using the fact that $(\gamma/\omega)|Q_{\rm f}|^2 = {\rm Im}(Q_{\rm f})$, we have

$$\Gamma_{\rm dr} = (1 - r)\,\Gamma_{\rm tide}\,{\rm Im}(Q_{\rm f}). \tag{4.27}$$

We can use equations (4.26) & (4.27) to derive

$$\delta\omega_{\rm f}^2 = \frac{\omega\gamma\Gamma_{\rm tide}(1 - r)}{\Gamma_{\rm dr}} - \gamma^2. \tag{4.28}$$

So far we have not determined the sign of $\delta\omega_{\rm f}$, and indeed there is one fixed point for each sign; however, we will show in § 4.5.2 that one is always unstable.

These fixed points exists if equations (4.26) & (4.27) can be solved for $Q_{\rm f}$ and $\sigma_{\rm f}$, which is possible if (assuming $\Gamma_{\rm tide} > 0$)

$$\frac{\gamma}{\omega\Gamma_{\rm tide}} < \frac{1-r}{\Gamma_{\rm dr}}; \tag{4.29}$$

this in particular requires

$$(1-r)\Gamma_{\rm dr} > 0. \tag{4.30}$$

If $\Gamma_{\rm dr} > 0$, then equation (4.30) reduces to

$$|k| < |m| \left(\frac{(1-C)\mu a^2}{3I_*}\right)^{1/2}. \tag{4.31}$$

As a result, Fuller & Lai (2012b) referred to the quantity on the right-hand side of equation (4.31) as the "critical" harmonic.

The existence of the fixed points also relies on the "weak-tide" limit, which we define to be $|\delta\omega_{\rm f}| < \Delta\omega/2$, where $\Delta\omega$ is the eigenmode frequency spacing near the mode in question. This means that the fixed point must lie within the eigenmode's domain of influence, so that the contribution of other eigenmode resonances can be legitimately neglected. If this is not the case, then resonance locking is not possible.

For example, if $\Gamma_{\rm dr}$ is very small, equation (4.27) requires a commensurately small value of Q. However, this could be impossible to achieve in practice, since it would require a very large value of the detuning $\delta\omega$, allowing the possibility for a neighboring mode to come into resonance. The actual outcome in such a situation is that the tidal interaction would dominate the dynamics, and the drift processes contributing to $\Gamma_{\rm dr}$ would be irrelevant—i.e., the "strong-tide" limit.

A necessary condition for the weak-tide limit, and thus for a resonance lock to be able to occur, is $|\delta\omega_{\rm f}| \ll \omega$, which evaluates to

$$\frac{|\Gamma_{\rm dr}|}{\gamma} \gg \frac{\Gamma_{\rm tide}|1-r|}{\omega}. \tag{4.32}$$

We will use this as a convenient, although very liberal, proxy for the real requirement of $|\delta\omega_{\rm f}| < \Delta\omega/2$, so as to avoid handling the additional parameter $\Delta\omega$. Calculations of dynamical tidal evolution that use the adiabatic approximation (§ 4.6.1) with many modes—e.g. Witte & Savonije (1999); Fuller & Lai (2012b)—already naturally account for the true requirement.

4.5.2 Fixed point stability

Linearization

We will now perform a linear stability analysis about each fixed point. First, note that the presence of the nonanalytic functions $|\cdot|$ and $\mathrm{Im}(\cdot)$ in equation (4.24) necessitates treating the real and imaginary parts of Q separately. Thus let

$$\boldsymbol{\zeta} = \begin{bmatrix}\mathrm{Re}(Q) & \mathrm{Im}(Q) & (\sigma-\omega)/\omega\end{bmatrix}^T,$$

and

$$\frac{d\boldsymbol{\zeta}}{dt} = \mathbf{f}(\boldsymbol{\zeta}),$$

where $\mathbf{f}$ represents equations (4.23) & (4.24) and satisfies $\nabla \cdot \mathbf{f} = -2\gamma$. We can then derive a time-evolution equation for $\boldsymbol{\delta\zeta} = \boldsymbol{\zeta} - \boldsymbol{\zeta}_{\rm f}$ by invoking results from § 4.5.1.

Proceeding, to linear order we have

$$\frac{d}{dt}\boldsymbol{\delta\zeta} = A\boldsymbol{\delta\zeta} + o(\boldsymbol{\delta\zeta}), \tag{4.33}$$

where

$$A = \mathcal{D}\mathbf{f}(\boldsymbol{\zeta}_{\rm f}) = \begin{bmatrix} -\gamma & \delta\omega_{\rm f} & A_{1,3} \\ -\delta\omega_{\rm f} & -\gamma & A_{2,3} \\ A_{3,1} & A_{3,2} & 0 \end{bmatrix}, \tag{4.34}$$

$$A_{1,3} = -\frac{\omega\beta}{\Gamma_{\rm tide}} \qquad A_{2,3} = \frac{\omega\beta\delta\omega_{\rm f}}{\gamma\Gamma_{\rm tide}} \tag{4.35}$$

$$A_{3,1} = -\frac{2\beta\delta\omega_{\rm f}}{\omega} \qquad A_{3,2} = r\Gamma_{\rm tide} - \frac{2\beta\gamma}{\omega}, \tag{4.36}$$

and $\beta = \Gamma_{\rm dr}/(1-r)$.

Eigenvalues

We assume in this section that equation (4.29) is satisfied, so that the resonance locking fixed point formally exists, and that equation (4.32) is also satisfied, so that we are in the weak-tide limit and the fixed point physically exists. The characteristic polynomial P for the eigenvalues λ of A is

$$P(\lambda) = \lambda^3 + 2\gamma\lambda^2 + P_1\lambda + P_0, \tag{4.37}$$

where

$$P_1 = \frac{\omega\gamma\Gamma_{\rm tide}}{\beta} - \frac{r\omega\beta\delta\omega_{\rm f}}{\gamma} \qquad P_0 = 2\omega\Gamma_{\rm dr}\delta\omega_{\rm f}. \tag{4.38}$$

A fixed point is asymptotically stable if all eigenvalues satisfy $\mathrm{Re}(\lambda) < 0$. A standard theorem then states that, for this to occur, it is necessary (but not sufficient) that all of the coefficients of λ^i ($i \geq 0$) in equation (4.37) possess the same sign. We thus must have that $P_{1,0} > 0$.

First, we see that

$$+1 = \mathrm{sign}(P_0) = \mathrm{sign}(\Gamma_{\rm dr})\mathrm{sign}(\delta\omega_{\rm f}). \tag{4.39}$$

Since equations (4.26) & (4.27) admit two solutions, corresponding to $\delta\omega_{\rm f} = \pm|\delta\omega_{\rm f}|$, the criterion that $P_0 > 0$ simply allows us to select the solution that could potentially be stable. Henceforth we will focus on the solution that satisfies equation (4.39), which we refer to as the "lagging" fixed point; similarly, the "leading" fixed point is the one that fails to satisfy equation (4.39).

Equation (4.39) permits the following intuitive interpretation: the forcing frequency σ is "pushed" towards an eigenfrequency in the direction specified by the sign of $\Gamma_{\rm dr}$, but the approaching eigenmode "pushes" σ in the opposite direction, and resonance locking occurs when these "forces" cancel out (§ 4.2). In particular, if $\Gamma_{\rm dr} > 0$, $\sigma_{\rm f}$ should be smaller than ω, meaning $\delta\omega_{\rm f} = \omega - \sigma_{\rm f} > 0$, consistent with equation (4.39).

It remains to analyze P_1 and to ascertain when it is also positive. Moreover, since positivity of the characteristic polynomial's coefficients is only a necessary condition for stability, we must then further examine the Hurwitz matrix associated with P to establish when its leading principal minors are also positive (e.g. Gradshteyn & Ryzhik 2007). We perform this analysis in Appendix C.1 in the limit of $\gamma \ll |\delta\omega_{\rm f}|$; the result is that the lagging fixed point is stable if and only if

$$\Gamma_{\rm dr} < 0 \quad \text{or} \quad 0 < \frac{\Gamma_{\rm dr}}{\gamma} < (1-r)\left(\frac{\Gamma_{\rm tide}}{\omega}\right)^{1/3} \tag{4.40}$$

(subject to the assumptions we have made thus far). In particular, the lagging fixed point is thus always stable for $r > 1$ per equation (4.30).

Figure 4.2 shows the stability region of the lagging fixed point as a function of the damping rate γ and the frequency drift rate $\Gamma_{\rm dr}$ for two example values of the backreaction rate $\Gamma_{\rm tide}$ and the moment of inertia ratio r. Stability was determined by numerically solving for the eigenvalues λ using equation (4.37), and is indicated by green shading, while instability is white; regions where the fixed point does not exist are shaded dark gray. Equations (4.29), (4.32), & (4.40), which are displayed as blue dashed, black dotted, and magenta dot-dashed lines, closely correspond to the green region's boundaries. The values used in the top panel were chosen based on our white dwarf binary application in § 4.9.1. In the bottom panel we have $r > 1$, which by equation (4.30) implies $\Gamma_{\rm dr} < 0$.

The instability boundary defined by equation (4.40) is in fact a supercritical Hopf bifurcation (Wiggins 2003), corresponding to the loss of stability of a complex conjugate eigenvalue pair. Past the bifurcation, inside the unstable region of parameter space, this unstable complex conjugate pair splits into two unstable real eigenvalues, as shown in Figure 4.3. In other words, the fixed point switches from being an unstable spiral to an unstable node. Determining the parameter space manifold on which this splitting occurs will be useful in § 4.7.2; we can accomplish this by setting the discriminant of equation (4.37) to zero (thus requiring a repeated root), yielding

$$0 = 36\gamma P_1 P_0 - 32\gamma^3 P_0 + 4\gamma^2 P_1^2 - 4P_1^3 - 27P_0^2. \tag{4.41}$$

Although this equation cannot be solved analytically, we can nonetheless determine the asymptotic dependence of $\Gamma_{\rm dr}$ on γ in the limit $\gamma \to 0$. Newton's polygon for equation (4.41) shows that this asymptotic dependence is linear: $\Gamma_{\rm dr} = A\gamma$. Substituting this into equation (4.41), setting $\gamma = 0$, and solving for A, we have that the lagging fixed point is a spiral if

$$\Gamma_{\rm dr} < \gamma\left(\frac{1-r}{r^{2/3}}\right)\left(\frac{\Gamma_{\rm tide}}{\omega}\right)^{1/3}. \tag{4.42}$$

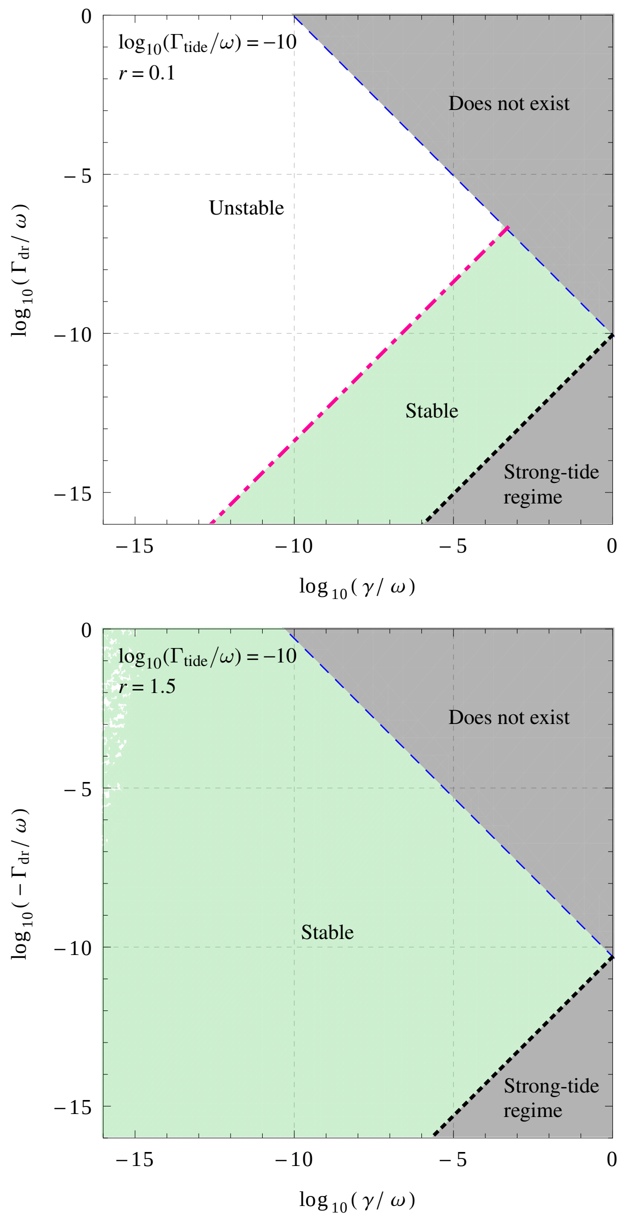

Figure 4.2: Resonance locking fixed point stability analysis. Regions where the fixed point is asymptotically stable are shaded green, while unstable regions are white, and regions where the fixed point does not exist are dark gray. We determined the stability regions by numerically evaluating the eigenvalues λ_i of the matrix A determined by linearizing the equations of motion about the fixed point (equation 4.34) and enforcing $\mathrm{Re}(\lambda_i) < 0$ together with equation (4.32). The analytic results in equations (4.29), (4.32), & (4.40) are displayed as blue dashed, black dotted, and magenta dot-dashed lines. The lower-right gray triangle in both panels corresponds to where the weak-tide limit is certainly violated, and thus the fixed point does not physically exist; see § 4.5.1. In the bottom panel we have $r > 1$, which by equation (4.30) implies $\Gamma_{\rm dr} < 0$.

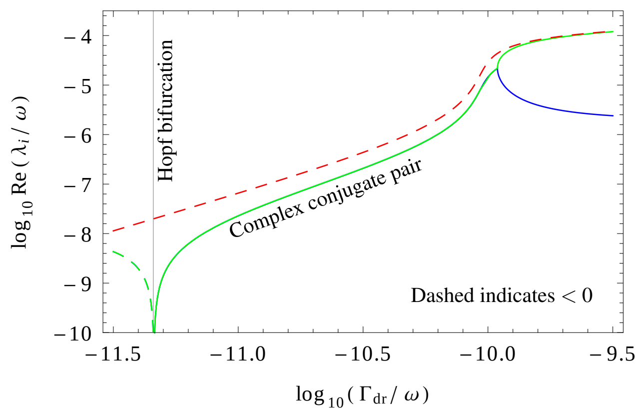

Figure 4.3: Real parts of the lagging fixed point's three eigenvalues as functions of $\Gamma_{\rm dr}$ for $\gamma/\omega = 10^{-8}$, $\Gamma_{\rm tide}/\omega = 10^{-10}$, and $r = 0.01$ (see the left middle panel of Figure 4.10). A complex conjugate pair exists for $\Gamma_{\rm dr}/\omega \lesssim 10^{-10}$ (equation 4.42), which loses stability at $\Gamma_{\rm dr}/\omega \approx 10^{-11.3}$ in a Hopf bifurcation (equation 4.40).

4.6 Trajectories

Here we will show several examples of trajectories that can be produced by our dynamical equations from § 4.5.1. First, however, in § 4.6.1 we will discuss two different analytic approximations that the trajectories follow in certain limits.

4.6.1 Analytic approximations

Adiabatic approximation

In this paper, we define the adiabatic approximation to be the situation where the mode amplitude can instantaneously adjust to a changing forcing frequency, and thus we can set the $\dot{Q}$ term in equation (4.23) to zero and assume σ is constant. Equation (4.23) can then be solved exactly:

$$Q_{\rm ad} = \frac{\omega}{\delta\omega - i\gamma}. \tag{4.43}$$

This approximation, also referred to as the Lorentzian approximation due to the form of equation (4.43), is frequently employed in the literature.

The domain of validity of the adiabatic approximation can be determined by comparing the maximum possible mode growth rate to the growth rate implied by equation (4.43); when the latter exceeds the former, the adiabatic approximation is no longer valid. We can determine the maximum rate at which a mode amplitude Q can grow by providing a perfect resonance to equation (4.23), i.e., by setting $\sigma = \omega$. Dropping the damping term and setting $\dot{\sigma} = 0$, the particular solution is

$$Q(t) = i\omega t, \tag{4.44}$$

which implies that $|\dot{Q}|_{\rm max} = \omega$. Next, in order to estimate the time derivative of $Q_{\rm ad}$, we take

$\dot{\sigma} \approx \Gamma_{\rm dr}\omega$, which gives us

$$|\dot{Q}_{\rm ad}| \approx |\Gamma_{\rm dr}| \left(\frac{\omega^2}{\delta\omega^2 + \gamma^2} \right). \tag{4.45}$$

We then equate $|\dot{Q}_{\rm ad}|$ and $|\dot{Q}|_{\rm max}$ and solve for $\delta\omega$, finding

$$\delta\omega_{\rm ad}^2 \approx |\Gamma_{\rm dr}|\omega - \gamma^2; \tag{4.46}$$

if $|\Gamma_{\rm dr}|\omega < \gamma^2$, then the adiabatic approximation is always valid.

No-backreaction approximation

Although directly solving equations (4.23) & (4.24) outside the adiabatic limit requires numerical integration, we can nonetheless produce an approximate analytic expression for $Q(t)$ in the limit that backreaction of the mode on the tidal forcing frequency σ is unimportant (Reisenegger & Goldreich 1994; Rathore et al. 2005). This approximation subsumes the adiabatic approximation, but is also more complicated.

Since we are already assuming that the mode damping rate is weak enough for the resonance locking fixed point to exist (equation 4.29), we can simply take $\gamma \to 0$. Subject to this simplification, we can solve equation (4.6), yielding

$$q(t) \approx i\omega U e^{-i\omega t} \int_{t_0}^{t} e^{i\omega t - i\psi} dt, \tag{4.47}$$

with $t_0 \ll -(\omega\Gamma_{\rm dr})^{-1/2}$. If we then approximate ψ as

$$\psi \approx \psi_0 + \omega t + \omega\Gamma_{\rm dr} t^2/2,$$

where we have set resonance to occur (i.e. $\dot{\psi} = \omega$) at $t = 0$, then equation (4.47) becomes a closed-form solution to the equations of motion.

Since the integral in equation (4.47) approaches a constant for $t \gg (\omega\Gamma_{\rm dr})^{-1/2}$, and since we wish to estimate the maximum value of $|Q|$, we can simply extend the domain of integration to $(-\infty, +\infty)$, yielding (using e.g. the method of stationary phase)

$$q(t) \approx -(1-i)U \sqrt{\frac{\pi\omega}{\Gamma_{\rm dr}}} e^{-i\omega t - i\psi_0} \tag{4.48}$$

for $t \gg (\omega\Gamma_{\rm dr})^{-1/2}$. We thus find that

$$|Q|_{\rm max} \approx \sqrt{\frac{2\pi\omega}{|\Gamma_{\rm dr}|}}. \tag{4.49}$$

We plot this maximal value of $|Q|$ in the middle panels of Figures 4.4 – 4.7 as a dash-dotted black line.

4.6.2 Numerical results

Figures 4.4 – 4.7 show full numerical solutions to equations (4.23) & (4.24) for several different choices of our four parameters γ, $\Gamma_{\rm dr}$, $\Gamma_{\rm tide}$, and r. In each case, the mode amplitude is initialized to the adiabatic approximation in the regime where it should be valid (§ 4.6.1).

First, Figure 4.4 gives a simple example of resonance locking into a stable fixed point. Next, we hold $\Gamma_{\rm tide}$, γ, and r constant, but increase $\Gamma_{\rm dr}$ by a factor of ~ 10, thus making σ sweep towards resonance more quickly. In this case the fixed point is no longer stable, since equation (4.40) is no longer satisfied, and Figure 4.5 shows the limit cycle resonance lock that then occurs. The system passes through resonance in between the two unstable fixed points, and then oscillates back and forth through resonance. This oscillation pumps the mode amplitude up as the system is repelled by the fixed points. Eventually, the oscillation ceases and the mode's angular momentum discharges into rotation causing the system to travel back away from resonance and decay back onto the adiabatic approximation. The cycle then begins again. This limit cycle is in fact precisely the stable periodic orbit generated by the supercritical Hopf bifurcation (§ 4.5.2).

Figure 4.6 shows the resulting evolution again holding all parameters constant except for $\Gamma_{\rm dr}$, which we increase by another factor of ~ 10. The resonance locking fixed point is now sufficiently unstable that it suppresses the mode amplitude's growth and prevents resonance locking from occurring. Near resonance the mode amplitude still grows appreciably, but after the lock fails to hold, damping causes the mode amplitude to decay exponentially. We have found the linear character of the lagging fixed point to be the principal distinguishing factor between a limit cycle occurring and a failed resonance capture due to fixed point suppression. Specifically, we find that if the lagging fixed point is an unstable node, meaning all its eigenvalues are real (Figure 4.3), then it acts to suppress the mode amplitude and leads to a failed capture. If instead the lagging fixed point is an unstable spiral, meaning its eigenvalues contain an unstable complex conjugate pair (§ 4.5.2), then it is able to "pump" a trajectory to high amplitude and allow the formation of a limit cycle. This distinction, which is valid within a factor of ~ 3 in $\Gamma_{\rm dr}$, will be critical in § 4.7.2.

4.6.3 Chaos

Lastly, Figure 4.7 shows a chaotic trajectory. This situation is very similar to the limit cycle evolution shown in Figure 4.5, in that the resonance locking fixed point is unstable but $\Gamma_{\rm dr}$ is not so large that resonance locking doesn't occur altogether; the essential difference is that the mode amplitude profile resulting from the adiabatic approximation (dashed line) is capped by damping not far above the fixed points, unlike in Figure 4.5 where it ascends much higher. This corresponds to the fact that the choice of parameters for Figure 4.7 lies close (logarithmically speaking) to the bifurcation manifold in parameter space where equation (4.29) ceases to be satisfied and the fixed points no longer exist. This appears to be a key ingredient for chaos, as we will explain below, which is why we have changed γ to a larger value than that used in Figures 4.4 – 4.6 (so that equation 4.29 is closer to not being satisfied).

Since the fixed points are so close to the peak of the adiabatic profile, the pumping process that occurs due to repulsion from the fixed points cannot allow the mode to acquire a very large

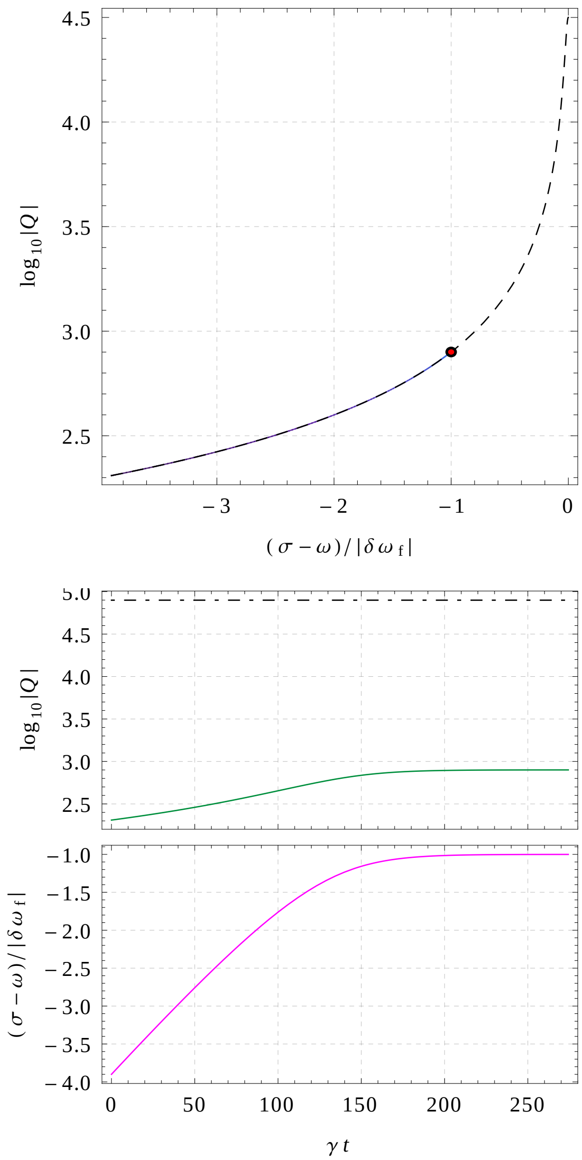

Figure 4.4: Numerical integration of mode and orbital evolution equations for the case of resonance locking into a stable fixed point. Parameters used were $\Gamma_{dr}/\omega = 10^{-9}$, $\gamma/\omega = 10^{-4.5}$, $\Gamma_{tide}/\omega = 10^{-10}$, and $r = 0.5$. The adiabatic approximation is shown in the top panel as a dashed black line (§ 4.6.1), while the actual system trajectory is purple. The red circle shows the lagging fixed point (§ 4.5). Individual timeseries for the mode amplitude Q and the forcing frequency σ are shown in the bottom two panels. The dash-dotted black line in the mode amplitude panel shows equation (4.49), which gives the maximum amplitude attainable under the no-backreaction approximation (§ 4.6.1). The lagging fixed point's eigenvalues are $\lambda/\omega \in \{(-0.031 \pm 1.2\,i)\times 10^{-3},\, -1.6\times 10^{-6}\}$.

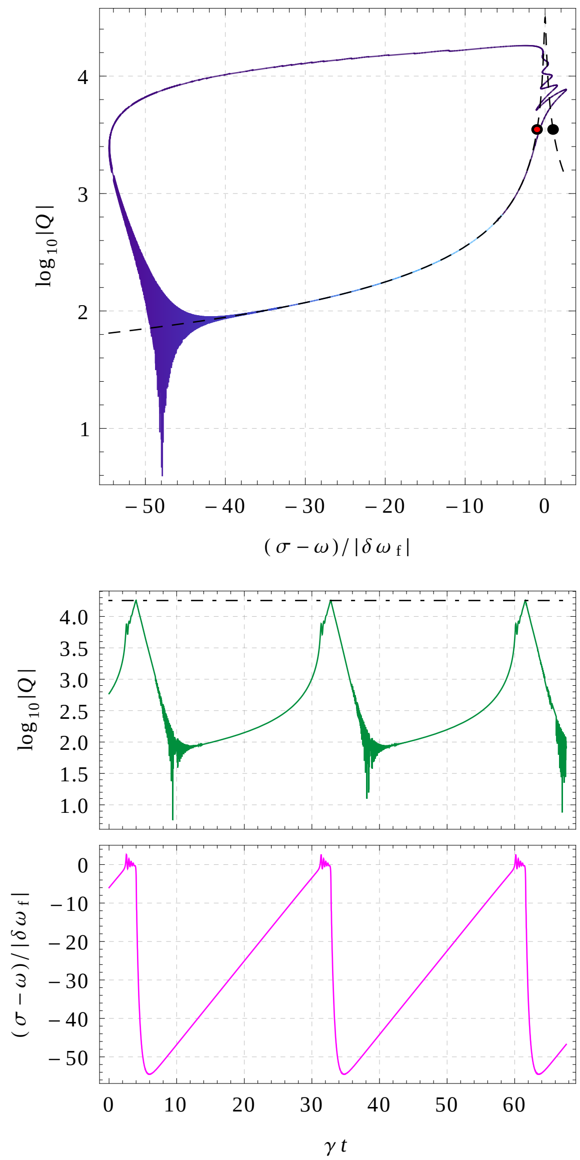

Figure 4.5: Resonance lock limit cycle for a case in which the fixed points exist (red and black circles) but are linearly unstable. Parameters used were $\Gamma_{\rm dr}/\omega = 10^{-7.7}$, $\gamma/\omega = 10^{-4.5}$, $\Gamma_{\rm tide}/\omega = 10^{-10}$, and $r = 0.5$. Conventions used are the same as in Figure 4.4. Color shows time, ranging from purple at $t = 0$ to light blue. The red & black circles show the lagging and leading fixed points, respectively (§ 4.5). System sweeps through resonance without initially being captured. However, the system then oscillates through resonance several times, pumping up the mode's amplitude. Eventually, the oscillation ceases and the mode's angular momentum discharges into rotation causing the system to travel back away from resonance and start over. The lagging fixed point's eigenvalues are $\lambda/\omega \in \{-3.9 \times 10^{-4},\ (1.6 \pm 0.49\,i) \times 10^{-4}\}$.

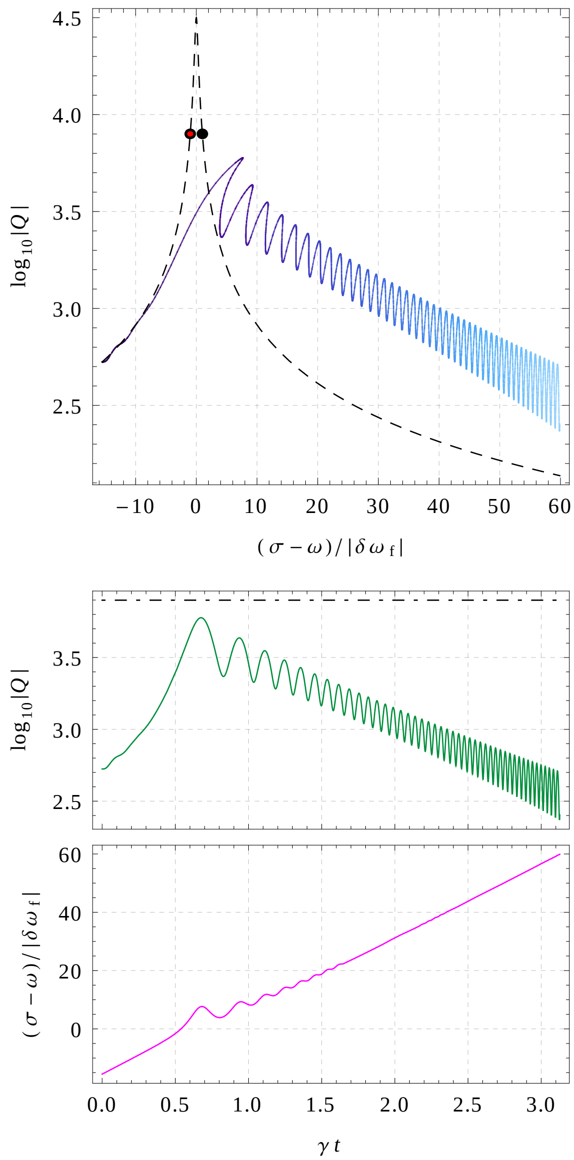

Figure 4.6: Failed resonance lock. Parameters used were $\Gamma_{\rm dr}/\omega = 10^{-7}$, $\gamma/\omega = 10^{-4.5}$, $\Gamma_{\rm tide}/\omega = 10^{-10}$, and $r = 0.5$. Conventions used are the same as in Figure 4.4. Color shows time, ranging from purple at $t = 0$ to light blue. The unstable, repulsive fixed points (red and black circles) suppress the maximum attainable mode amplitude below the dash-dotted black line in the second panel, which shows the maximum amplitude that would be achieved without backreaction (§ 4.6.1). This suppression is severe enough to prevent resonance locking from occurring. The lagging fixed point's eigenvalues are $\lambda/\omega \in \{-6.7 \times 10^{-4},\ 5.4 \times 10^{-4},\ 6.8 \times 10^{-5}\}$.

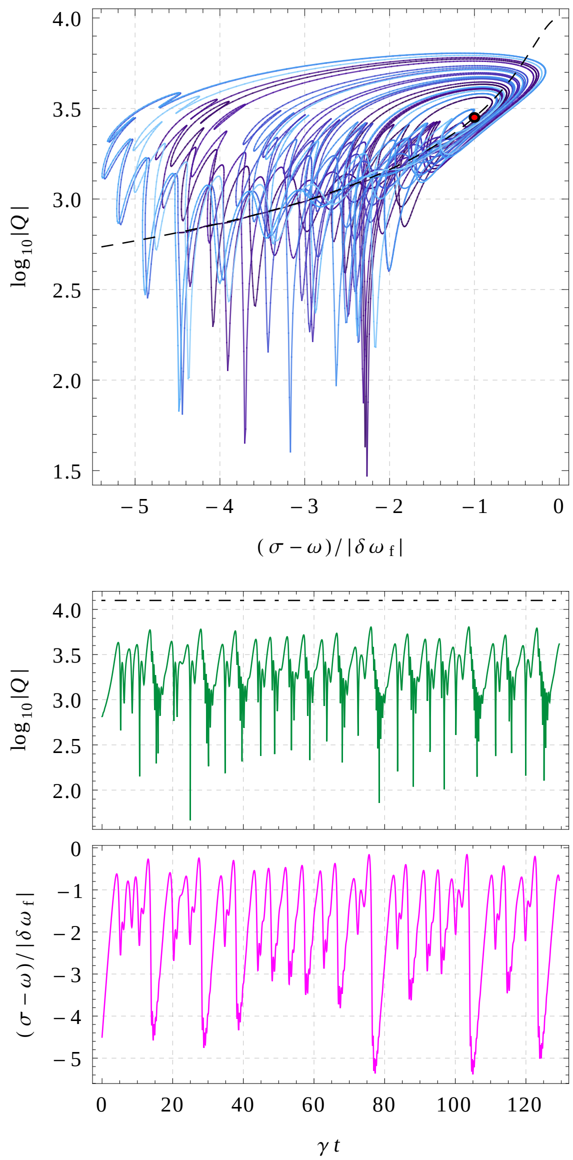

Figure 4.7: Chaotic resonance lock around an unstable fixed point (red circle). Parameters used were $\Gamma_{\rm dr}/\omega = 10^{-7.4}$, $\gamma/\omega = 10^{-4}$, $\Gamma_{\rm tide}/\omega = 10^{-10}$, and $r = 0.5$. Conventions used are the same as in Figure 4.4. Color shows time, ranging from purple at $t = 0$ to light blue. This situation is similar to that depicted in Figure 4.5, but in this case backreaction is so significant that the system never fully returns to the adiabatic approximation once deviating from it near the fixed point. Chaotic orbits are instead executed around the fixed point. The lagging fixed point's eigenvalues are $\lambda/\omega \in \{(0.98 \pm 2.4\,i) \times 10^{-4},\ -4.0 \times 10^{-4}\}$.

amplitude. As a result, when the mode's angular momentum eventually drains into the background spin, the system does not retreat back from resonance very far, and has little time to decay back onto the adiabatic approximation before resonance is reached again. The initial condition upon entering resonance is consequently somewhat different each cycle, leading to the potential for chaos.

We show a three-dimensional projection of the orbit from Figure 4.7 in Figure 4.8. The lagging fixed point is shown by a small red sphere, while its unstable plane corresponding to eigenvalues $\lambda/\omega = (0.98 \pm 2.4\, i) \times 10^{-4}$ is also displayed.

We now present numerical evidence that the path depicted in Figure 4.8 follows a strange attractor. We emphasize that our evidence is not rigorous. A strange attractor of a dynamical system, also known as an attracting chaotic invariant set, is a set that (Wiggins 2003):

1. is compact,
2. is invariant under the dynamical equations,
3. is attracting,
4. has sensitive dependence on initial conditions, and
5. is topologically transitive.

Figure 4.8 appears to begin to trace out a bounded, attracting, invariant set, which we denote Λ; this addresses conditions (i) – (iii). In Figure 4.9, we estimate the largest Lyapunov exponent of the trajectory in Figure 4.8 to be $6 \times 10^{-5}\omega$. Since this is positive, trajectories that begin together deviate exponentially as time passes. This then points toward condition (iv) being satisfied. Lastly, since color indicates time in Figure 4.8, the fact that dark purple (early times) is tightly and randomly interwound with light blue (late times) leads us to believe that condition (v) is likely also satisfied. Again, we have presented only suggestive evidence; further study is required to fully address the presence of a strange attractor.

In addition, we note that our preliminary investigations show that the chaos present results from the Hopf orbit undergoing a period-doubling cascade, and is similar in several ways to the Rössler attractor (Rössler 1976). This requires further study.

4.7 Achieving resonance locks

4.7.1 Numerical results

In order to ascertain the conditions that lead to resonance locks, we performed sample integrations of equations (4.23) & (4.24) numerically. We initialized each integration with

$$\delta\omega_0 = 10 \times \max\left(\delta\omega_{\rm f}, \delta\omega_{\rm ad}, \gamma\right)$$

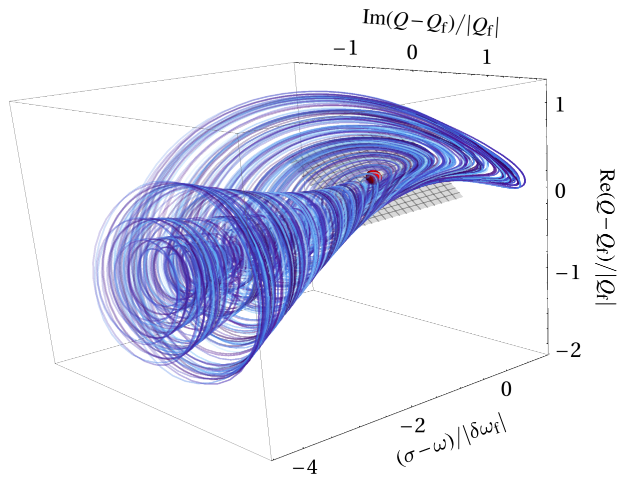

Figure 4.8: Three-dimensional projection of the integration from Figure 4.7. Time is indicated by color, ranging from dark purple at early times to light blue. The unstable plane corresponding to eigenvalues $(0.98 \pm 2.4\,i) \times 10^{-4}$ is shown, centered on the fixed point (red sphere). Each cycle, the system begins near the fixed point, but is then ejected along the unstable manifold. Nonlinear terms cause the system to decay back onto the adiabatic solution; this motion comprises the spiral structure on the left. The adiabatic solution then transports the system near to the fixed point, and the cycle begins again with perturbed initial conditions.

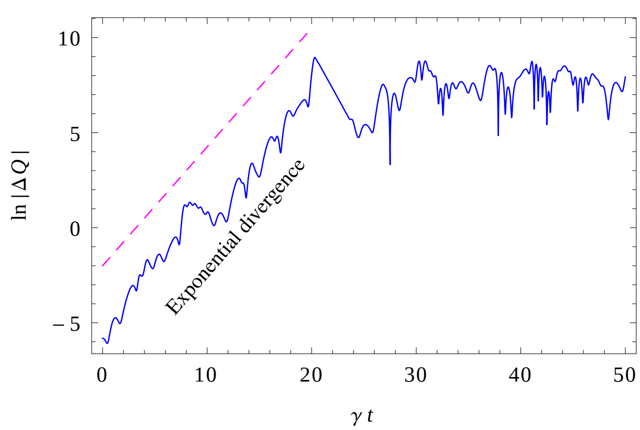

Figure 4.9: Estimation of largest Lyapunov exponent for the chaotic trajectory in Figures 4.7 & 4.8. We initialized two numerical integrations of our dynamical equations on the adiabatic solution (§ 4.6.1) with slightly perturbed initial detuning frequencies: $\delta\omega_0 = 0.95\delta\omega_\mathrm{f}$ and $0.950001\delta\omega_\mathrm{f}$. The blue curve shows the norm of the difference between the resulting values of the reduced mode amplitude Q as a function of time. The trajectories initially deviate exponentially, demonstrating chaos, with a rough functional form of $e^{t/\tau}$ for $\tau \approx 2 \times 10^4/\omega$ (dashed magenta line). We thus estimate the largest Lyapunov exponent (Wiggins 2003) for the trajectories to be $\approx 1/\tau \approx 6 \times 10^{-5}\omega > 0$, which is close to the damping rate of $\gamma = 10^{-4}\omega$.

and Q_0 set by the adiabatic approximation from equation (4.43). We then performed each integration until $t_1 = 2\delta\omega_0/\omega\Gamma_{\rm dr}$. We determined that a resonance lock occurred if, assuming $r < 1$,

$$\frac{\min\delta\omega}{\delta\omega_0} > -0.5,$$

where $\min\delta\omega$ is the minimum value of $\delta\omega$ attained over the final 10% of integration.[3] A similar formula was used for $r > 1$, but accounting for the fact that resonance is then approached from the left (in terms of $\delta\omega$; see § 4.5.1). Note that these conditions account for stable, limit cycle, and chaotic forms of resonance locking (§ 4.6.2).

Figure 4.10 shows our results. Light blue regions indicate that a resonance lock did occur, while white indicates the reverse, and dark gray indicates that the fixed point does not exist (§ 4.5.1). The green lines are the analytic formula from equation (4.54) below for the boundary between successful and failed resonance locking. The thin purple lines are the equivalent condition for resonance locks to occur when $r > 1$, from equation (4.53). Both analytic approximations, which we will develop in the next section, show good agreement with numerical results.

4.7.2 Analytic approximations

We now seek to obtain an analytical understanding of our numerical results in Figure 4.10. We will thus attempt to assemble a set of analytic approximations to determine what values of our four parameters γ, $\Gamma_{\rm dr}$, $\Gamma_{\rm tide}$, and r (§ 4.4) lead to resonance locks, and what values do not. We define resonance locking in this context to be any behavior such that σ does not increase without bound as $t \to \infty$; this definition comprises locking into a stable fixed point (Figure 4.4), limit cycles about an unstable fixed point (Figure 4.5), and chaotic behavior like in Figure 4.7, but does not include the behavior seen e.g. in Figure 4.6.

We see by inspecting equations (4.25) & (4.43) that the adiabatic solution exactly passes through the resonance locking fixed point. As a result, a sufficient condition for a resonance lock to be achieved is $|\delta\omega_{\rm f}| > |\delta\omega_{\rm ad}|$, which evaluates to

$$\Gamma_{\rm dr}^2 \lesssim (1-r)|\Gamma_{\rm tide}|\gamma, \tag{4.50}$$

together with fixed point stability (§ 4.5.2; equation 4.40). However, this is a very conservative estimate of the resonance locking regime. To develop a set of necessary and sufficient criteria for resonance locks, recall that the time derivative of $\delta\omega$ is given by (equation 4.24)

$$\dot{\delta\omega}/\omega = -\Gamma_{\rm dr} + \Gamma_{\rm tide}(g_1 - rg_2), \tag{4.51}$$

where g_1 and g_2 are

$$g_1 = \frac{\gamma}{\omega}|Q|^2 \qquad g_2 = \mathrm{Im}[Q]. \tag{4.52}$$

First, assume $r \gg 1$. By equation (4.30) we see that $\Gamma_{\rm dr} < 0$ and thus that the system approaches

[3] Numerous other potential resonance lock criteria exist; however, we have found this to be the most reliable.

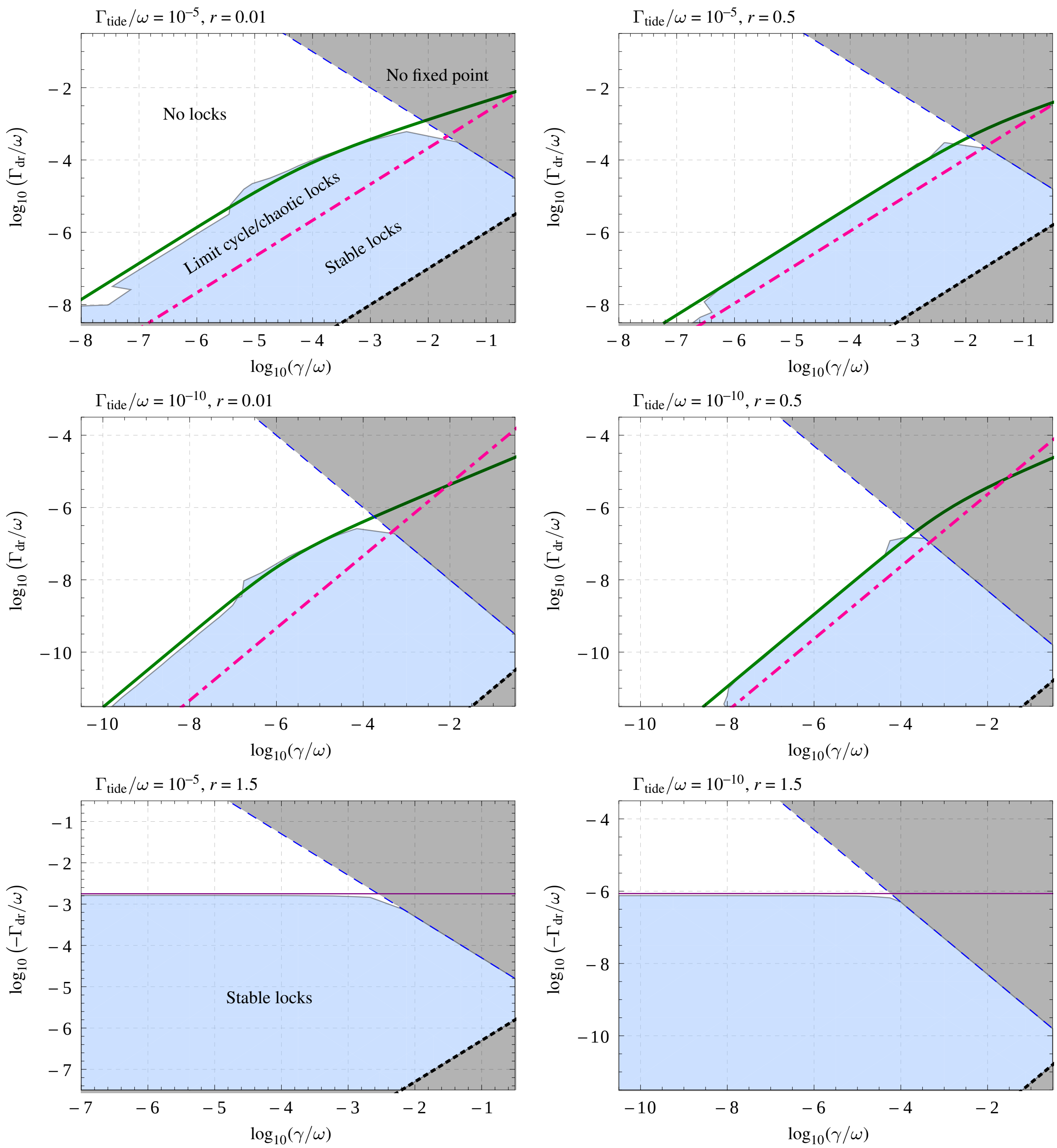

Figure 4.10: Resonance lock regimes based on numerical solution of mode, spin, and orbit evolution equations from § 4.5.1. Light blue shading indicates that resonance locking occurs (including stable fixed point locks, limit cycles, and chaotic locks, as in Figures 4.4, 4.5, & 4.7), while white indicates the reverse (as in Figure 4.6). Above each dashed blue line, the resonance locking fixed point does not exist (§ 4.5.1; equation 4.29). The green and purple lines correspond to our analytic formulae for the resonance locking regime (§ 4.7.2; equations 4.54 & 4.53 respectively). The dash-dotted magenta line indicates the upper boundary of the domain of stability of the resonance lock fixed point (§ 4.5.2; equation 4.40), while the dotted black line shows where the weak-tide limit is certainly violated (§ 4.5.1; equation 4.32). Limit cycles and chaotic orbits (as in Figures 4.5 & 4.7) preferentially occur in the regions between the green and magenta lines (where the fixed point is unstable but locks still occur).

resonance from the left (in terms of $\delta\omega$; note that in Figures 4.4 – 4.7 the abscissa is $\sigma-\omega = -\delta\omega$). Since the lagging fixed point is always stable in this situation (§ 4.5.2), we simply need the resonance passage to provide sufficient amplitude to reach the fixed point in order for a stable resonance lock to take hold. Invoking the no-backreaction approximation results from § 4.6.1 to substitute a maximum value of Im[Q] into equation (4.51), dropping g_1, and setting $\dot{\delta\omega} \sim 0$ leads to the following condition for resonance locking:

$$-\frac{\Gamma_{\rm dr}}{\Gamma_{\rm tide}} > 3r\sqrt{-\frac{\pi\omega}{\Gamma_{\rm dr}}}. \qquad (r \gg 1) \tag{4.53}$$

Although our analysis is strictly valid only for r much larger than unity, we find it to work well even for $r \gtrsim 1$, as can be seen in the bottom row of Figure 4.10 (where $r = 1.5$). We have inserted an additional factor of 3 on the right-hand side of equation (4.53) to match our numerical results.

Next, assume $r \ll 1$. By equation (4.30) this means $\Gamma_{\rm dr} > 0$, so the system approaches the resonance locking fixed point from the right (in terms of $\delta\omega$). Here, however, the fixed point is *not* always stable, as we found in § 4.5.2. In § 4.6.2, we argued that resonance locks in the form of limit cycles or chaotic trajectories could occur when the fixed point was an unstable spiral (with a complex conjugate pair of eigenvalues), but that resonance capture failed when the fixed point was an unstable node (with all real eigenvalues); this was true within a factor of ~ 3 in terms of the value of $\Gamma_{\rm dr}$. Thus a necessary condition for resonance locks (to within a factor of ~ 3) is equation (4.42), which specifies where the fixed point is a spiral. Next, we drop g_2 and again substitute the no-backreaction approximation results from § 4.6.1 to find that resonance passage can deliver a system to the resonance locking fixed point if

$$\frac{\gamma}{\Gamma_{\rm dr}} > \frac{\Gamma_{\rm dr}}{2\pi\Gamma_{\rm tide}}.$$

Augmented with equation (4.42), this approximately becomes the following condition for resonance locking:

$$\frac{\gamma}{\Gamma_{\rm dr}} > \frac{\Gamma_{\rm dr}}{6\pi\Gamma_{\rm tide}} + \frac{1}{3}\left(\frac{r^{2/3}}{1-r}\right)\left(\frac{\omega}{\Gamma_{\rm tide}}\right)^{1/3}. \qquad (r \ll 1) \tag{4.54}$$

Similar to our formula for $r > 1$, our analysis is valid only for r very close to zero; however, we again find it to work well even for $r \lesssim 1$, as can be seen in the right panels of the top two rows of Figure 4.10 (where $r = 0.5$). We have inserted an additional factor of $1/3$ on the right-hand side of equation (4.54) to match our numerical results.

4.8 Tidal evolution during resonance locks

4.8.1 Accelerating tidal evolution

Here we generalize the energetic arguments made in Burkart et al. (2013) to estimate the orbital and spin evolution during a resonance lock. During a lock, the reduced mode amplitude

Q is roughly given by its value at the fixed point, i.e., equation (4.27); note, however, that this approximation is very crude for limit cycles and chaotic orbits (e.g. Figures 4.5 & 4.7) since in those cases the real and imaginary parts of Q have a more complicated dependence on time. Using equations (4.16) & (4.27) together with our definitions of $\Gamma_{\rm dr}$, $\Gamma_{\rm tide}$, and r from equations (4.18) – (4.21), we can derive

$$\dot{\Omega}_{\rm orb} = \left(\frac{1}{1-r}\right)\left[\alpha_{\rm orb} - \frac{r}{k}\left(m\alpha_{\rm spin} + \frac{\partial\omega}{\partial t}\right)\right], \tag{4.55}$$

where again $\alpha_{\rm orb}$ and $\alpha_{\rm spin}$ represent the contributions to $\dot{\Omega}_{\rm orb}$ and $\dot{\Omega}_{\rm spin}$ from slowly varying processes other than resonant interaction with the normal mode in question (see equations 4.13 & 4.16). This can be converted into an energy transfer rate by equation (4.15). Performing a similar derivation for the spin frequency, we have

$$\dot{\Omega}_{\rm spin} = \left(\frac{r}{1-r}\right)\left[-\alpha_{\rm spin} + \frac{1}{rm}\left(k\alpha_{\rm orb} - \frac{\partial\omega}{\partial t}\right)\right], \tag{4.56}$$

Examining equations (4.55) & (4.56), we see that a resonance lock acts to *accelerate* the orbital and spin evolution given by the nonresonant processes contributing to $\alpha_{\rm orb}$ and $\alpha_{\rm spin}$, which are due e.g. to gravitational wave orbital decay, the equilibrium tide, etc. Moreover, since the time derivative of the eccentricity is simply a linear combination of $\dot{\Omega}_{\rm orb}$ and $\dot{\Omega}_{\rm spin}$ (Witte & Savonije 1999), resonance locking also accelerates circularization. The degree of acceleration depends on how close the moment of inertia ratio r is to unity; we estimate under what conditions $r \sim 1$ in § 4.8.2. This acceleration of tidal evolution is what led Witte & Savonije (2002) to conclude that resonance locks solve the solar-binary problem (Meibom et al. 2006), although they neglected essential nonlinear effects that obviate their results (see § 4.3).

The presence of $\alpha_{\rm spin}$ in the evolution equation for $\dot{\Omega}_{\rm orb}$ (and $\alpha_{\rm orb}$ in the equation for $\dot{\Omega}_{\rm spin}$) implies that a resonance lock efficiently couples orbital and spin evolution together, as well as to stellar evolution through the rate of change of the eigenfrequency $\partial\omega/\partial t$. For example, if gravitational waves in an inspiraling white dwarf binary cause orbital decay, a resonance lock will cause tidal synchronization to occur on a gravitational wave timescale (§ 4.9.1). Similarly, resonance locking can cause stellar spindown by magnetic braking or eigenfrequency evolution due to tidal heating to backreact on the binary orbit.

4.8.2 Conditions for rapid tidal evolution

Here we estimate the "typical" value of r (defined in equation 4.21) expected to occur in a given binary, so as to assess whether resonance locks significantly accelerate tidal evolution (§ 4.8.1). First, consider a binary in a circular, spin-aligned orbit. For the lowest-order $l = 2$ spherical harmonic of the tidal potential, only one temporal Fourier component of the tidal forcing exists: $k = m = 2$ (§ 4.4.1). With only a single forcing component, it is thus generically unlikely to find $r \sim 1$. The exception is when considering a star whose companion's mass is $\ll M$, in which case r may be ~ 1 even for a circular orbit.

For an eccentric orbit, however, there is significant power at many harmonics k of the orbital frequency. In this case, a resonance lock persists until it is disrupted when another mode, driven by a different Fourier component, also comes into resonance and upsets the balance of spin and orbital evolution theretofore enforcing $\delta\dot{\omega} = 0$. Whether the existing resonance lock can withstand a second resonance passage depends on how "robust" it is; we can estimate the degree of "robustness" using the maximum amplitude achieved under the no-backreaction approximation from § 4.6.1:[4]

$$|q|_{\max} = |U|\sqrt{\frac{2\pi\omega}{|\Gamma_{\mathrm{dr}}|}}. \tag{4.57}$$

If we equate $\omega \approx k\Omega_{\mathrm{orb}}$, having taken $|m\Omega_{\mathrm{spin}}| \ll |k\Omega_{\mathrm{orb}}|$ for simplicity, then $|q|_{\max}$ depends on the harmonic index k as

$$|q|_{\max} \underset{\sim}{\propto} k^b X^k_{lm}, \tag{4.58}$$

where X is a Hansen coefficient and $b > 0$ is a constant that accounts for power law dependences on the tidal overlap integral and other mode-dependent quantities entering into equation (4.57) (§ 4.4.1). Using our scaling derived in Appendix C.2, equation (4.58) becomes

$$|q|_{\max} \underset{\sim}{\propto} k^{b-1/2}\exp\left[-kg(e)\right], \tag{4.59}$$

where the full form of $g(e) \approx (1-e^2)^{3/2}/3$ is given in equation (C.10).

The longest-lived resonance locks in an eccentric binary will be those with the largest values of $|q|_{\max}$. Thus we can estimate the "typical" value of r by finding the value of k that maximizes $|q|_{\max}$. This is

$$\mathrm{argmax}_k |q|_{\max} \approx \frac{b-1/2}{g(e)}. \tag{4.60}$$

In order to produce a simple order-of-magnitude estimate, we take $b-1/2 \sim 1$ to find that the most robust resonance locks will have $r \sim 1$, and thus significantly increase the rate of tidal evolution, if[5]

$$1-e^2 \sim \left(10\frac{I_*}{\mu a^2}\right)^{1/3}. \tag{4.61}$$

When this condition is not satisfied, then either the longest-lived resonance locks will not provide much acceleration of tidal evolution, or there will be no long-lived locks at all.

4.9 Astrophysical applications

In §§ 4.9.1 & 4.9.2, we determine where tidal resonance locks may be able to occur by applying the criteria we have developed—equations (4.29) & (4.54)—to inspiraling compact object binaries

[4]Our results are insensitive to the expression by which a resonance lock's "robustness" is quantified, so long as it is proportional to U.

[5]Note that whether $r > 1$ or $r < 1$ is determined by the sign of Γ_{dr}, which is independent of our estimates here; see § 4.5.1.

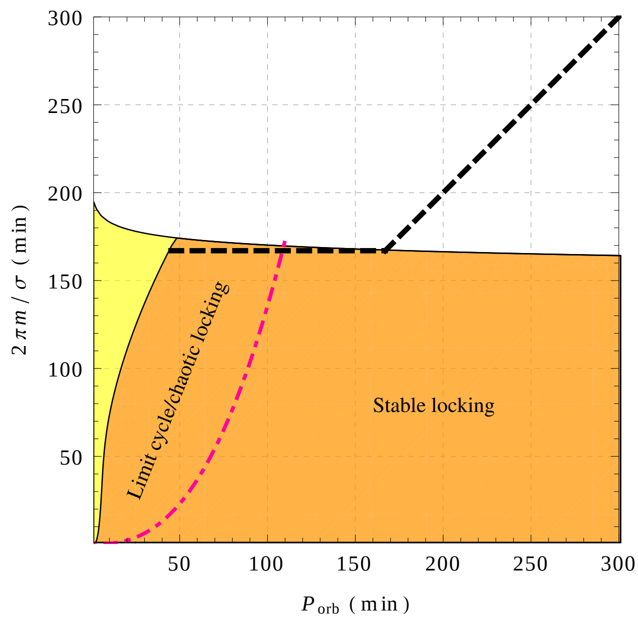

Figure 4.11: Resonance locking regimes for a fiducial white dwarf binary. Yellow shading indicates that the resonance locking fixed points exists (equation 4.29), but that resonance locks are nonetheless not possible. Orange shading indicates the complete resonance locking regime, derived from our numerical results in § 4.7.1 (equation 4.54). The black dashed line shows a schematic system trajectory, assuming the initial spin is negligible. The dot-dashed magenta line shows where the lagging fixed point becomes unstable (equation 4.40).

and eccentric stellar binaries.

4.9.1 Inspiraling compact object binaries

We consider the case of a circular, spin-orbit-aligned binary consisting of either two white dwarfs or two neutron stars. The equivalent of the drift rate Γ_{dr} in this case is

$$\Gamma_{dr} = \frac{m\Omega_{orb}}{\omega t_{gw}}, \tag{4.62}$$

where t_{gw} is the gravitational wave orbital decay time given by (Peters 1964)

$$t_{gw} = \omega_*^{-1} \frac{5}{96} \frac{\left(1+M'/M\right)^{1/3}}{M'/M} \beta_*^{-5} \left(\frac{\omega_*}{\Omega_{orb}}\right)^{8/3}. \tag{4.63}$$

Here $\omega_*^2 = GM/R^3$ is the dynamical frequency and $\beta_*^2 = GM/Rc^2$ is the ratio of the escape velocity to the speed of light. We consider only the $l = |m| = 2$ component of the tidal response.

For a fiducial double-white dwarf binary, we use the $0.6M_\odot$, $T_{eff} = 5,500$ K carbon/oxygen white dwarf model described in Burkart et al. (2013), with a radius of $R = 0.013R_\odot$, and a moment of inertia of $I_* = 0.18MR^2$. For the damping rate γ and tidal overlap integral $\mathcal{I}$, we use the following scaling relations listed in Table 3 of Burkart et al. (2013):

$$\mathcal{I} \sim 27 \times \left(\frac{\sigma}{\omega_*}\right)^{3.69}$$
$$\gamma \sim 2.9 \times 10^{-14}\omega_* \times \left(\frac{\sigma}{\omega_*}\right)^{-1.88},$$

where our mode normalization convention is $E_* = \varepsilon$ and we are neglecting rotational modifications of the stellar eigenmodes (in other words, setting the Coriolis force operator B from § 4.4.1 to zero).

For a fiducial double-neutron star binary, we use the $M = 1.4M_\odot$, $R = 12$ km cold neutron star model employed in Weinberg et al. (2013), which assumed the Skyrme-Lyon equation of state (Chabanat et al. 1998; Steiner & Watts 2009). We assume that $I_* = 0.18MR^2$, as with our white dwarf model. Weinberg et al. (2013) give the following scaling relations for $l = 2$ g-modes:

$$\mathcal{I} \sim 0.3 \times \left(\frac{\sigma}{\omega_*}\right)^{2}$$
$$\gamma \sim 4 \times 10^{-8} \times \left(\frac{\sigma}{\omega_*}\right)^{-2} T_8^{-2}\ \mathrm{Hz},$$

where T_8 is the core temperature in units of 10^8 K.

Figure 4.11 shows our result for the white dwarf case. The yellow region shows where the resonance locking fixed point exists (equation 4.29) but where resonance locks are nonetheless not possible according to our numerical and analytic results in § 4.7. The orange region shows the complete resonance locking regime derived from our numerical results (equation 4.54). The dashed black line in the top panel is a simple, schematic system trajectory for a double-white dwarf binary. The system begins in the upper right with a long orbital period and a small rotation rate. Once orbital decay causes the system to reach the orange region, a resonance lock occurs and the forcing frequency σ is held approximately constant. This was already demonstrated in Burkart et al. (2013) using the adiabatic approximation (§ 4.6.1), which is valid for determining when the resonance locking fixed points exist.

Eventually, however, the system exits the orange region. At this point resonance locking is no longer possible because of the short gravitational wave inspiral time. This novel prediction comes from our analysis in this work.[6] Note that this prediction neglects nonlinear hydrodynamical phenomena (§ 4.3): in reality the wave amplitude eventually becomes large enough to cause wave breaking, as shown in Burkart et al. (2013); Fuller & Lai (2012a). This may be a more stringent

[6] Burkart et al. (2013) did assess where the adiabatic approximation (which was inaccurately referred to as the "secular approximation") became invalid; however, this is an incomplete consideration that fails to account for fixed point instability, limit cycles, etc.

constraint on the existence of resonance locks in many close white dwarf binaries.

In the neutron star case, the gravitational wave time is much shorter than for white dwarf binaries at comparable values of R/a, since neutron stars are much more relativistic objects. Resonance passage thus happens very quickly, which prevents modes from reaching amplitudes large enough to allow locking. As a result, resonance locks are never possible, even though the resonance locking fixed point exists for $P_{\rm orb} \lesssim 50$ ms.

To get a sense of the degree to which equation (4.54) fails to be satisfied for neutron star binaries, we first compute the following quantities with $\Omega_{\rm spin} = 0$:

$$\frac{\gamma}{\omega} = 10^{-7} T_8^{-2} \left(\frac{P_{\rm orb}}{50 \text{ ms}} \right)^3 \qquad \frac{\Gamma_{\rm dr}}{\omega} = 6 \times 10^{-5} \left(\frac{P_{\rm orb}}{50 \text{ ms}} \right)^{-5/3}$$

$$\frac{\Gamma_{\rm tide}}{\omega} = 10^{-11} \left(\frac{P_{\rm orb}}{50 \text{ ms}} \right)^{-6} \qquad r = 0.002 \left(\frac{P_{\rm orb}}{50 \text{ ms}} \right)^{-4/3}.$$

We thus set $r \approx 0$. Substituting the remaining values into equation (4.54) and simplifying, we have

$$10\, T_8^2 < 10^{-7} \left(\frac{P_{\rm orb}}{50 \text{ ms}} \right)^{1/3}. \tag{4.64}$$

This shows that resonance locking fails to occur by ~ 8 orders of magnitude at a wide range of orbital periods. The conclusion that resonance locks cannot occur in neutron star binaries is thus very robust.

4.9.2 Eccentric binaries

In this section we estimate whether resonance locking can occur in eccentric stellar binaries (Witte & Savonije 1999). For a fiducial system, we take parameters consistent with KOI-54 (Welsh et al. 2011), where it has been recently suggested that one or more of the observed tidally excited pulsations may be the signatures of resonance locks (Fuller & Lai 2012b; Burkart et al. 2012; see however O'Leary & Burkart 2013). This system consists of two similar A stars with $M \approx 2.3 M_\odot$, $R \approx 2.2 R_\odot$, and $T_{\rm eff} \approx 8{,}500$ K. The binary's orbital parameters are $e = 0.83$ and $P_{\rm orb} = 43$ days. Burkart et al. (2012) estimated damping rates for such stars to be

$$\gamma \sim 0.1 \left(\frac{\omega}{\omega_*} \right)^{-4} \text{Myr}^{-1}. \tag{4.65}$$

For overlap integrals $\mathcal{I}$, we take the following scaling derived for A stars from Burkart et al. (2012):

$$\mathcal{I} \sim 10^{-5} \left(\frac{\omega}{\omega_*} \right)^{11/6}. \tag{4.66}$$

The drift rate $\Gamma_{\rm dr}$ in this case comes from the equilibrium tide's influence on each star's spin and on the overall orbital frequency. We account only for the equilibrium tide's effect on the orbital frequency for simplicity. Parameterizing the equilibrium tide's energy transfer rate by its quality factor $\mathcal{Q}_{\rm eq}$, so that (Goldreich & Soter 1966)

$$|\dot{E}_{\rm eq}| \sim \frac{E_{\rm tide}\Omega_{\rm orb}}{\mathcal{Q}_{\rm eq}}, \tag{4.67}$$

we have the approximate formula

$$\Gamma_{\rm dr} \sim \frac{E_{\rm tide}}{\mathcal{Q}_{\rm eq}\mu a^2}\frac{k}{\omega}, \tag{4.68}$$

where the energy contained in the equilibrium tide is roughly $E_{\rm tide} \sim \lambda(M'/M)^2(R/a)^6E_*$, and the constant λ (related to the apsidal motion constant) is $\sim 3\times10^{-3}$ for an A star.

Witte & Savonije (1999) invoked the adiabatic approximation (§ 4.6.1) to show that resonance locking could occur in various fiducial eccentric binary systems; Burkart et al. (2012) performed a similar analysis for KOI-54. However, as we have established in this work, this only means that the resonance locking fixed point exists, and not necessarily that resonance locking actually occurs. For the latter, we need to apply our criterion from equation (4.54).

As in § 4.9.1, we proceed to compute the values of our four parameters that affect the possibility of resonance locks in the current situation. We fix r, but assume $0 \ll r < 1$. We also assume that the star is nonrotating. We then find[7]

$$\begin{aligned}\frac{\gamma}{\omega} &= 10^{-11}\left(\frac{P_{\rm orb}}{40\ \rm day}\right)^{5/3}\\ \frac{\Gamma_{\rm dr}}{\omega} &= 3\times10^{-21}\left(\frac{P_{\rm orb}}{40\ \rm day}\right)^{-4}\left(\frac{\mathcal{Q}_{\rm eq}}{10^8}\right)^{-1}\\ \frac{\Gamma_{\rm tide}}{\omega} &= 6\times10^{-18}\left(\frac{P_{\rm orb}}{40\ \rm day}\right)^{-4.6}.\end{aligned}$$

Substituting into equation (4.54), noting that the first term on the right-hand side of equation (4.54) is much smaller than the second in this case (unlike in § 4.9.1), we find that locks are present if

$$1 > 10^{-4}\left(\frac{1-r}{0.1}\right)^{-1}\left(\frac{P_{\rm orb}}{40\ \rm day}\right)^{4.1}\left(\frac{\mathcal{Q}_{\rm eq}}{10^8}\right)^{-1}. \tag{4.69}$$

It thus appears that resonance locks are indeed possible in eccentric binaries, subject to the validity of the assumptions enumerated in § 4.3 (e.g., solid-body rotation).

[7] Since we are considering an eccentric orbit, the tidal coupling coefficient U (on which $\Gamma_{\rm tide}$ depends) is additionally proportional to a Hansen coefficient, due to the Fourier expansion of the orbital motion (§ 4.4.1). We take this coefficient to be of order unity.

4.10 Conclusion

We have studied tidally induced resonance locking in close (but detached) binary systems. In a resonance lock, the detuning frequency $\delta\omega = \omega - \sigma$ between a stellar or planetary eigenmode frequency ω and a particular Fourier harmonic of the tidal driving frequency $\sigma = k\Omega_{\rm orb} - m\Omega_{\rm spin}$ is held constant (§ 4.2; Witte & Savonije 1999). This happens when a slowly varying physical process causing $\delta\omega$ to evolve in one direction is balanced by resonant interaction with the eigenmode in question causing $\delta\omega$ to evolve in the reverse direction. The slowly varying process could be, e.g., orbital decay due to gravitational waves causing $\Omega_{\rm orb}$ to increase, magnetic braking causing $\Omega_{\rm spin}$ to decrease, stellar evolution altering ω, or nonresonant components of the tidal response (the "equilibrium tide") affecting both $\Omega_{\rm orb}$ and $\Omega_{\rm spin}$ simultaneously.

Our primary goal has been to understand the dynamical properties and stability of resonance locks without relying on simplifying approximations for the mode amplitude evolution used in previous calculations. We defer detailed implications of these results to future papers. We have derived a novel set of equations allowing for a dynamically evolving mode amplitude coupled to the evolution of both $\Omega_{\rm spin}$ and $\Omega_{\rm orb}$ (§ 4.4). In particular, we do not assume that the mode amplitude is given by a Lorentzian profile resulting from the adiabatic approximation (§ 4.6.1) used in previous work, but instead solve the fully time-dependent mode amplitude equation.

In § 4.5 we analyzed the stability of the dynamical fixed points associated with resonance locks. We analytically derived when such fixed points exist (equation 4.29); there are either two fixed points or none for a given eigenmode. Although one of these equilibria is always unstable, the other can be stable when certain restrictions on binary and mode parameters are met (equation 4.40 in § 4.5.2). One of the important conclusions of this analysis is that resonance locks can exist and be stable even when the adiabatic approximation for the mode amplitude evolution is invalid (which happens, e.g., in the limit of moderately weak damping).

In § 4.6.2 we analyzed the properties of resonance locks using direct numerical integration of our dynamical equations. In the simplest case in which a resonance lock fixed point exists and is stable, two possibilities arise: either a resonance passage is able to pump the mode's amplitude up sufficiently high to reach the fixed point and be captured into it, creating the resonance lock (Figure 4.4), or the system instead sweeps through resonance without locking.

The more interesting situation is when both fixed points are unstable. In this case, we showed that resonance locking can nonetheless occur in some cases in a time-averaged sense. In these situations the mode amplitude and detuning frequency $\delta\omega$ execute limit cycles or even chaotic trajectories around the fixed points (see Figures 4.5 & 4.7). We presented evidence in § 4.6.3 suggesting that resonance locking may in fact correspond to a strange attractor for certain parameter values; see Figure 4.8.

In order to determine when resonance locking of some kind occurs (either stable, limit cycle, or chaotic), we performed numerical integrations over wide ranges of parameter values in § 4.7.1. Using analytic approximations from § 4.6.1, we then developed approximate analytic formulae that explain our numerical results and define the binary and mode parameter regimes in which resonance locks of some kind occur. The key results are equations (4.53) & (4.54) and Figure 4.10. Future studies of tidal evolution that do not include our full set of coupled mode-spin-orbit evolution equations can nonetheless utilize our results to assess whether resonance locks can occur.

One of the interesting consequences of resonance locks highlighted by Witte & Savonije (1999) and Witte & Savonije (2002) using numerical simulations in the adiabatic approximation is that locks can produce a significant speed up of orbital and spin evolution. We have explained this analytically in § 4.8.1. In particular, we have demonstrated that resonance locks generically act to produce orbital and spin evolution on a timescale that is somewhat shorter than the slowly varying physical process whose influence drives the system into a lock. The magnitude of this acceleration depends on the effective moment of inertia ratio r defined in equation (4.21) and is large for $r \sim 1$. The latter condition can only be satisfied in eccentric binaries or binaries with high mass ratios. For the case of an eccentric orbit, we derived a rough condition for significant acceleration of the rate of orbital and spin evolution in § 4.8.2.

To give a rough sense of the possible application of our results, we applied them to three sample astrophysical systems in § 4.9: inspiraling white dwarf and neutron star binaries in § 4.9.1, and eccentric binaries with early-type stars in § 4.9.2. As has been argued previously using the adiabatic approximation for mode amplitudes, resonance locks are likely very common in white dwarf binaries and eccentric stellar binaries. They cannot, however, occur in neutron star binaries since orbital decay by gravitational wave emission is too rapid. A future application that may be of considerable interest is tidal circularization during high-eccentricity migration of hot Jupiters.

The theory of resonance locking that we have developed bears some similarity to resonance capture in planetary dynamics (Murray & Dermott 1999). In the case of both mean-motion resonances (Goldreich 1965) and spin-orbit resonances (Goldreich & Peale 1968), the generic equation governing the evolution of the relevant angle Ψ towards resonance is

$$\ddot{\Psi} = -F \sin\Psi + G. \tag{4.70}$$

For mean-motion resonances, Ψ defines the angle between the mean anomalies of two orbiting bodies, while for spin-orbit resonances, Ψ is related to the difference between a body's mean and true anomalies (relevant only for eccentric orbits). In both cases, G provides a frequency drift term, resulting from orbital decay for mean-motion resonances and from a net tidal torque for spin-orbit resonances.

Equation (4.70) can be compared to our equation describing the evolution of the detuning frequency $\delta\omega = \omega - \sigma$ in equation (4.24). Both specify the second time derivative of a resonance angle, and both contain a frequency drift term describing how resonance is approached. The essential difference is that in place of the pendulum restoring force present in equation (4.70), tidal resonance locking instead contains two terms providing the complicated interaction with a stellar or planetary normal mode. Thus, although there are qualitative similarities between resonance capture in planetary dynamics and resonance locking, no formal mathematical analogy exists.

It is important to reiterate that resonance locks can only occur under a specific set of conditions (§ 4.3). They are not relevant to all close binaries. In particular, the dynamical tide must be composed of global radial standing waves, with damping times much longer than radial wave travel times. For this reason, an efficient angular momentum transport process must maintain approximate solid body rotation; if not, critical layers may develop where mode angular momentum is deposited into the background rotation profile, which would lead to efficient local wave damping. In addition, we have restricted our analysis to linear perturbation theory. In practice, this represents a restriction on the maximum mode amplitudes that are allowed, since nonlinear instabilities can act on large-amplitude waves. For example, in the case of binaries containing solar-type stars with radiative cores, wave breaking in the core likely prohibits the establishment of global standing waves (Goodman & Dickson 1998), thus also precluding resonance locks from developing.

Appendix A

Tidal asteroseismology

A.1 Nonadiabatic tidally driven oscillation equations

Here we will describe the computational procedure we employed to solve for tidally driven stellar responses, which we then used to model KOI-54's lightcurve. In Appendix A.1.1, we account for rotation only by using Doppler-shifted driving frequencies $k\Omega_{\rm orb} - m\Omega_*$, and neglect any effects of the Coriolis force; in Appendix A.1.2, we invoke the traditional approximation (Bildsten et al. 1996) to account for the Coriolis force (§ 2.3.4).

A.1.1 Formalism without the Coriolis force

The gravitational potential due to the secondary, experienced by the primary, is given by

$$U_{2\to 1} = -\frac{GM_2}{|D - r|}. \tag{A.1}$$

Performing a multipole expansion (Jackson 1999) and excising the $l = 0$ (since it is constant) and $l = 1$ (since it is responsible for the Keplerian center-of-mass motion) terms, we are left with the tidal potential:

$$U = -\frac{GM_2}{D(t)} \sum_{l=2}^{\infty} \sum_{m=-l}^{l} W_{lm} \left(\frac{r}{D(t)}\right)^l e^{-imf(t)} Y_{lm}(\theta, \phi), \tag{A.2}$$

where

$$\begin{aligned} W_{lm} &= \frac{4\pi}{2l+1} Y^*_{lm}(\pi/2, 0) \\ &= (-1)^{(l+m)/2} \mathrm{mod}(l+m+1, 2) \sqrt{\frac{4\pi}{2l+1} \frac{(l+m-1)!!}{(l+m)!!} \frac{(l-m-1)!!}{(l-m)!!}}. \end{aligned} \tag{A.3}$$

Next, we shift to the primary's corotating frame (by sending $\phi \to \phi + \Omega_* t$) and expand the time dependence of the orbit in terms of the Hansen coefficients:

$$U = \frac{M_2}{M_1} \sum_l \left(\frac{R_1}{a}\right)^{l+1} \sum_m W_{lm} Y_{lm}(\theta, \phi) \sum_k \exp(-i\sigma_{km} t) X_{lm}^k(e) U_l(r), \tag{A.4}$$

with $\sigma_{km} = k\Omega_{\rm orb} - m\Omega_*$ and

$$U_l(r) = -\left(\frac{GM_1}{R_1}\right)\left(\frac{r}{R_1}\right)^l. \tag{A.5}$$

The unit-normalized Hansen coefficients $\widetilde{X}_{lm}^k$ were defined in equation (2.11); here we are using the conventionally normalized Hansen coefficients $X_{lm}^k = \widetilde{X}_{lm}^k/(1-e)^{l+1}$, which are convenient to evaluate numerically as an integral over the eccentric anomaly:

$$X_{lm}^k = \frac{1}{\pi} \int_0^\pi (1 - e\cos E)^{-l} \cos\left[k(E - e\sin E) - 2m \arctan\left(\sqrt{\frac{1+e}{1-e}} \tan(E/2)\right)\right] dE. \tag{A.6}$$

If we represent the linear response of a star to the perturbing tidal potential by an abstract vector $y(r, \theta, \phi, t)$ whose components are the various oscillation variables (e.g., ξ_r/r), then y can also be expanded, again *in the primary's corotating frame,* as in (A.4):

$$y = \frac{M_2}{M_1} \sum_l \left(\frac{R_1}{a}\right)^{l+1} \sum_m W_{lm} Y_{lm}(\theta, \phi) \sum_k \exp(-i\sigma_{km} t) X_{lm}^k(e) y_{lm}^k(r). \tag{A.7}$$

The equations necessary to determine $y_{lm}^k(r)$ are given in the appendix of Pfahl et al. (2008), along with appropriate boundary conditions; note that their U is our U_l and their driving frequency ω is our σ_{km}.

After determining $y_{lm}^k(r)$ in the corotating frame, we can switch to the inertial frame specified in § 2.3.1:

$$y = \frac{M_2}{M_1} \sum_l \left(\frac{R_1}{a}\right)^{l+1} \sum_k \exp(-ik\Omega_{\rm orb} t) \sum_m W_{lm} Y_{lm}(\theta, \phi) X_{lm}^k(e) y_{lm}^k(r). \tag{A.8}$$

As noted in § 2.4.2, we see in equation (A.8) that the observed *frequencies* should be pure harmonics of the orbital frequency, even though the corresponding *amplitudes* of observed pulsations are influenced by the star's rotation rate (via the Doppler-shifted frequency σ_{km}).

A.1.2 Rotation in the traditional approximation

We now invoke the traditional approximation (§ 2.3.4); we must correspondingly adopt the Cowling approximation and employ the Hough functions (§ 2.5) as angular basis functions instead of spherical harmonics.

We expand the Hough functions as (Longuet-Higgins 1968)

$$H^k_{\lambda m} = \sum_l e^k_{\lambda l m}\tilde{P}_{lm} \quad \to \quad e^k_{\lambda l m} = 2\pi \int_{-1}^{1} \widetilde{P}_{lm} H^k_{\lambda m} d\mu \quad \to \quad \widetilde{P}_{lm} = \sum_\lambda e^k_{\lambda l m} H^k_{\lambda m}, \tag{A.9}$$

where $\widetilde{P}_{lm}$ is a normalized associated Legendre function defined by

$$\widetilde{P}_{lm} = \sqrt{\frac{2l+1}{4\pi}\frac{(l-m)!}{(l+m)!}}\, P_{lm} \quad \to \quad Y_{lm}(\theta,\phi) = e^{im\phi}\widetilde{P}_{lm}(\cos\theta). \tag{A.10}$$

We used the numerical method of calculating the expansion coefficients $e^k_{\lambda l m}$ detailed in Ogilvie & Lin (2004) § 5.4. The tidal potential in the corotating frame is then

$$U = \frac{M_2}{M_1}\sum_l \left(\frac{R_1}{a}\right)^{l+1} \sum_m W_{lm} e^{im\phi} \sum_k \exp(-i\sigma_{km}t) X^k_{lm} \sum_\lambda H^k_{\lambda m}(\mu) U^k_{\lambda l m}(r), \tag{A.11}$$

where

$$U^k_{\lambda l m}(r) = -\left(\frac{GM_1}{R_1}\right)\left(\frac{r}{R_1}\right)^l e^k_{\lambda l m}, \tag{A.12}$$

$\sigma_{km} = k\Omega_{\rm orb} - m\Omega_*$, and the Coriolis parameter q on which the Hough functions depend is

$$q = 2\Omega_*/\sigma_{km}, \tag{A.13}$$

which justifies writing $H^k_{\lambda m}$ and $e^k_{\lambda l m}$ rather than $H^q_{\lambda m}$ and $e^q_{\lambda l m}$.

We again represent the linear response of a star, as in Appendix A.1.1, by a vector $y(r,\theta,\phi,t)$ whose components are the various oscillation variables, and which can be expressed in the inertial frame as:

$$\begin{aligned} y &= \frac{M_2}{M_1}\sum_k \exp(-ik\Omega_{\rm orb}t) \sum_l \left(\frac{R_1}{a}\right)^{l+1} \sum_m W_{lm} e^{im\phi} X^k_{lm}(e) \sum_\lambda H^k_{\lambda m}(\mu) y^k_{\lambda l m}(r) \\ &= \frac{M_2}{M_1}\sum_k \exp(-ik\Omega_{\rm orb}t) \sum_l \left(\frac{R_1}{a}\right)^{l+1} \sum_m W_{lm} X^k_{lm}(e) \sum_\lambda \sum_{l'} e^k_{\lambda l' m} Y_{l'm}(\theta,\phi) y^k_{\lambda l m}(r). \end{aligned} \tag{A.14}$$

The expansion of $H^q_{\lambda m}$ back into associated Legendre functions in the second line of equation (A.14) is useful since disk integrals are convenient to perform over spherical harmonics (§ 2.3.3).

Following Unno et al. (1989), we choose the components of y as

$$y_1 = \frac{\xi_r}{r}, \qquad y_2 = \frac{\delta p}{\rho g r}, \qquad y_5 = \frac{\Delta s}{c_p}, \quad \text{and} \quad y_6 = \frac{\Delta L}{L_r}, \tag{A.15}$$

where we have omitted the variables corresponding to the perturbed gravitational potential, y_3 and y_4. Equation (A.14) together with determination of the radial displacement $\xi_r/r = y_1$ and the

Lagrangian flux perturbation $\Delta F/F = y_6 - 2y_1$ at the photosphere then enables use of the formalism from § 2.3.3 to compute the flux perturbation as seen by an observer.

Next, we present the differential equations which determine a particular component $y^k_{\lambda lm}(r)$ of the full response in radiative zones. These equations are nearly identical to those in the appendix of Pfahl et al. (2008), but with $l(l+1)$ replaced by λ and with certain terms set to zero as per the traditional approximation. In practice these terms can be left in, since they are nearly zero for situations where the traditional approximation is valid; this is then a smooth way of transitioning among different regimes. Omitting (λlmk) indices and denoting $U = U^k_{\lambda lm}$ and $\omega = \sigma_{km}$, the equations are

$$\frac{dy_1}{d\ln r} = y_1\left(\frac{gr}{c_s^2} - 3\right) + y_2\left(\frac{\lambda g}{\omega^2 r} - \frac{gr}{c_s^2}\right) - y_5\rho_s + \frac{\lambda}{\omega^2 r^2}U \tag{A.16}$$

$$\frac{dy_2}{d\ln r} = y_1\left(\frac{\omega^2 - N^2}{g/r}\right) + y_2\left(1 - \eta + \frac{N^2}{g/r}\right) - y_5\rho_s - \frac{1}{g}\frac{dU}{dr} \tag{A.17}$$

$$\begin{aligned}\frac{dy_5}{d\ln r} = {} & y_1\frac{r}{H_p}\left[\nabla_{\rm ad}\left(\eta - \frac{\omega^2}{g/r}\right) + 4(\nabla - \nabla_{\rm ad}) + c_2\right] + y_2\frac{r}{H_p}\left[(\nabla_{\rm ad} - \nabla)\frac{\lambda g}{\omega^2 r} - c_2\right] \\ & + y_5\frac{r}{H_p}\nabla(4 - \kappa_s) - y_6\frac{r}{H_p}\nabla + \frac{r}{H_p}\left[\nabla_{\rm ad}\left(\frac{dU/dr}{g}\right) + (\nabla_{\rm ad} - \nabla)\frac{\lambda}{\omega^2 r^2}U\right]\end{aligned} \tag{A.18}$$

$$\frac{dy_6}{d\ln r} = y_2\left(\frac{\lambda\gamma g}{\omega^2 r}\right) + y_5\left(i\omega\frac{4\pi r^3 \rho c_p T}{L}\right) - y_6\gamma + \left(\frac{\lambda\gamma}{\omega^2 r^2}\right)U, \tag{A.19}$$

where $\eta = 4\pi r^3\rho/M_r$, $\gamma = 4\pi r^3\rho\varepsilon/L_r$, $c_2 = (r/H_p)\nabla(\kappa_{\rm ad} - 4\nabla_{\rm ad}) + \nabla_{\rm ad}(d\ln\nabla_{\rm ad}/d\ln r + r/H_p)$, $H_p = \rho g/p$ is the pressure scale height, and ε is the specific energy generation rate.

We need four boundary conditions for our four variables. Our first three are

$$0 = \xi_r(0) \qquad \text{evanescence in convective core,} \tag{A.20}$$

$$0 = \Delta s(0) \qquad \text{adiabaticity/evanescence in core,} \tag{A.21}$$

$$0 = \frac{\Delta F(R)}{F(R)} - 4\frac{\Delta T(R)}{T(R)} \qquad \text{blackbody at the stellar surface,} \tag{A.22}$$

where $\Delta T/T$ can be cast in terms of y_1, y_2, and y_5 using standard thermodynamic derivative identities.

A final surface boundary condition that allows for traveling and/or standing waves can be generated by imposing energetic constraints at the surface. This is detailed in Unno et al. (1989) pp. 163 – 167 for adiabatic oscillations. To generalize the boundary condition to include nonadiabaticity, rotation, and inhomogeneous tidal forcing, we write equations (A.16) – (A.19) as

$$\frac{dy}{d\ln r} = My + b, \tag{A.23}$$

where M and b are treated as constant near the stellar photosphere. The constant solution is $y_0 = -M^{-1}b$; defining $z = y - y_0$, the homogeneous solutions for z can be computed by diagonalizing M. In the evanescent case, we eliminate the solution for y with outwardly increasing energy density.

Alternatively, in the traveling wave case, we eliminate the inward-propagating wave. The final boundary condition is then implemented by setting the amplitude of the eliminated homogeneous solution to zero, and solving for a relationship between the original fluid variables implied by this statement.

A.2 Analytic model of ellipsoidal variation

As discussed in § 2.6.1, our simplified model of ellipsoidal variation reproduces the much more sophisticated simulation code employed by Welsh et al. (2011) to model KOI-54; here we discuss the details of our analytic methods, which can easily be applied to model other systems.

A.2.1 Irradiation

The following is our simple analytical model of the insolation component of the KOI-54's ellipsoidal variation. We focus our analysis on the primary, since extending our results to the secondary is trivial. Our main assumption is that all radiation from the secondary incident upon the primary is immediately reprocessed at the primary's photosphere and emitted isotropically (i.e., absorption, thermalization, and reemission). This assumption is well justified for KOI-54, since its two component stars are of very similar spectral type. The method below might need to be modified if the components of a binary system had significantly different spectral types, because then some of the incident radiation might instead be scattered.

The incident flux on the primary, using the conventions and definitions introduced in § 2.3.1, is

$$F_{2\to 1} = \frac{L_2}{4\pi D^2} Z(\hat{r}\cdot\hat{D}), \tag{A.24}$$

where Z is the ramp function, defined by

$$Z(x) = \begin{cases} 0 & x < 0 \\ x & x \geq 0 \end{cases}. \tag{A.25}$$

We can expand $Z(\hat{r}\cdot\hat{D})$ in spherical harmonics as

$$Z(\hat{r}\cdot\hat{D}) = \sum_{lm} Z_{lm} Y_{lm}(\theta,\phi)\, e^{-imf(t)}, \tag{A.26}$$

where Z_{lm} can be evaluated to

$$Z_{lm} = 2\left(\frac{2l+1}{4\pi}\cdot\frac{(l-m)!}{(l+m)!}\right)^{1/2}\left(\frac{\cos(m\pi/2)}{1-m^2}\right)\int_{-1}^{1}\sqrt{1-\mu^2}P_{lm}\,d\mu, \tag{A.27}$$

with $\cos(m\pi/2)/(1-m^2) \to \pi/2$ for $m = \pm 1$.

Next, taking the reemission as isotropic, the reemitted intensity will be

$$I_{\rm emit} = \frac{F_{2\to 1}}{\pi}. \tag{A.28}$$

Using this together with our expansion of $Z(\hat{r}\cdot\hat{D})$ as well as results from § 2.3.3, we can evaluate the observed flux perturbation:

$$\frac{\delta J}{J_1} = \beta(T_1)\left(\frac{L_2}{L_1}\cdot\frac{R_1^2}{D(t)^2}\right)\sum_{l=0}^{\infty}\sum_{m=-l}^{l} b_l\, Z_{lm}\, Y_{lm}(\theta_{\rm o},\phi_{\rm o})\, e^{-imf(t)}, \tag{A.29}$$

where $J_1 = L_1/4\pi s^2$ is the unperturbed observed flux, s is the distance to the observer, the bandpass correction coefficient $\beta(T)$ is defined in equation (2.19), the disk-integral factor b_l is defined in equation (2.23), several values of b_l using Eddington limb darkening are given in Table 2.3, and other variables are defined in § 2.3.1. Since b_l declines rapidly with increasing l, it is acceptable to include only the first few terms of the sum in equation (A.29). We have neglected limb darkening, so it is formally necessary to use a flat limb darkening law in calculating b_l ($h(\mu) = 2$; § 2.3.3). However, we found this to be a very modest effect.

The binary separation D and the true anomaly f can be obtained as functions of time in various ways, e.g., by expanding with the Hansen coefficients employed earlier (equation 2.11 or A.6), or by using

$$D = \frac{a(1-e^2)}{1+e\cos f} \tag{A.30}$$

together with numerical inversion of

$$\Omega_{\rm orb} t = 2\arctan\left(\frac{(1-e)\tan(f/2)}{\sqrt{1-e^2}}\right) - \frac{e\sqrt{1-e^2}\sin f}{1+e\cos f}, \quad -\pi < f < \pi. \tag{A.31}$$

The observed flux perturbation from the secondary is obtained from equation (A.29) by switching $1 \leftrightarrow 2$ and sending $\phi_o \to \phi_o + \pi$.

Using the fact that $b_0 = 1$ and $Z_{00} = \sqrt{\pi}/2$, it can be readily verified that the total reflected power, i.e. $s^2 J_1$ times (A.29) integrated over all observer angles (θ_o, ϕ_o), is equal to $L_2(\pi R_1^2/4\pi D^2)$. This is just the secondary's luminosity times the fraction of the secondary's full solid angle occupied by the primary, which is the total amount of the secondary's radiation incident on the primary.

A.2.2 Equilibrium tide

We invoke the Cowling approximation (well satisfied for surface values of perturbation variables), and use the analytic equilibrium tide solution, where the radial displacement at star 1's surface becomes

$$\xi_r = -\frac{U(R_1,t)}{g(R_1)}, \tag{A.32}$$

and U is the tidal potential. Using the expansion in equation (A.2), $\xi_{r,lm}(t)/R_1$ from equation (2.20) becomes (Goldreich & Nicholson 1989a)

$$\frac{\xi_{r,lm}(t)}{R_1} = \frac{M_2}{M_1}\left(\frac{R_1}{D(t)}\right)^{l+1} W_{lm}\, e^{-imf(t)}. \tag{A.33}$$

We invoke von Zeipel's theorem (von Zeipel 1924; Pfahl et al. 2008) to determine the corresponding surface emitted flux perturbation:

$$\frac{\Delta F_{lm}(t)}{F_1} = -(l+2)\frac{\xi_{r,lm}(t)}{R_1}. \tag{A.34}$$

We can then explicitly evaluate the observed flux variation using the formalism from § 2.3.3:

$$\frac{\delta J}{J_1} = \frac{M_2}{M_1}\sum_{l=2}^{\infty}\left(\frac{R_1}{D(t)}\right)^{l+1}\sum_{m=-l}^{l}\left\{\left[2-\beta(T_1)(l+2)\right]b_l - c_l\right\} W_{lm}\, Y_{lm}(\theta_\mathrm{o},\phi_\mathrm{o})\, e^{-imf(t)}, \tag{A.35}$$

where the bandpass correction coefficient $\beta(T)$ is defined in equation (2.19), W_{lm} is defined in equation (A.3), the disk-integral factors b_l and c_l are defined in equations (2.23) and (2.24), several values of b_l and c_l using Eddington limb darkening are given in Table 2.3, and other variables are defined in § 2.3.1. Due to the strong dependence on l, it is typically acceptable to include only the first term of the sum in equation (A.29). Computation of the binary separation $D(t)$ and true anomaly $f(t)$ is discussed in Appendix A.2.1. The observed flux perturbation from the secondary is obtained from equation (A.35) by switching $1 \leftrightarrow 2$ and sending $\phi_o \to \phi_o + \pi$.

We note that although the analytic equilibrium tide solution for the radial displacement ξ_r is a good approximation at the stellar surface regardless of stellar parameters, the presence of a significant surface convection zone in a solar-type star proscribes the use of equation (A.34); Pfahl et al. (2008) gives the appropriate replacement in their eq. (37). Moreover, we note that equation (A.34) may also be invalid for slowly rotating stars in eccentric orbits; see § 2.6.2.

A.3 Tidal orbital evolution

A.3.1 Eigenmode expansion of tidal torque and energy deposition rate

Assuming alignment of rotational and orbital angular momenta, the tidal torque τ produced by star 2 on star 1 must have only a z component, where $\hat{z}$ points along the orbital angular momentum. We can evaluate it as follows (Kumar & Quataert 1998). First,

$$\begin{aligned}\tau &= \hat{z}\cdot\int_*\left(r\times\frac{dF}{dV}\right)dV = \int_*(\hat{z}\times r)\cdot\frac{dF}{dV}\,dV \\ &= \int_*\hat{\phi}\cdot\left[-(\rho_0+\delta\rho)\boldsymbol{\nabla}U\right] r\sin\theta\, dV.\end{aligned} \tag{A.36}$$

The term involving the background density ρ_0 vanishes; expanding both the tidal potential U and the Eulerian density perturbation $\delta\rho$ in spherical harmonics with expansion coefficients $U_{lm}(r,t)$ and $\delta\rho_{lm}(r,t)$, we have

$$\tau(t) = i\sum_{l=2}^{\infty}\sum_{m=-l}^{l} m\int_0^{R_1} \delta\rho_{lm}(r,t)U_{lm}^*(r,t)r^2dr. \tag{A.37}$$

Further invoking the expansions from equations (2.5) and (A.4), as well as the definitions in § 2.3.2, we arrive with

$$\tau(t) = -2\,i\left(\frac{GM_1^2}{R_1}\right)\sum_{nlmkk'} m\frac{(\varepsilon_l Q_{nl}W_{lm})^2}{E_{nl}}\widetilde{X}_{lm}^k\widetilde{X}_{lm}^{k'}\Delta_{nlmk}e^{i(k'-k)\Omega_{\rm orb}t}. \tag{A.38}$$

Lastly, averaging over a complete orbital period and rearranging the sums, we derive our final expression for the secular tidal torque:

$$\begin{aligned}\langle\tau\rangle = 8\left(\frac{GM_1^2}{R_1}\right)\left(\frac{M_2}{M_1}\right)^2\sum_{l=2}^{\infty}\left(\frac{R_1}{a}\right)^{2l+2}&\sum_{m=-l}^{l} mW_{lm}^2\times\\ &\sum_{k=0}^{\infty}X_{lm}^k(e)^2\sum_n\left(\frac{Q_{nl}^2}{E_{nl}}\right)\left(\frac{\omega_{nl}^2\sigma_{km}\gamma_{nl}}{(\omega_{nl}^2-\sigma_{km}^2)^2+4\gamma_{nl}^2\sigma_{km}^2}\right).\end{aligned} \tag{A.39}$$

The torque depends on the rotation rate Ω_* only through the Doppler-shifted frequency $\sigma_{km} = k\Omega_{\rm orb} - m\Omega_*$, since we have neglected rotational modification of the eigenmodes (§ 2.3.4). Figure 2.4 shows plots of this torque evaluated for KOI-54.

Note that a particular term of this sum is positive if and only if $m\sigma_{km} = m(k\Omega_{\rm orb} - m\Omega_*) > 0$, which reduces to $(k/m)\Omega_{\rm orb} > \Omega_*$. This is known as being prograde, since it is equivalent to the condition that a mode's angular structure, in the corotating frame, rotate in the same sense as the stellar spin; conversely, retrograde waves with $(k/m)\Omega_{\rm orb} < \Omega_*$ cause negative torques.

Using similar techniques to those given above, an equivalent expansion of the secular tidal energy deposition rate into the star (including mechanical rotational energy) can be derived:

$$\begin{aligned}\langle\dot{E}\rangle = 8\Omega_{\rm orb}\left(\frac{GM_1^2}{R_1}\right)\left(\frac{M_2}{M_1}\right)^2\sum_{l=2}^{\infty}\left(\frac{R_1}{a}\right)^{2l+2}&\sum_{m=-l}^{l} W_{lm}^2\times\\ &\sum_{k=0}^{\infty}kX_{lm}^k(e)^2\sum_n\left(\frac{Q_{nl}^2}{E_{nl}}\right)\left(\frac{\omega_{nl}^2\sigma_{km}\gamma_{nl}}{(\omega_{nl}^2-\sigma_{km}^2)^2+4\gamma_{nl}^2\sigma_{km}^2}\right).\end{aligned} \tag{A.40}$$

The only difference between equations (A.39) and (A.40) is switching $m \leftrightarrow k\Omega_{\rm orb}$.

A.3.2 Nonresonant pseudosynchronization

A pseudosynchronous frequency $\Omega_{\rm ps}$ is defined as a rotation rate that produces no average tidal torque on the star throughout a sufficiently long time interval, which here we take to be a complete orbital period (§ 2.5). I.e.,

$$\langle\tau\rangle(\Omega_{\rm ps}) = 0. \tag{A.41}$$

Here we will show that our expansion from A.3.1 reproduces the value of $\Omega_{\rm ps}$ derived in Hut (1981), which we denote $\Omega_{\rm ps}^{\rm nr}$, in the equilibrium tide limit. We will in particular show that Hut's result is independent of assumptions about eigenmode damping rates.

Proceeding, we take the nonresonant (equilibrium tide) limit of equation (A.39). This is obtained by retaining only the first term in the Taylor series expansion in σ_{km}/ω_{nl} of the last factor in parentheses from equation (A.39), and yields

$$\langle\tau_{\rm nr}\rangle = 8\left(\frac{GM_1^2}{R_1}\right)\left(\frac{M_2}{M_1}\right)^2\sum_{l=2}^{\infty}\left(\frac{R_1}{a}\right)^{2l+2}\left[\sum_{m>0}^{l} mW_{lm}^2\sum_{k=-\infty}^{\infty}X_{lm}^k(e)^2\sigma_{km}\right]\left[\sum_n\left(\frac{Q_{nl}^2}{E_{nl}}\right)\left(\frac{\gamma_{nl}}{\omega_{nl}^2}\right)\right]; \tag{A.42}$$

note that sums over k and m become decoupled from the sum over n. Setting $\langle\tau_{\rm nr}\rangle(\Omega_{\rm ps}^{\rm nr}) = 0$ and retaining only $l = 2$, we have

$$0 = \sum_{k=-\infty}^{\infty} X_{22}^k(e)^2\left(k\Omega_{\rm orb} - 2\Omega_{\rm ps}^{\rm nr}\right). \tag{A.43}$$

We need two identities to evaluate this further. First, starting with the definition of the Hansen coefficients,

$$\left(\frac{a}{D}\right)^{l+1} e^{-imf} = \sum_{k=-\infty}^{\infty} X_{lm}^k e^{-ik\Omega_{\rm orb}t}, \tag{A.44}$$

we can differentiate with respect to t, then multiply by the complex conjugate of (A.44) and average over a complete period to derive

$$\sum_{k=-\infty}^{\infty} k\left(X_{lm}^k\right)^2 = \frac{m}{2\pi}\int_0^{2\pi}\left(\frac{1+e\cos f}{1-e^2}\right)^{2l+2} df. \tag{A.45}$$

Specializing to $l = 2$,

$$\sum_{k=-\infty}^{\infty} k\left(X_{2m}^k\right)^2 = m\left[\frac{5e^6+90e^4+120e^2+16}{16(1-e^2)^6}\right]. \tag{A.46}$$

The second identity needed,

$$\sum_{k=-\infty}^{\infty}\left(X_{2m}^k\right)^2 = \frac{3e^4+24e^2+8}{8(1-e^2)^{3/2}}, \tag{A.47}$$

can be derived similarly.

Substituting equations (A.46) and (A.47) into (A.43), we have that

$$\Omega_{\text{ps}}^{\text{nr}} = \Omega_{\text{orb}} \cdot \frac{1+(15/2)e^2+(45/8)e^4+(5/16)e^6}{\left[1+3e^2+(3/8)e^4\right](1-e^2)^{3/2}}; \tag{A.48}$$

this is precisely eq. (42) from Hut (1981).

Appendix B

Tides in inspiraling white dwarf binaries

B.1 Angular momentum transport

If we assume there is a source of angular momentum near the WD surface, e.g. from tides, a fossil magnetic field of initial magnitude $\sim B_0$ will wind up and exert magnetic tension forces attempting to enforce solid-body rotation. The rate at which magnetic tension transports polar angular momentum through a spherical surface S at radius r is given by

$$\dot{J}_z = \frac{1}{4\pi} \int_S B_r B_\phi \, r \sin\theta \, dS, \tag{B.1}$$

which can be derived by applying the divergence theorem to the magnetic tension force density $(B \cdot \boldsymbol{\nabla})B/4\pi$. As the field winds up, the radial component remains constant, while the azimuthal component increases as (Spruit 1999)

$$B_\phi = N_{\rm w} B_r, \tag{B.2}$$

where $N_{\rm w} = r \sin\theta \int (d\Omega_{\rm spin}/dr) dt$ is the rotational displacement that occurs during wind up and we have assumed the rotational velocity field can be described by "shellular" rotation: $v = \Omega_{\rm spin}(r) r \sin\theta \hat{\phi}$.

Once the field wind up propagates into the WD core, an equilibrium field is established that communicates the tidal torque throughout the WD and eliminates any rotational shear. There are several requirements necessary for this equilibrium to be reached during inspiral, and consequently for WDs in inspiraling binaries to rotate as a rigid bodies.

B.1.1 Solid-body rotation at short orbital periods

Whether there is sufficient time for the global equilibrium magnetic field to develop and eliminate differential rotation altogether amounts to whether the timescale over which the torque changes, given by the gravitational wave inspiral time $t_{\rm gw}$ (equation 3.1), is longer than the timescale over which the wind up of the magnetic field propagates into the core, which is given by the global Alfvén crossing time $\langle t_{\rm A} \rangle = \int dr/v_{\rm A}$, where $v_{\rm A} = B_r/\sqrt{4\pi\rho}$ is the radial Alfvén speed. This restriction translates to

$$B_0 \gg \frac{1}{t_{\rm gw}} \int_0^R \sqrt{4\pi\rho}\, dr, \tag{B.3}$$

where we have assumed $B_r \sim B_0 \sim$ constant. We can evaluate this further as

$$B_0 \gg 0.2\ \mathrm{G} \left(\frac{P_{\rm orb}}{10\ \mathrm{min}}\right)^{-8/3} F_1 \tag{B.4}$$

where

$$F_1 = \left(\frac{M'}{M}\right)\left(\frac{1+M'/M}{2}\right)^{-1/3}\left(\frac{M}{0.60M_\odot}\right)^{13/6}\left(\frac{R}{0.013R_\odot}\right)^{-1/2}.$$

The other requirement for solid-body rotation is that the rotational displacement $N_{\rm w}$ required for the equilibrium field configuration must not be too extreme, since the field becomes susceptible to resistive dissipation as well as various instabilities as it winds up (Spruit 1999). We can address this constraint by setting the tidal torque appropriate for a resonance lock $\tau_r = I_r\Omega/t_{\rm gw}$ (equation 3.9), where I_r is the moment of inertia up to a radius r, equal to equation (B.1), and then requiring $N_{\rm w} \lesssim 1$. Solving for B_0, we have

$$B_0 \gtrsim \sqrt{\frac{\tau}{r^3}} = \sqrt{\frac{I_r\Omega}{r^3 t_{\rm gw}}}. \tag{B.5}$$

Since the right-hand side of equation (B.5) scales radially as r^1, we can safely set $I_r = I_*$ and $r = R$. Evaluating this further yields

$$B_0 \gtrsim 10^4\ \mathrm{G} \left(\frac{P_{\rm orb}}{10\ \mathrm{min}}\right)^{-11/6} F_2, \tag{B.6}$$

where

$$F_2 = \left(\frac{M'}{M}\right)^{1/2}\left(\frac{1+M'/M}{2}\right)^{-1/6}\left(\frac{I_*}{0.18MR^2}\right)^{1/2}\left(\frac{M}{0.6M_\odot}\right)^{4/3}\left(\frac{R}{0.013R_\odot}\right)^{-1/2}. \tag{B.7}$$

We see that equation (B.4) is likely to hold nearly until mass transfer, meaning there is always sufficient time to set up an equilibrium field capable of stably transmitting angular momentum throughout the WD and enforcing solid-body rotation. Equation (B.6) is more restrictive, however, and shows that even for a fossil field of initial magnitude of $B_0 \sim 10^6$ G in a carbon/oxygen WD (§ 3.6.2), excessive wind up may begin to occur below an orbital period of ~ 1 min. Nonetheless, at orbital periods of ~ 100 min where standing-wave resonance locks occur, which require solid-body rotation, equation (B.6) requires only modest fields of ~ 200 G.

Lastly, although angular momentum transport occurs due to a wound-up equilibrium magnetic field, torsional Alfvén waves can also be excited, which cause oscillations in the differential rotation profile. Formally, a phase-mixing timescale must elapse before such waves damp (Spruit 1999). However, due to the slowly varying torque, we expect Alfvén wave excitation to be weak.

Indeed, in simulations of the solar magnetic field's evolution, Charbonneau & MacGregor (1993) found that Alfvén wave amplitudes (in terms of $\delta\Omega_{\rm spin}/\Omega_{\rm spin}$) were small.

B.1.2 Transport during an initial resonance lock

When a standing wave resonance lock first begins to takes hold, angular momentum is applied exclusively to a thin layer near the outer wave turning point where wave damping predominantly occurs. Since no equilibrium field state has yet developed in this situation, a concern exists that the layer will rapidly synchronize and destroy the lock before it begins (§ 3.6.2).

To this end, we first compare the spin-up timescale of the layer to the Alfvén travel time $t_{\rm A}$ across it. Using the torque for a resonance lock from equation (3.9) and taking $t_{\rm A} = H/v_{\rm A}$, where H is the thickness of the layer, we have

$$\frac{(2/3)4\pi\rho r^4 H\Omega_{\rm spin}}{I_*\Omega_{\rm spin}/t_{\rm gw}} \gg \frac{H\sqrt{4\pi\rho}}{B_r}. \tag{B.8}$$

Evaluating ρ at the radiative-convective boundary (RCB), letting $B_r \sim B_0$, and setting $r \approx R$, this becomes

$$B_0 \gg \sqrt{\frac{4\pi}{\rho_{\rm rcb}}}\left(\frac{3I_*}{8\pi R^4 t_{\rm gw}}\right). \tag{B.9}$$

We can evaluate this further as

$$B_0 \gg 10^{-3}\ {\rm G}\left(\frac{P_{\rm orb}}{200\ {\rm min}}\right)^{-8/3} F_3, \tag{B.10}$$

where

$$F_3 = \left(\frac{\rho_{\rm rcb}}{8.4\times10^{-7}\rho_{\rm c}}\right)^{-1/2}\left(\frac{M'}{M}\right)\left(\frac{1+M'/M}{2}\right)^{-1/3}\left(\frac{I_*}{0.18MR^2}\right)\left(\frac{M}{0.60M_\odot}\right)^{13/6}\left(\frac{R}{0.013R_\odot}\right)^{-1/2}$$

and $\rho_{\rm c}$ is the central density.

Secondly, even if no critical layer occurs, it is still necessary for the *global,* wound-up equilibrium field to develop quickly in order for an initial resonance lock to develop. Specifically, in order for a particular resonance to halt the increase in the tidal driving frequency $\sigma = 2(\Omega - \Omega_{\rm spin})$, its locally applied tidal torque must be communicated globally fast enough relative to the timescale over which the torque changes significantly. If this cannot occur, the system sweeps through the resonance without locking (see also § 3.6.3). The timescale over which a maximally resonant torque decays by roughly a factor of two is given by the time for the detuning $\delta\omega$ to increase from zero to of order the associated mode's damping rate γ_n (see e.g. equation 3.5; also Appendix B.2.3). Comparing to the global Alfvén travel time $\langle t_{\rm A}\rangle$, this condition becomes

$$B_0 \gg \frac{\Omega}{\gamma_n t_{\rm gw}}\int_0^R \sqrt{4\pi\rho}\,dr, \tag{B.11}$$

which is identical to equation (B.3) except with an additional factor of Ω/γ_n on the right-hand side. Evaluating further, we have

$$B_0 \gg 100\ \mathrm{G} \left(\frac{P_{\mathrm{orb}}}{200\ \mathrm{min}}\right)^{-11/3} \left(\frac{\gamma_n^{-1}}{120\ \mathrm{yr}}\right) F_1, \tag{B.12}$$

where F_1 was defined in Appendix B.1.1. The value of 100 G reduces to 6 G for a helium WD (`He7` from Table 3.1), holding γ_n constant. This is a much stricter requirement than equation (B.10), but still seems likely to be satisfied given typical WD fields (§ 3.6.2).

B.2 Global normal mode analysis

B.2.1 Mode dynamics

Here we give an overview of linear normal mode analysis as it applies to tidal interactions. As such, we assume the fluid motions generated by the tidal potential represent standing waves; we discuss the possibility of traveling waves in § 3.7.

In linear perturbation theory, we expand all fluid variables in spherical harmonics angularly, indexed by l and m, and adiabatic normal modes radially, indexed by the number of radial nodes n, as

$$\delta X(r,\theta,\phi,t) = \sum_{l=2}^{\infty} \sum_{m=-l}^{l} \sum_{n} q_{nlm}(t)\delta X_{nlm}(r) Y_{lm}(\theta,\phi). \tag{B.13}$$

We computed normal modes using the ADIPLS stellar pulsation package (Christensen-Dalsgaard 2008). In this work we concern ourselves only with quadrupolar eigenmodes, and consider only circular orbits, meaning we can let $l = 2$ and $m = \pm 2$, since $m = 0$ modes have no time dependence with zero eccentricity. Thus equation (B.13) becomes

$$\delta X(r,\theta,\phi,t) = 2\sum_{n} \mathrm{Re}\left[q_n(t)\delta X_n(r) Y_{22}(\theta,\phi)\right], \tag{B.14}$$

with $m = 2$ used throughout.

We can write the momentum equation schematically as (Press & Teukolsky 1977)

$$\rho\ddot{\boldsymbol{\xi}} = -\rho\mathcal{L}[\boldsymbol{\xi}] - \rho\nabla U, \tag{B.15}$$

where the linear internal acceleration operator $\mathcal{L}$ satisfies $\mathcal{L}[\boldsymbol{\xi}_n] = \omega_n^2\boldsymbol{\xi}_n$, ω_n is an eigenfrequency, and U is the tidal potential. The corotating frame mode amplitude equations determining the behavior of each q_n can be obtained from equation (B.15) by taking the scalar product with $\boldsymbol{\xi}_n^*$ on both sides and integrating over the star, yielding (e.g. Weinberg et al. 2012)

$$\ddot{q}_n + 2\gamma_n\dot{q}_n + \omega_n^2 q_n = 2\omega_n^2 \varepsilon W Q_n e^{-i\sigma t}, \tag{B.16}$$

where $W = \sqrt{3\pi/10}$, $\varepsilon = (M'/M)(R/a)^3$ is the tidal factor, $\sigma = m(\Omega - \Omega_{\rm spin})$ is the tidal driving frequency, and the linear overlap integral Q_n is discussed in Appendix B.2.4 (Press & Teukolsky 1977). We have also inserted into equation (B.16) a damping rate γ_n, the calculation of which we describe in Appendix B.2.3. We normalize our normal modes by setting

$$E_* = E_n = \int_0^R 2\omega_n^2 \left(\xi_{r,n}^2 + l(l+1)\xi_{{\rm h},n}^2\right) \rho r^2 dr. \tag{B.17}$$

Given slowly varying orbital and stellar properties, the steady-state solution to equation (B.16) is

$$q_n(t) = 2\varepsilon Q_n W \left(\frac{\omega_n^2}{(\omega_n^2 - \sigma^2) - 2i\gamma_n\sigma}\right) e^{-i\sigma t}. \tag{B.18}$$

The above amplitude applies in the corotating stellar frame; in the inertial frame the time dependence $e^{-i\sigma t}$ instead becomes $e^{-im\Omega t}$.

B.2.2 Angular momentum and energy transfer

Assuming a circular orbit and alignment of spin and orbital angular momenta, the secular quadrupolar tidal torque on a star is given by an expansion in quadrupolar ($l = 2$) normal modes as (Burkart et al. 2012 Appendix C1 and references therein)

$$\tau = 8mE_*\varepsilon^2 W^2 \sum_n Q_n^2 \frac{\omega_n^2 \sigma \gamma_n}{(\omega_n^2 - \sigma^2)^2 + 4\sigma^2\gamma_n^2}, \tag{B.19}$$

where most variables are defined in the previous section.

The tidal energy deposition rate into the star $\dot{E}_{\rm tide}$ can be determined from τ by the relation

$$-\dot{E}_{\rm orb} = \dot{E}_{\rm tide} = \Omega\tau, \tag{B.20}$$

valid only for a circular orbit. This can be derived by differentiating standard equations for the energy and angular momentum of a binary with respect to time, setting $\dot{e} = e = 0$, and noting that the tidal torques and energy deposition rates in each star of a binary are independent.

The total energy contained in the linear tide can be expressed in the corotating frame as (Schenk et al. 2002)

$$E_{\rm tide} = \frac{1}{2}\left\langle \dot{\boldsymbol{\xi}}, \dot{\boldsymbol{\xi}} \right\rangle + \frac{1}{2}\left\langle \boldsymbol{\xi}, \mathcal{L}[\boldsymbol{\xi}] \right\rangle, \tag{B.21}$$

where the operator $\mathcal{L}$ was introduced in Appendix B.2.1. Using results from Appendix B.2.1, we can evaluate this expression as

$$E_{\rm tide} = 2E_*\varepsilon^2 W^2 \sum_n Q_n^2 \frac{\omega_n^2(\sigma^2 + \omega_n^2)}{(\omega_n^2 - \sigma^2)^2 + 4\sigma^2\gamma_n^2}. \tag{B.22}$$

Lastly, since the great majority of the tidal energy is in the lowest-order modes, i.e. the equilibrium tide, which satisfy $\omega_n \gg \sigma$, we can further set $\sigma \approx 0$ in the previous equation to derive the simple expression

$$E_{\rm tide} \approx \lambda E_* \varepsilon^2, \tag{B.23}$$

where

$$\lambda = 2W^2 \sum_n Q_n^2. \tag{B.24}$$

Several limits can be taken of our general torque expression in equation (B.19). First, if we assume $\omega_n \gg (\sigma, \gamma_n)$, we arrive at the equilibrium tide limit:

$$\tau_{\rm eq} = 8mE_* \varepsilon^2 W^2 \sum_n Q_n^2 \left(\frac{\sigma \gamma_n}{\omega_n^2} \right). \tag{B.25}$$

Willems et al. (2010) showed that in linear theory the equilibrium tide provides a negligible torque due to the very weak damping present in WDs, resulting from their high densities and long thermal times. We confirm this result: e.g., the tidal quality factor associated with damping of the quadrupolar equilibrium tide in WDs is (equation 3.15)

$$Q_{\rm t}^{\rm eq} = \frac{1}{8} \frac{\sum_n Q_n^2}{\sum_n Q_n^2 \sigma \gamma_n / \omega_n^2} \gtrsim 10^{13}, \tag{B.26}$$

which is much larger than the effective value of $Q_{\rm t}$ for the dynamical tide determined in § 3.5.1. The resonant dynamical tide ($\omega_n \sim \sigma$ in equation B.19) is discussed in §§ 3.4 & 3.7.

B.2.3 Damping

We consider two different damping processes in this appendix: thermal diffusion and turbulent convection. We also calculate g-modes' group travel times, which sets the effective damping time for traveling waves. Figure B.1 shows plots of all three of these quantities for several of our fiducial WD models, and demonstrates that thermal diffusion is the dominant source of damping for high-order g-modes in WDs.

Damping due to electron conduction and radiative diffusion can be estimated simultaneously as (Goodman & Dickson 1998)

$$\gamma_n^{\rm diff} = \frac{1}{2E_n} \int \chi k_r^2 \frac{dE_n}{dr} dr, \tag{B.27}$$

where dE_n/dr is the integrand of equation (B.17), χ is the thermal diffusivity (including both radiative diffusion and electron conduction), and k_r is the radial wavenumber. In terms of an effective opacity κ, χ can be expressed as

$$\chi = \frac{16\sigma T^3}{3\kappa\rho^2 c_p}. \tag{B.28}$$

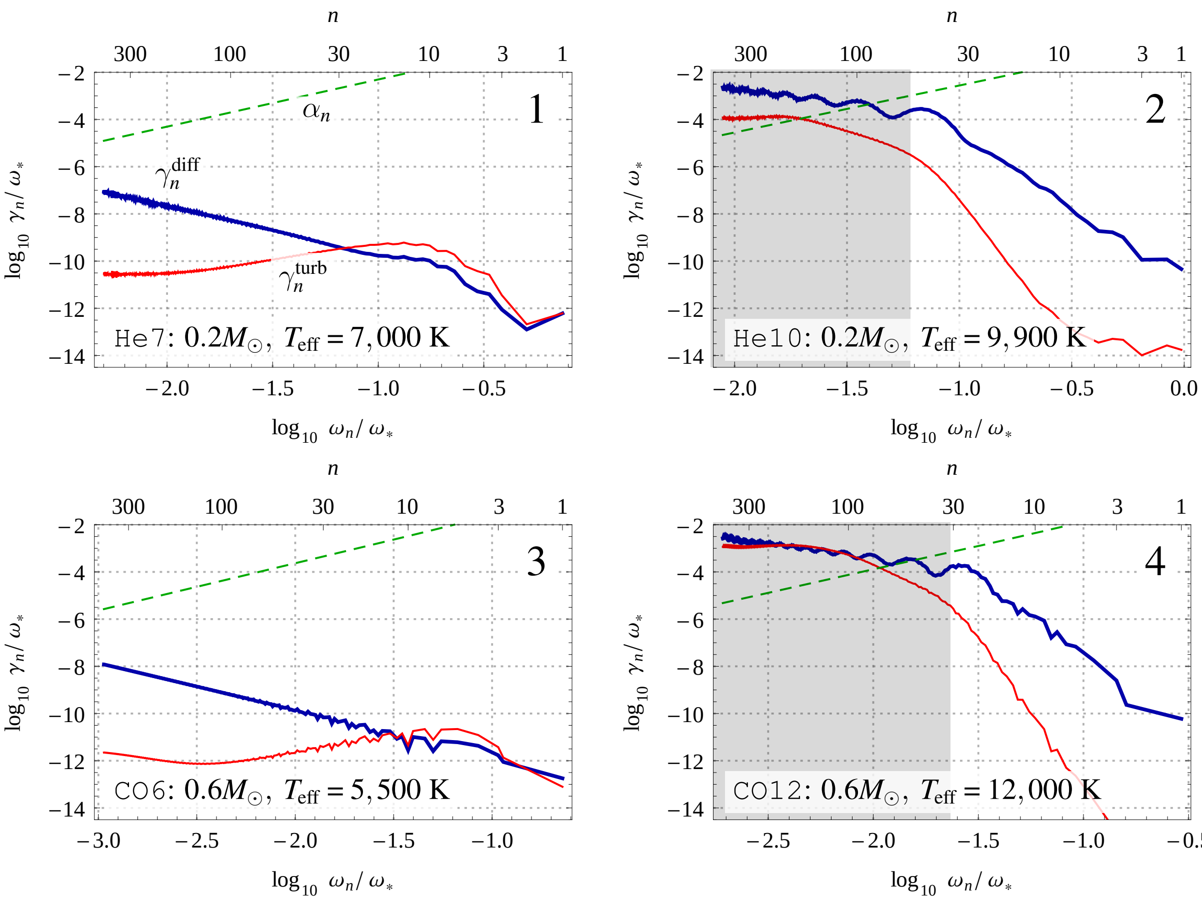

Figure B.1: Plots of the contributions to eigenmode damping rates due to thermal diffusion $\gamma_n^{\rm diff}$ (thick blue lines) and turbulent convection $\gamma_n^{\rm turb}$ (red lines), as well as the effective damping rate for traveling waves $\alpha_n = 2\pi/t_{{\rm group},n}$ (dashed green lines), as functions of the eigenmode frequency ω_n (in units of the dynamical frequency $\omega_{\rm dyn}$) and radial order n, for the first 400 g-modes in four of our fiducial WD models (Table 3.1). We describe the computation of these quantities in Appendix B.2.3. Inside the shaded regions in panels 2 & 4, g-modes become traveling waves due to rapid thermal diffusion near their outer turning points. In this case, approximating wave damping rates using $\gamma_n^{\rm diff} + \gamma_n^{\rm turb}$ is invalid, and a traveling wave formalism such as that discussed in § 3.7 must be used. Note that the WD models shown here are different from those in Figure 3.4.

For high-order g-modes, k_r is given by (Christensen-Dalsgaard 2008)

$$k_r^2 = k_{\rm h}^2 \left(\frac{N^2}{\omega^2} - 1 \right), \tag{B.29}$$

where $k_{\rm h}^2 = l(l+1)/r^2$ is the angular wavenumber. The integration in equation (B.27) is performed up to the adiabatic cutoff radius defined by $\omega t_{\rm th} = 1$ (Unno et al. 1989), where $t_{\rm th} = pc_pT/gF$ is the local thermal time. A wave's group travel time across a scale height must remain smaller than its local damping time in order for the wave to reflect. This criterion will always be broken for sufficiently long-period waves since the radial wavenumber k_r grows as ω^{-1}; nonetheless, we find that thermal diffusion is never strong enough to invalidate the standing wave assumption for all of the modes used in this work that are capable of effecting standing wave resonance locks.

To estimate the turbulent convective damping rate, we rely on the calibration of convective viscosity performed by Penev et al. (2009). The formula we employ is

$$\gamma_n^{\rm turb} \sim \frac{\omega_n^2}{E_n} \int \rho r^2 \nu_{\rm turb} \left[s_{0'} \left(\frac{d\xi_r}{dr} \right)^2 + s_1 l(l+1) \left(\frac{d\xi_{\rm h}}{dr} \right)^2 \right] dr, \tag{B.30}$$

where $s_{0'} = 0.23$ and $s_1 = 0.084$ (Penev & Sasselov 2011). For the effective turbulent viscosity $\nu_{\rm turb}$, we use equation (11) of Shiode et al. (2012):

$$\nu_{\rm turb} = L v_{\rm conv} \min \left[\frac{1}{\Pi_{\rm min}} \left(\frac{2\pi}{\omega t_{\rm eddy}} \right)^2, \left(\frac{2\pi}{\omega t_{\rm eddy}} \right), \Pi_{\rm max} \right], \tag{B.31}$$

where $v_{\rm conv}$ is the convective velocity, L is the mixing length, $t_{\rm eddy} = v_{\rm conv}/L$, $\Pi_{\rm min} = 0.1$, and $\Pi_{\rm max} = 2.4$.

Lastly, the effective damping rate applicable in the traveling wave regime is the inverse group travel time $\alpha = 2\pi/t_{\rm group}$; we can calculate $t_{\rm group}$ as

$$t_{\rm group} = 2 \int \frac{dr}{|v_{\rm group}|}, \tag{B.32}$$

where $v_{\rm group} = d\omega/dk_r$ and the integration is over the propagation cavity where the wave frequency $\omega < N$. Using the dispersion relation from equation (B.29), this becomes

$$\alpha = \pi \left(\int \frac{k_{\rm h} N}{\omega^2} dr \right)^{-1}. \tag{B.33}$$

For $\omega \ll N$, $\alpha \propto \omega^2$; this proportionality is verified in Table 3.3 and Figure B.1.

B.2.4 Linear overlap integral

The linear overlap integral for quadrupolar eigenmodes, introduced in equation (B.16), can be expressed as

$$\begin{aligned} Q_n &= \frac{1}{MR^l}\int_0^R l\left(\xi_{r,n}+(l+1)\xi_{\mathrm{h},n}\right)\rho r^{l+1}dr \\ &= \frac{1}{MR^l}\int_0^R \delta\rho_n\, r^{l+2}dr \\ &= -\frac{R}{GM}\cdot\frac{2l+1}{4\pi}\cdot\delta\phi_n(R), \end{aligned} \tag{B.34}$$

with $l=2$, where ξ_{h} is the horizontal fluid displacement. The second equality can be derived by substituting the continuity equation, and the third equality by substituting Poisson's equation. However, all three of these methods of calculating Q_n suffer from numerical difficulties, presumably arising due to a failure of orthogonality or completeness of the numerically computed eigenmodes (Fuller & Lai 2011), or to small inconsistencies in the stellar model (Fuller & Lai 2012a).

Thus we now consider a more stable way of numerically evaluating Q_n, which is what we actually employed in our calculations and the fits in Table 3.3. We again focus on $l=2$ modes, but the technique can easily be extended to arbitrary l. First, the tidally generated displacement field is given as a sum of normal modes in equation (B.13). If we set the tidal driving frequency σ and the damping rate γ_n to zero in equation (B.18) and substitute into equation (B.14) (while keeping the tidal factor ε nonzero), we recover the equilibrium tide limit. However, the equilibrium tide can alternatively be obtained by directly solving the inhomogeneous linear stellar oscillation equations in the zero-frequency limit; see e.g. Weinberg et al. (2012) Appendix A.1. Equating these two alternate expressions, taking the scalar product with $\rho\boldsymbol{\xi}_n^*$ on both sides, integrating over the star, and solving for Q_n, one obtains

$$Q_n = \frac{\omega_n^2}{WE_*}\int_0^R \left(X_{\mathrm{eq}}^r\xi_n^r + l(l+1)X_{\mathrm{eq}}^{\mathrm{h}}\xi_n^{\mathrm{h}}\right)\rho r^2 dr, \tag{B.35}$$

where

$$X_{\mathrm{eq}}(r,\theta,\phi) = \sum_{m=\pm 2}\left(X_{\mathrm{eq}}^r(r)\hat{r} + rX_{\mathrm{eq}}^{\mathrm{h}}(r)\boldsymbol{\nabla}\right)Y_{2m}(\theta,\phi) \tag{B.36}$$

is the numerically computed $l=2$ equilibrium tide scaled to $\varepsilon=1$.

Finally, there is one further method of computing Q_n that we have employed, which also uses a solution to the inhomogeneous equations. In this method, however, instead of comparing alternate computations of the equilibrium tide, we instead evaluate the inhomogeneous tidal response very near an eigenfrequency. The overlap can then be extracted by fitting the resulting Lorentzian profile of e.g. the tidal energy. This method numerically agrees very well with the equilibrium tide method described above.

B.3 Verification of traveling wave torque approximation

Here we will justify our traveling wave tidal torque approximation described in § 3.7.2 using several distinct lines of reasoning. Our goal is to explain why the traveling wave torque can be expressed in terms of the properties of global eigenmodes as in equation (3.32). This is a different approach than is typical in the literature.

First, in the limit that the wave damping time is much longer than the group travel time, the tidal response is well approximated as a standing wave. Thus taking the standing wave torque and setting the damping rate equal to the inverse group travel time (Appendix B.2.3) represents a natural method of smoothly transitioning to the traveling wave limit, since it corresponds to the situation where a wave is nearly completely absorbed over one travel time. One apparent difficulty with the resulting expression in our equation (3.32) is that it appears to contain explicit dependence on the wave travel time, which seems paradoxical, since a traveling wave has no information about the extent of the propagation cavity. This is, however, simply an artifact of our normalization convention. To show this, we first note that our approximation for $\tau_{\rm trav}$ depends on $\alpha = 2\pi/t_{\rm group}$ (Appendix B.2.3) only through

$$\tau_{\rm trav} \propto Q^2/\alpha. \tag{B.37}$$

Next, given the appropriate WKB expression for $\xi_{\rm h}$ (Christensen-Dalsgaard 2008),

$$\xi_{\rm h} \approx A\sqrt{\frac{N}{\rho r^3 \Lambda \sigma^3}} \sin\left(\int k_r dr + \delta\right), \tag{B.38}$$

where A is a constant, we impose our normalization convention from equation (B.17) and use the fact that $\xi_{\rm h} \gg \xi_r$ for g-modes to obtain

$$\begin{aligned} E_* &\approx 2\sigma^2 \int \Lambda^2 \xi_{\rm h}^2 \rho r^2 dr \\ &\approx A^2 \left(\frac{\pi\sigma\Lambda}{\alpha}\right), \end{aligned} \tag{B.39}$$

having set $\sin^2 \to 1/2$. This implies that unnormalized eigenfunctions (which are independent of global integrals) must be multiplied by $A \propto \alpha^{1/2}$ in order to be normalized properly. Since the overlap integral Q is linear in the eigenfunctions (Appendix B.2.4), re-examining equation (B.37) shows that $\tau_{\rm trav}$ is indeed independent of α and hence $t_{\rm group}$.

An alternate justification of our traveling wave torque expression can be obtained by considering how a traveling wave of a given frequency σ can be expressed in terms of global standing wave eigenmodes, which form a complete basis (Dyson & Schutz 1979). Obtaining a traveling wave functional form of $e^{i(kr \pm \sigma t)}$ requires summing at least two real-valued eigenmodes with a relative global phase difference between their complex amplitudes of $\pm\pi/2$, where both modes possess frequencies close to σ. Examining equation (B.18), we see that the phase of a standing mode's amplitude is given by $\arctan(\gamma/\delta\omega)$. Thus, in order to approximate a traveling wave of commensurate

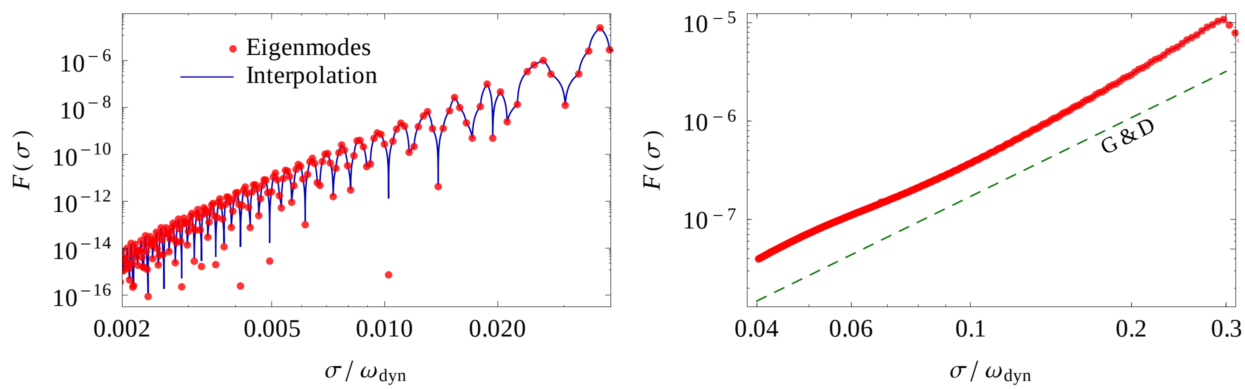

Figure B.2: Dimensionless traveling wave tidal torque $F(\sigma) = \tau_{\rm trav}/\varepsilon^2 E_*$, computed as described in § 3.7.2. Red points show direct evaluations of equation (3.32) at eigenmode frequencies, while blue lines are linear interpolations of these values. *Left panel:* Results for our $0.6M_\odot$, $T_{\rm eff} = 5,500$ K `CO6` WD model (Table 3.1). To facilitate straightforward comparison, this plot employs the same axes and conventions as in Figure 8 of Fuller & Lai (2012a). *Right panel:* Results for a solar model, which agrees reasonably well with the semi-analytic traveling wave result in equation (13) of Goodman & Dickson (1998) (dashed green line).

frequency, two adjacent eigenmodes 1 and 2 must satisfy

$$\arctan\left(\frac{\gamma_1}{\delta\omega_1}\right) - \arctan\left(\frac{\gamma_2}{\delta\omega_2}\right) = \pm\frac{\pi}{2}, \tag{B.40}$$

which simplifies to $\gamma_1\gamma_2 = \delta\omega_1\delta\omega_2$. Setting $|\delta\omega_{1,2}| \approx (\Delta P_0/2\pi)\sigma^2 \approx \alpha$, where ΔP_0 is the asymptotic g-mode period spacing, we find that the damping rate required to produce a traveling wave is $\gamma \sim 2\pi/t_{\rm group}$, consistent with our equation (3.32).

Lastly, we will quantitatively demonstrate that our approximation for the traveling wave tidal torque reproduces results available in the literature. First, the left panel of Figure B.2 shows our traveling wave torque evaluated for our `CO6` WD model (Table 3.1), expressed in the dimensionless form $F(\sigma) = \tau_{\rm trav}/\varepsilon^2 E_*$, as a function of the $l = m = 2$ tidal forcing frequency $\sigma = 2(\Omega - \Omega_{\rm spin})$. Comparing this to Figure 8 of Fuller & Lai (2012a), which employs the same conventions and axes, shows reasonable agreement. In particular, both exhibit the jagged variation with frequency discussed in § 3.7.1. Our result has a slightly steeper overall trend, leading to a smaller torque at low frequencies; however, because excitation is sensitive to the details of the composition boundaries in the model, there is no reason to expect detailed agreement. In addition, the right panel of Figure B.2 compares traveling wave results for solar-type stars from Goodman & Dickson (1998) (using their equation 13) with our equation (3.32) applied to a solar model. Both possess the same power-law scaling with frequency, and agree in normalization within a factor of ~ 2.

B.4 White dwarf models

We used MESA version 4298 (Paxton et al. 2011) to produce our helium WD models (Table 3.1: `He5`, `He7`, and `He10`). We used three inlists. The first evolves a $1.6M_\odot$ star with $Z = 0.02$ from ZAMS to where $0.198M_\odot$ of its core is locally at least 90% helium. Salient non-default parameter values are:

```
mesh_delta_coeff = 0.5
h1_boundary_limit = 0.1
h1_boundary_mass_limit = 0.198
```

The second smoothly removes the outer $1.4M_\odot$, leaving a hydrogen layer with $\sim 1\%$ of the remaining mass. This is achieved with:

```
relax_mass = .true.
new_mass = 0.2
```

The third evolves the resulting $0.2M_\odot$ WD until $T_{\rm eff} = 5{,}000$ K. We invoke MESA's element diffusion routine even where the plasma interaction parameter $\Gamma > 1$. Salient non-default parameter choices are:

```
mesh_delta_coeff = 0.05
which_atm_option = 'simple_photosphere'
surf_bc_offset_factor = 0
do_element_diffusion = .true.
use_Ledoux_criterion = .true.
diffusion_gamma_full_off = 1d10
diffusion_gamma_full_on = 1d10
diffusion_T_full_off = -1
diffusion_T_full_on = -1
diffusion_Y_full_off = -1
diffusion_Y_full_on = -1
```

Our carbon/oxygen WD models (Table 3.1: `CO6` and `CO12`) were produced by solving for hydrostatic equilibrium subject to heat transport by radiative diffusion and electron conduction (Hansen et al. 2004). We use the OPAL EOS and effective opacities (Rogers et al. 1996) in the WD outer layers, and transition to the Potekhin-Chabrier EOS and electron conduction opacities (Potekhin & Chabrier 2010) where the electrons begin to become degenerate. We use a mixture of 25% carbon, 75% oxygen for the inner 98% of the model's mass, then add a helium layer with 1.7% of the mass, and finally a hydrogen layer with the remaining 0.17%. We smooth the composition transition regions over $\sim 0.1H_p$ with a Gaussian profile, where H_p is a pressure scale height. We treat convection with mixing length theory, using $L = H_p$ for the mixing length.

Appendix C

Dynamical resonance locking

C.1 Deriving fixed point stability conditions

Here we will determine the stability region for the resonance locking fixed point described in § 4.5. The characteristic polynomial P in question is given in equation (4.37).

First, $P_1 > 0$ reduces to

$$\delta\omega_{\mathrm{f}} < \frac{(1-r)^2\gamma^2\Gamma_{\mathrm{tide}}}{r\Gamma_{\mathrm{dr}}^2}. \tag{C.1}$$

We immediately see that this is satisfied if $\Gamma_{\mathrm{dr}} < 0$ (assuming $\Gamma_{\mathrm{tide}} > 0$), since by equation (4.39) we then have $\delta\omega_{\mathrm{f}} < 0$. If instead $\delta\omega_{\mathrm{f}} > 0$, then we can take $|\delta\omega_{\mathrm{f}}| \gg \gamma$ to derive

$$\Gamma_{\mathrm{dr}} < \gamma\left(\frac{1-r}{r^{2/3}}\right)\left(\frac{\Gamma_{\mathrm{tide}}}{\omega}\right)^{1/3}. \tag{C.2}$$

Next, the Hurwitz matrix for P is

$$H = \begin{pmatrix} 2\gamma & P_0 & \\ 1 & P_1 & \\ & 2\gamma & P_0 \end{pmatrix}. \tag{C.3}$$

The remaining condition for stability of the fixed point is that the three leading principal minors of H must be positive; this formally yields three additional inequalities. However, one is $\gamma > 0$ which is always satisfied, and the other two are actually identical:

$$2\gamma P_1 > P_0, \tag{C.4}$$

which expands to

$$\gamma^2\Gamma_{\mathrm{tide}}(1-r)^2 > \Gamma_{\mathrm{dr}}^2\delta\omega_{\mathrm{f}}. \tag{C.5}$$

We now see that $\Gamma_{\mathrm{dr}} < 0$ implies asymptotic stability. If $\Gamma_{\mathrm{dr}} > 0$, then the inequality reduces to (again assuming $|\delta\omega_{\rm f}| \gg \gamma$)

$$\Gamma_{\rm dr} < \gamma(1-r)\left(\frac{\Gamma_{\rm tide}}{\omega}\right)^{1/3}. \tag{C.6}$$

Since equation (C.6) is more restrictive than equation (C.2) (since $r < 1$ for $\Gamma_{\rm dr} > 0$; see equation 4.30), equation (C.6) is the condition for asymptotic stability when $\Gamma_{\rm dr} > 0$.

C.2 Hansen coefficient scaling

Here we will determine how the Hansen coefficients X^k_{lm} scale with harmonic index k. These coefficients are defined to satisfy

$$\left(\frac{a}{D(t)}\right)^{l+1} e^{-imf(t)} = \sum_{k=-\infty}^{\infty} X^k_{lm} e^{-ik\Omega_{\rm orb}t}, \tag{C.7}$$

where D is the binary separation and f is the true anomaly. For $|k| \gg |m|\Omega_{\rm peri}/\Omega_{\rm orb}$, where $\Omega_{\rm peri}$ is the effective orbital frequency at periapse, we have that $X^k_{lm} \propto\!\!\!\sim X^k_{00}$. We can express X^k_{lm} in general as an integral over the eccentric anomaly E (Burkart et al. 2012); for $l = m = 0$, this is

$$\begin{aligned} X^k_{00} &= \frac{1}{\pi}\int_0^{\pi} \cos\left[k(E - e\sin E)\right] dE \\ &= J_k(ek) \end{aligned} \tag{C.8}$$

where J is a Bessel function. We can expand $J_k(ek)$ as (Abramowitz & Stegun 1972)

$$J_k(ek) \propto\!\!\!\sim \frac{1}{\sqrt{k}} \exp\left[-kg(e)\right], \tag{C.9}$$

where

$$\begin{aligned} g(e) &= \frac{1}{2}\ln\left(\frac{1+\eta}{1-\eta}\right) - \eta \\ &= \frac{\eta^3}{3} + \frac{\eta^5}{5} + \frac{\eta^7}{7} + \cdots \end{aligned} \tag{C.10}$$

and $\eta = \sqrt{1-e^2}$.

C.3 Canonical angular momentum

Here we will derive the canonical angular momentum associated with a stellar perturbation. The Lagrangian density for a stellar perturbation is (Friedman & Schutz 1978a)

$$\mathcal{L} = \frac{1}{2}\rho\left(|\dot{\boldsymbol{\xi}}|^2 + \dot{\boldsymbol{\xi}}\cdot B\boldsymbol{\xi} - \boldsymbol{\xi}\cdot C\boldsymbol{\xi}\right), \tag{C.11}$$

where $\boldsymbol{\xi}$ is the Lagrangian displacement vector, the Coriolis force operator B was defined in § 4.4.1, and the Hermitian operator C is defined in e.g. Schenk et al. (2002). The z component of the canonical angular momentum is then

$$\begin{aligned} J &= -\left\langle \partial_\phi\boldsymbol{\xi}, \frac{\partial\mathcal{L}}{\partial\dot{\boldsymbol{\xi}}}\right\rangle \\ &= -\left\langle \partial_\phi\boldsymbol{\xi}, \dot{\boldsymbol{\xi}} + B\boldsymbol{\xi}/2\right\rangle. \end{aligned} \tag{C.12}$$

As in § 4.4.1, we perform a phase space expansion of the Lagrangian displacement vector and its time derivative (Schenk et al. 2002), so that

$$\begin{pmatrix}\boldsymbol{\xi}\\ \dot{\boldsymbol{\xi}}\end{pmatrix} = \sum_A q_A \begin{pmatrix}\boldsymbol{\xi}_A\\ -i\omega_A\boldsymbol{\xi}_A\end{pmatrix}, \tag{C.13}$$

where A runs over all rotating-frame stellar eigenmodes and both frequency signs. The canonical angular momentum then becomes

$$J = \frac{1}{2}\sum_{AB} q_A^* q_B m_A \left[2\omega_B\left\langle\boldsymbol{\xi}_A,\boldsymbol{\xi}_B\right\rangle + \left\langle\boldsymbol{\xi}_A, iB\boldsymbol{\xi}_B\right\rangle\right]. \tag{C.14}$$

Since $\left\langle \partial_\phi\boldsymbol{\xi}, \dot{\boldsymbol{\xi}}\right\rangle$ is real valued, we can re-express equation (C.14) as

$$J = \frac{1}{2}\sum_{AB} q_A^* q_B \left[(m_A\omega_B + m_B\omega_A)\left\langle\boldsymbol{\xi}_A,\boldsymbol{\xi}_B\right\rangle + m_A\left\langle\boldsymbol{\xi}_A, iB\boldsymbol{\xi}_B\right\rangle\right]. \tag{C.15}$$

We have that $\left\langle\boldsymbol{\xi}_A,\boldsymbol{\xi}_B\right\rangle \propto \delta_{m_A,m_B}$, so J reduces to

$$J = \frac{1}{2}\sum_A \frac{\varepsilon_A m_A}{\omega_A}|q_A|^2, \tag{C.16}$$

where we have used the orthogonality relation (Friedman & Schutz 1978b)

$$(\omega_A + \omega_B)\left\langle\boldsymbol{\xi}_A,\boldsymbol{\xi}_B\right\rangle + \left\langle\boldsymbol{\xi}_A, iB\boldsymbol{\xi}_B\right\rangle = \delta_{AB}\frac{\varepsilon_A}{\omega_A}. \tag{C.17}$$

Bibliography

Abramowitz, M., & Stegun, I. A. 1972, Handbook of Mathematical Functions (Dover)

Adelman, S. J. 2004, in IAU Symposium, Vol. 224, The A-Star Puzzle, ed. J. Zverko, J. Ziznovsky, S. J. Adelman, & W. W. Weiss, 1

Arras, P., Burkart, J., Quataert, E., & Weinberg, N. N. 2012, MNRAS, 422, 1761

Arras, P., Flanagan, E. E., Morsink, S. M., et al. 2003, ApJ, 591, 1129

Barker, A. J., & Ogilvie, G. I. 2010, MNRAS, 404, 1849

Bildsten, L., Ushomirsky, G., & Cutler, C. 1996, ApJ, 460, 827

Brown, W. R., Kilic, M., Hermes, J. J., et al. 2011, ApJ, 737, L23

Burkart, J., Quataert, E., Arras, P., & Weinberg, N. N. 2012, MNRAS, 421, 983

—. 2013, MNRAS, 433, 332

Campbell, C. G. 1984, MNRAS, 207, 433

Chabanat, E., Bonche, P., Haensel, P., Meyer, J., & Schaeffer, R. 1998, Nuclear Physics A, 635, 231

Chapman, S., & Lindzen, R. S. 1970, Atmospheric Tides (Dordrecht, Netherlands: D. Reidel Press)

Charbonneau, P., & MacGregor, K. B. 1993, ApJ, 417, 762

Christensen-Dalsgaard, J. 2003, Lecture Notes on Stellar Oscillations, 3rd edn. (http://users-phys.au.dk/jcd/oscilnotes/)

—. 2008, Ap&SS, 316, 113

Darwin, G. H. 2010, The Scientific Papers of Sir George Darwin 5 Volume Paperback Set

Dewitt, H., Slattery, W., Baiko, D., & Yakovlev, D. 2001, Contributions to Plasma Physics, 41, 251

Dyson, J., & Schutz, B. F. 1979, Royal Society of London Proceedings Series A, 368, 389

Dziembowski, W. 1977, Acta Astron., 27, 203

Friedman, J. L., & Schutz, B. F. 1978a, ApJ, 221, 937

—. 1978b, ApJ, 222, 281

Fuller, J., & Lai, D. 2011, MNRAS, 412, 1331

—. 2012a, MNRAS, 421, 426

—. 2012b, MNRAS, 420, 3126

Goldreich, P. 1965, MNRAS, 130, 159

Goldreich, P., & Nicholson, P. D. 1989a, ApJ, 342, 1079

—. 1989b, ApJ, 342, 1075

Goldreich, P., & Peale, S. J. 1968, ARA&A, 6, 287
Goldreich, P., & Soter, S. 1966, Icarus, 5, 375
Goodman, J., & Dickson, E. S. 1998, ApJ, 507, 938
Gradshteyn, I. S., & Ryzhik, I. M. 2007, Table of Integrals, Series, and Products, 2nd edn. (Elsevier)
Hansen, C. J., Kawaler, S. D., & Trimble, V. 2004, Stellar Interiors, 2nd edn. (New York: Springer)
Hansen, C. J., & van Horn, H. M. 1979, ApJ, 233, 253
Hermes, J. J., Kilic, M., Brown, W. R., et al. 2012, ApJ, 757, L21
Horowitz, C. J., Berry, D. K., & Brown, E. F. 2007, Phys. Rev. E, 75, 066101
Hut, P. 1981, A&A, 99, 126
Iben, Jr., I., Tutukov, A. V., & Fedorova, A. V. 1998, ApJ, 503, 344
Ipser, J. R., & Lindblom, L. 1990, ApJ, 355, 226
Jackson, J. D. 1999, Classical Electrodynamics, 3rd edn. (Wiley)
Koch, D. G., Borucki, W. J., Basri, G., et al. 2010, ApJ, 713, L79
Kumar, P., Ao, C. O., & Quataert, E. J. 1995, ApJ, 449, 294
Kumar, P., & Quataert, E. J. 1998, ApJ, 493, 412
Lai, D. 1994, MNRAS, 270, 611
—. 2012, MNRAS, 423, 486
Liebert, J., Bergeron, P., & Holberg, J. B. 2003, AJ, 125, 348
Lindzen, R. S. 1966, Monthly Weather Review, 94, 295
—. 1981, J. Geophys. Res., 86, 9707
Longuet-Higgins, M. S. 1968, Royal Society of London Philosophical Transactions Series A, 262, 511
Meibom, S., Mathieu, R. D., & Stassun, K. G. 2006, ApJ, 653, 621
Murray, C. D., & Dermott, S. F. 1999, Solar System Dynamics (UK: Cambridge University Press)
Ogilvie, G. I., & Lin, D. N. C. 2004, ApJ, 610, 477
O'Leary, R. M., & Burkart, J. 2013, ArXiv e-prints, arXiv:1308.0016 [astro-ph.SR]
Orosz, J. A., & Hauschildt, P. H. 2000, A&A, 364, 265
Panei, J. A., Althaus, L. G., Chen, X., & Han, Z. 2007, MNRAS, 382, 779
Paxton, B., Bildsten, L., Dotter, A., et al. 2011, ApJS, 192, 3
Penev, K., Barranco, J., & Sasselov, D. 2009, ApJ, 705, 285
Penev, K., & Sasselov, D. 2011, ApJ, 731, 67
Peters, P. C. 1964, Physical Review, 136, 1224
Pfahl, E., Arras, P., & Paxton, B. 2008, ApJ, 679, 783
Piro, A. L. 2011, ApJ, 740, L53
Potekhin, A. Y., & Chabrier, G. 2010, Contributions to Plasma Physics, 50, 82
Press, W. H., & Teukolsky, S. A. 1977, ApJ, 213, 183
Rathore, Y., Blandford, R. D., & Broderick, A. E. 2005, MNRAS, 357, 834
Reisenegger, A., & Goldreich, P. 1994, ApJ, 426, 688
Robinson, E. L., Kepler, S. O., & Nather, R. E. 1982, ApJ, 259, 219
Rogers, F. J., Swenson, F. J., & Iglesias, C. A. 1996, ApJ, 456, 902
Rössler, O. E. 1976, Physics Letters A, 57, 397

Schenk, A. K., Arras, P., Flanagan, É. É., Teukolsky, S. A., & Wasserman, I. 2002, Phys. Rev. D, 65, 024001

Shiode, J. H., Quataert, E., & Arras, P. 2012, MNRAS, 423, 3397

Spruit, H. C. 1999, A&A, 349, 189

Steiner, A. W., & Watts, A. L. 2009, Physical Review Letters, 103, 181101

Thompson, T. A. 2011, ApJ, 741, 82

Unno, W., Osaki, Y., Ando, H., Saio, H., & Shibahashi, H. 1989, Nonradial Oscillations of Stars (Japan: Tokyo University Press)

von Zeipel, H. 1924, MNRAS, 84, 665

Weinberg, N. N., Arras, P., & Burkart, J. 2013, ApJ, 769, 121

Weinberg, N. N., Arras, P., Quataert, E., & Burkart, J. 2012, ApJ, 751, 136

Weinberg, N. N., & Quataert, E. 2008, MNRAS, 387, L64

Welsh, W. F., Orosz, J. A., Aerts, C., et al. 2011, ApJS, 197, 4

Wiggins, S. 2003, Introduction to Applied Nonlinear Dynamical Systems and Chaos, 2nd edn. (Springer)

Willems, B., Deloye, C. J., & Kalogera, V. 2010, ApJ, 713, 239

Winget, D. E., Kepler, S. O., Campos, F., et al. 2009, ApJ, 693, L6

Witte, M. G., & Savonije, G. J. 1999, A&A, 350, 129

—. 2002, A&A, 386, 222

Zahn, J. P. 1970, A&A, 4, 452

Zahn, J.-P. 1975, A&A, 41, 329

—. 1977, A&A, 57, 383